Creep and fluidity of a granular packing under shear stress

van Bau Nguyen

PUCVL
Pôle Universités
Centre Val de Loire

UNIVERSITÉ D'ORLÉANS

UNIVERSITE D'ORLEANS

ÉCOLE DOCTORALE SCIENCES ET TECHNOLOGIES

Institut des Sciences de la Terre d'Orléans

THÈSE présentée par :

Van Bau NGUYEN

soutenue le : **03 Novembre 2011**

pour obtenir le grade de : **Docteur de l'Université d'Orléans**

Discipline/ Spécialité : **Géosciences**

Fluage et fluidité d'un empilement granulaire sous contrainte

THÈSE dirigée par :

Ary BRUAND	Professeur, Université d'Orléans
Eric CLÉMENT	Professeur, Université Paris VI

RAPPORTEURS :

Farhang RADJAI	Directeur de recherche, CNRS
Yoël FORTERRE	Chargé de recherche, HDR, CNRS

JURY :

M. Jean-Louis ROUET	Université d'Orléans, Examinateur
M. Christian HARTMANN	IRD, Examinateur
M. Farhang RADJAI	CNRS, Rapporteur
M. Yoël FORTERRE	CNRS, Rapporteur
M. Ary BRUAND	Université d'Orléans, Directeur de thèse
M. Eric CLÉMENT	Université Paris VI, Directeur de thèse

REMERCIEMENTS

J'aimerais tout d'abord remercier les membres du jury qui ont accepté d'évaluer mon manuscrit de thèse.

Je remercie particulièrement mes directeurs de thèse, Eric Clément et Ary Bruand, pour avoir orienté la thèse dans le bon sens, mais aussi pour le temps qu'ils m'ont consacré.

Je remercie des collègues dans mon bureau : Olivier Dron, Nicolas Champagne et Romain Mari qui m'ont donné beaucoup des conseil utiles pendant ma thèse.

Je remercie à toute ma famille : Lan Phuong Bui, Minh Khoi Nguyen.... qui m'ont constamment soutenu pendant mes études.

RÉSUMÉ

L'objectif principal de la thèse a été d'identifier expérimentalement les comportements mécaniques et rhéologiques de milieux granulaires dans un environnement de complexité croissante. En particulier, je me suis intéressé aux phénomènes de fluage sous contrainte en essayant de mieux comprendre l'impact des vibrations et la présence d'une faible quantité d'eau piégée entre les grains.

Au début de ma thèse, j'ai monté un système cissométrique permettant de réaliser des tests mécaniques de fluage. Ce dispositif a spécialement été conçu pour accéder aux domaines de très faibles contraintes cisaillements et de déformations. En outre, c'est un système de mesure relativement simple qui peut être adapté facilement aux problèmes de terrain et ainsi, à terme, permettre d'évaluer les caractéristiques mécaniques d'un sol " réel ". Au laboratoire, j'ai étudié les propriétés fondamentales de fluage sous contrainte d'un empilement granulaire de billes de verre de taille $d = 200\mu m$ sous le seuil de Coulomb. Une originalité de mon montage a été de mettre au point un système de lit fluidisé qui, en alliant flux d'air et vibration, m'a permis de fabriquer des empilements de compacité initiale contrôlée. En partant d'une situation très décompactée, par impacts successifs, on peut obtenir des compacités plus importantes. Grâce à des mesures de perte de charge, on accède à la perméabilité moyenne de la structure granulaire, j'ai établi une relation d'étalonnage entre perméabilité et compacité ; cela permet de remonter précisément à la compacité. Ce montage permet en outre, par injection dans le granulaire d'un gaz saturé en vapeur d'eau, d'imposer sous un faible gradient thermique une condensation et d'obtenir une quantité contrôlée d'eau piégée dans l'empilement. Cette méthode permettra par la suite d'aborder le cas de granulaires cohésifs.

Cette étude a mis en évidence que les seuils de Coulomb varient fortement avec la compacité, mais en plus , on a mis en évidence une contrainte σ_r appelée " contrainte de première rupture " qui traduit des réorganisation internes dans l'empilements et qui est d'environ 1/3 de la contrainte seuil maximale. En outre, grâce à la précision de la mesure de déformation, on a obtenu les réponses élastiques à de petits cycles en contrainte et on a établi que le module cisaillement élastique G augmente linéairement en fonction de la compacité, en accord avec le modèle d'élasticité non-linéaire de Hertz (modèle de champ moyen). En absence de vibration, nous avons réalisé une étude paramétrique complète du fluage en variant systématiquement la compacité et la contrainte de cisaillement. Dans tous les cas nous avons mise en évidence une dynamique de déformation logarithmique pour temps longs.

Il a été montré qu'une dynamique de déformation logarithmique peut-être observée même sous de faibles niveaux de contrainte. Elle peut être caractérisée empiriquement par un modèle de rhéologie initialement introduit par Derec et al.[13] mettant en jeu une variable dynamique interne appelé "fluidité". Les deux paramètres du modèle (fluidité initiale et coefficients de vieillissement) sont mesurés en fonction de la compacité et du niveau de contrainte. De plus, bien avant le seuil de Coulomb, un seuil dit de "micro-rupture" est observé, correspondant à des réarrangements

granulaires qui ont pour effet d'augmenter le coefficient de vieillissement, c'est à dire de ralentir la dynamique de fluage avant la rupture finale correspondant au seuil de Coulomb. Cette étude a été prolongée pour des empilements sous vibration et en présence d'une quantité d'eau ajoutée.

Notre étude sur les seuils de contrainte, l'élasticité effective et la dynamique de fluage, a été prolongée pour des empilements sous vibration générés par des transducteurs piézo-électriques enfouis sous la surface. On a trouvé aussi que les seuils de Coulomb à différentes compacités, pouvaient être notablement diminués en fonction du niveau de vibration même pour de faibles accélérations moyennes. On constate que le module élastique est lui aussi diminué par la vibration et que sa valeur est quasiment réversible pour des temps faibles d'application de la vibration. On a étudié aussi l'influence des formes spectrales des vibrations sur la dynamique de fluage. Pour une même fréquence d'excitation et un même niveau d'énergie élastique dans le granulaire, deux types de sources ont été étudiés : une vibration sinusoïdale produisant une réponse très harmonique et des créneaux produisant un spectre beaucoup plus large.

Une faible quantité d'eau peut aussi être ajoutée et ainsi modifier les propriétés mécaniques par la présence de ponts capillaires. Nous avons mis au point et étalonné une méthode d'injection d'un air humidifié à une température légèrement supérieure à la température ambiante. On a vérifié (par pesée avec une micro balance) que la condensation dans le granulaire augmentait avec ce temps d'injection et que la quantité d'eau condensée dépendait faiblement de la hauteur. C'est donc une méthode intéressante pour étudier les granulaires faiblement humides. Des expériences préliminaires montrent la dépendance des seuils de Coulomb de la réponse élastique et de la dynamique de fluage avec la quantité d'eau piégée.

ABSTRACT

The main objective of the thesis was to identify experimentally the mechanical and rheological behavior of granular medium in an environment varying in complexity. In particular, I was interested to creep phenomenon under stress in trying to understand better the impact of vibration and the presence of a small amount of water trapped between the grains.

At the beginning of my thesis, I set-up a system to perform mechanical creep tests. This device has been specially designed to access to areas of very low shear stresses and deformations. In addition, it is a device that can be easily adapted to field environment, and this to assess the mechanical properties of 'real' soils. In the laboratory, I studied the basic properties of creep strain of a granular resulting from the packing of glass beads with means diameter $d = 200\mu m$ under the Coulomb threshold. An originality of my set-up was the fluidized bed, which uses air flow and vibration, and this allows the control of the initial packing fraction. Starting from a very loose packing, and using successive mechanical, a higher compacity can be reached. Through pressure difference measurement, we determine the average permeability of the granular medium. Then, I established a calibration relationship between the permeability and the packing fraction, which can be used to go back precisely to the packing fraction. This setup also allows us to inject in a granular medium air saturated with water vapor, imposed under low thermal gradient and condensation to obtain a controlled amount of water content. It will be possible to apply this method to the case of cohesive granular medium.

This study showed that the Coulomb thresholds varies strongly with the packing fraction. In addition, it showed a stress σ_r called "the first rupture", that results from internal reorganizations in the granular medium and which is approximated 1/3 of the maximum stress threshold. Moreover, thanks to the precision of measuring deformation, we obtained the elastic response with small stress cycles, and we found that the shear elastic modulus G increases linearly with the packing fraction, in agreement with the model of nonlinear elasticity of Hertz (mean field). In the absence of vibration, we performed a parametric study of creep in varying the packing fraction and shear stress. In all cases, we found the dynamics of logarithmic creep for long times.

The logarithmic creep can be observed even under low stress levels. It can be empirically characterized by a rheological model introduced by Derec et al.[13], involving an internal dynamic variable called "fluidity". The two model parameters (initial fluidity and coefficient of aging) are measured in terms of packing fraction and the stress level. Before the Coulomb threshold, the "first-rupture" is observed, that have the effect of increasing the aging coefficient. It slows creep dynamics before the final threshold corresponding to the Coulomb threshold. This study was extended to granular medium under vibration and in the presence of water added.

Our study on stress threshold, the elastic modulus and dynamics of creep, has been extended to granular medium under vibration generated by piezoelectric transducers buried under the surface. We also found that the Coulomb thresholds at different packing fractions, could be significantly reduced depending on the level of vibration even at low accelerations averages. It is found

that the elastic modulus is also reduced by the vibration and its value is almost reversible for low-time application of vibration. We also studied the influence of the spectral shapes of vibration. For the same excitation frequency and the same level of elastic energy in the granular, two types of vibration were studied : a sinusoidal vibration producing a very harmonic response and a square vibration producing a much wider spectrum.

A small amount of water can be added and thus modifies the mechanical properties by the presence of capillary bridges. We developed and calibrated a method for injecting a humidified air at a temperature slightly above room temperature. We checked (by weighing with a micro scale) that in the granular medium the condensation increased with the injection time and that the amount of water depended weakly on the height. This is an interesting method to study a wet granular. Preliminary experiments show the dependence of the Coulomb threshold of the elastic response and dynamic creep with the amount of water content.

TABLE DES MATIÈRES

CHAPITRE 1

INTRODUCTION GÉNÉRALE

Contents

1.1 Introduction

This work has originated from a collaboration between the *Laboratoire de Physique et Mécanique des Milieux Hétérogènes (PMMH)* in *Pierre and Marie Curie University*, a physics laboratory and the *Institut des Sciences de la Terre d'Orléans (ISTO)* in *University of Orléans* specialized in soil-science. The objective of the current collaboration is to provide a better understanding to a class a granular systems called "*sandy soils*". This type of soil is composed of a granular matrix made of sandy grains of size reaching fractions of a millimeter. A second granular scale is mixed to the first one and consists of fine micro particles, essentially made of clay. The fraction of clay is very small and provides marginal cohesion to the packing. This last system is known in the soil-science community for its inherent structural instability and all the problem it poses in the context of agriculture and food production in deserted areas of the planet.

The results of my thesis is not directly applied to sandy-soils, however it may hopefully establish an original conceptual direction towards a better understanding of restructuration process due to mechanical constraints in loosely cohesive granular materials.
More generally, granular materials may come in a very large variety of shapes, sizes and inter-granular interactions. Usually, the expression "granular material" is restricted to assemblies of macroscopic particles such that thermal processes are quite irrelevant to describe the macroscopic physics and the mechanical properties. In the last decades, an intense scientific activity has been devoted to the understanding their constitutive relations. In the physics community the effort was principally focused on the fundamental understanding of simplified granular models such as idealized packing of spheres. In spite its relative simplicity, it was proven to be a very successful approach to identify generic behavior and clarify fundamental mechanisms at work for example in the rheology of an assembly of grains interacting microscopically through solid contacts. It has helped to shed new light on much more complex systems involving non only granular materials but also belonging to the class of complex fluids. This reductionist vision is currently evolving by the addition of elements of increasing complexity. My thesis follows this line of thought. First, I will consider the mechanical response of packing of dry glass beads. Then, I will study the changes in behavior due to the addition of weak vibrations. Finally, I will consider the case where a small amount of water is added to the packing.

The purpose of this first chapter is to present the concepts I will use in the framework of my thesis. First, I will present the basics for the "jamming transition" of a packing of grains and its relation to other complex fluids and glassy systems. Then, I will discuss the notion of elastic response of a granular packing. To this purpose, I will present the standart Hertz model for granular contacts rigity and its consequence on the relationship between the shear elastic modulus and the packing fraction.
Then, I will describe the generic response of a granular material to shear and introduce the Mohr-Coulomb theory which is currently used to characterize the shear strength of a granular medium. Thereafter, I will discuss the creep phenomenonology and empirical models used to describing long time deformation in soils. To complement the description of lond time relaxation, I will present also some notions of the recent descrition of complex fluid rheology involving internal complex relaxation mechanisms. I will then introduce the notion of material '*fluidity*' which is a base of analysis of my experimental results.
After that, I will review some elements describing the influence of vibration on the mechanical responses and flow properties of a granular medium. Finally, I will present a brief summary of the

works that have been devoted to the role of water content in a granular packing. In particular, I will discuss how the cohesion of wet granular matter may change with an amount of water added.

1.2 Jamming et RCP d'un milieu granulaire

For a granular assembly at low packing fraction ϕ, the spatial distribution of grains can be such that at zero agitation, particles do not touch each other and thus, the granular pressure is $p = 0$. If energy is transfered to the system via some external driving, the particles will collide as in a gas or in a liquid. In this last case, the square of velocity fluctuations is a good macroscopic variable decribing the transfer of momentum and energy. This is the so-called granular gas state. An equation of state linking the pressure to granular temperature can then be established. In the limit of zero confining pressure and zero temperature, as ϕ is increased, the granular system will reach a value ϕ_j, at which the particles just touch and lock into a rigid but disordered structure. To increase ϕ further one has to exert an external confining pressure $p > 0$ and compress elastically the grains. This is the 'jamming transition' : a transition from a liquid-like state to a rigid solid-like state charaterize by a positive macroscopic elastic shear modulus. The critical nature of the jammed state and the values of ϕ_j at the jamming transition depend on the dimensionality D of the system as well as some microscopic properties of the individual particles.

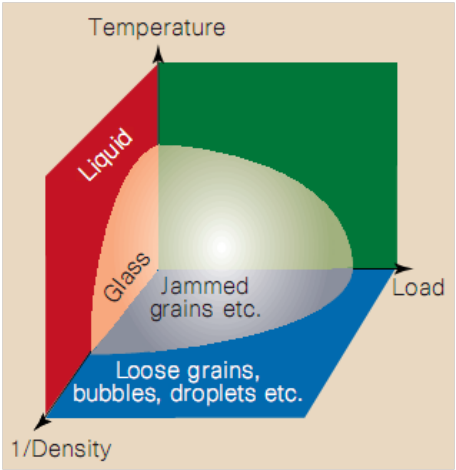

FIGURE 1.1: Jamming phase diagram proposed by Liu and Nagel [53]

In the absence of inter-granular friction ($\mu = 0$), the jamming point will correspond to a critical number of contact : $z_c = 2D$. For $\mu \neq 0$, the addition of rotational degrees of freedom lead to a drastic change in the value of the critical number of contacts : $Z_c = D+1$. As a consequence, grains with friction can undergo a jamming processes at much lower packing fraction [26] than frictionless particles. For spherical, frictionless and rigid particles, the density at which a packing is jammed is often called the 'random close packing' (RCP) density ϕ_{rcp}. From numerous experiments and numerical simulations, one finds that for large number of particles, the random close packing densities are [43, 82] : in 2D $\phi_{rcp} \approx 0.84$ and in 3D $\phi_{rcp} \approx 0.64$. In spite of the many consistent experimental and numerical determinations of the ϕ_{rcp} values, a clear mathematical definition of what RCP means and a precise analytical calculation of it, remain elusive. In practice, a rigid assembles of frictional spheres can experience a jammed state for a packing fraction range : $0.55 \leq \phi \leq 0.635$.

In 1998, Liu and Nagel [53] sketched a speculative phase diagram suited to unify the description of many different materials such as granular materials, pastes, dense suspensions, foams, glasses etc... (see fig.1.1). All these systems display a severe slowing down of their dynamics leading to quasi blockade of the flow which is usually called "jamming". These authors suggested that temperature, packing fraction and stress can play a similar role as jamming would occur at low temperature, low applied stress and low volume per grain. For a granular medium, as we noted, the thermodynamic temperature plays a priori no role. However, a timely question is to understand to which extend external mechanical vibration could play a role similar to the thermodynamic temperature for glassy thermal systems.

1.3 Propriétés mécaniques et déformation par fluage d'un milieu granulaire

1.3.1 Relation entre contrainte et déformation

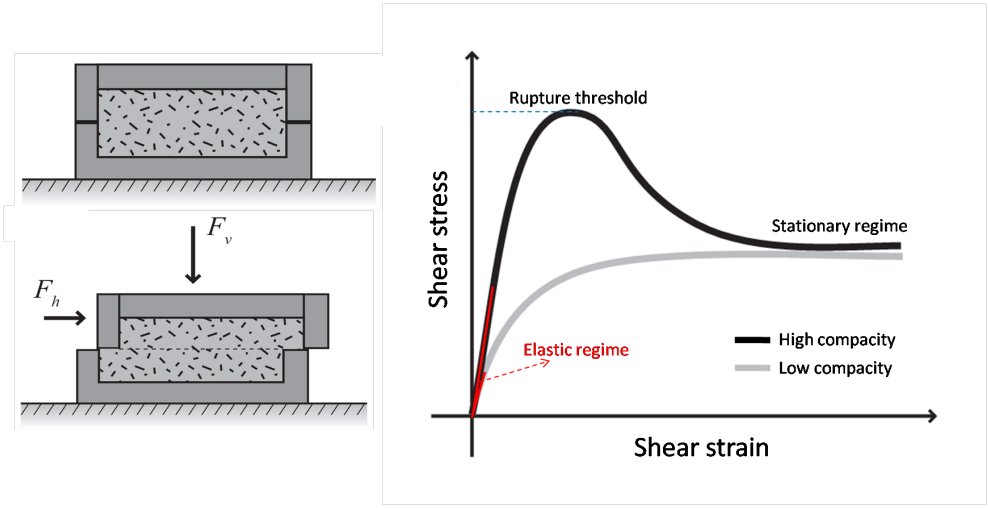

FIGURE 1.2: Schematic representation of a direct shear test (left) and variation of the shear stress as a function of shear strain as a function of the granular medium compacity (right).

A well known method for characterizing the shear-strain relation for a granular medium is for example, the direct shear test (sketch on fig.1.2 left). In this test, the shear stress is simply calculated by the relation :

$$\sigma = F_h / S \tag{1.1}$$

where S is the contact surface area, F_h is the shear force for a confining pressure $P = F_v / S$. During deformation, dense samples tend to dilate, and loose ones to contract. This is the "dilatancy effect" first noted and qualitatively explained by O.Reynolds in the XIX^{th} century. At high packing fractions, the shear-strain curve presents a peak of shear stress called the maximum shear stress. If one continues to shear, the resistance of the material decreases toward a constant value called the residual resistance of the material. On the other hand , if the packing fraction is low, one does not observe a peak of resistance, but only the residual resistance at large deformation. These results are very generic and were found in other shear tests like : the annular shear or the triaxial test.

Note that for all experimental tests, one observes in practice a strong localization of the deformation field called a "shear band". Typically shear bands occurs at the stresses around the peak value for dense packing and when the stress-strain curve saturates for loose packing. In dry granular packing, the shear-band lateral extension is of a few grain size. At low deformation, one observes an elastic regime (fig.1.2 left). In this regime, the relations between the shear stress and the shear strain are linear and reversible. For an ideal shear test, the slope would correspond to the shear elastic modulus G at a given confining pressure P.

1.3.2 Réponse élastique d'un milieu granulaire

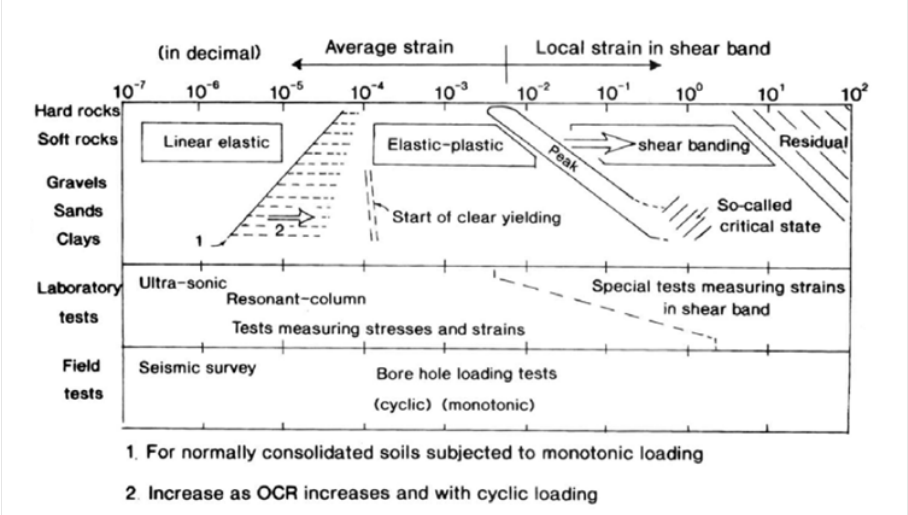

FIGURE 1.3: Empirical behavior of a large class of granular materials based on the response to shear deformation [33]

.

In practice, the elastic domain has been tested by different experimental methods (static or dynamic). Static experiment were performed by very small charge-discharge cycles of shear stress or shear strain, at a low frequency, in order to determine the shear modulus G. On the other hand, dynamic experiments, mostly using the sound wave propagation at a high frequencies (some kHz) were performed. An elastic behavior is actually identified under very small deformations (fig.1.3). The deformation level corresponding to the transition between the elastic and plastic behavior can vary by one to two orders of magnitude [33] according to the material and the nature of granular interactions. Fig.1.3 shows that, for material such as sand or clay. Measurements were performed at very low deformation level to identify the elastic domain (below $10^{-4}(m/m)$). In this thesis, we developed an experimental set-up suited to monitor deformations in this range (Chapter3).

1.3.3 Modèle de Hertz

First, we present the classical theory of inter-particular forces between two spheres for a linear material elasticity. When two spheres of radius R are compressed against each other by a force F, they are flattened in the vicinity of the contact zone in the form of a disk of radius a as the distance between their centers decreases of value δ. The deformation is the displacement relative to the size

characteristic of the deformed area δ/a. From Hooke's law, the relationship between the average stress σ and the deformation yields :

$$\sigma = \frac{F_N}{a^2} \propto E_g \frac{\delta}{a} \tag{1.2}$$

where E_g the grain Young's modulus, and the relationship between the radius of the contact area and the displacement is : $a^2 \approx R\delta$. Then, the contact force scales in a non-linear way with δ as :

$$F_N \propto R^2 E_g (\frac{\delta}{R})^{3/2} \tag{1.3}$$

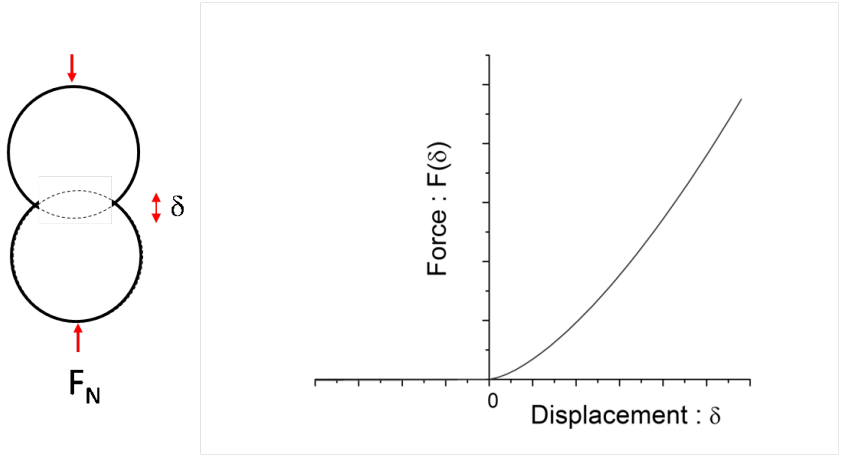

FIGURE 1.4: Schematic representation of the contact between two spheres with a displacement δ (left) and relation between the force and the displacement (right).

The full mechanical calculation was first carried by Hertz [45] and he found that the normal force between two spheres of identical radii is :

$$F_N = \frac{8_g}{3(1-\nu_g)} R^2 (\frac{\delta}{R})^{3/2} \tag{1.4}$$

where G_g is the shear modulus of the material and ν_g the Poisson ratio. If the spheres have different radii of curvature, it can be shown that : $R = \frac{2R_1R_2}{R_1+R2}$.
The previous qualitative argument can be extended to the shear stiffness calculation. If one calls F_T, the tangential force component between two spheres, with $F_T < \mu_s F_N$ as a condition for no slip, where μ_s is the coefficient of static friction, the two grains undergo a small relative tangential displacement Δs, the transverse deformation scale is $\Delta s/a$. The relationship between the mean stress and the shear deformation can be expressed as :

$$\frac{F_T}{a^2} \propto \mu_g (\frac{\Delta s}{a}) \tag{1.5}$$

where μ_g is the shear modulus of the grains, the tangential force is then :

$$F_T = \frac{8\mu_g}{2-\nu_g} R (\frac{\delta}{R})^{1/2} \Delta s \tag{1.6}$$

when the Coulomb limit is reached, the frictional force is $F_T = \mu_s F_N$. Many numerical model are based on such a representation of granular interaction to account for normal and tangential contact forces. This the so-called Hertz-Midlin model. However, as Mindlin himself noticed, there is a mechanical issue associated with the tangential stress at contact. Shear stress can be shown to diverge near the contact edge as in a mode II fracture [45]. This creates a plastic zone at the outer rim of the contact surface. This is an inherent source of dissipation which is rarely taken into account. Another limitation of this description is the presence of plastic deformations at contact, even at moderate external confining stress. These irreversible processes can be due (i) to the stress amplificaction at contact such that the material hardness limit is reached and (ii) microscopic asperities that can be also be plastified (this is the origin of solid friction). So, even though the Herz-Mindlin model provides a firm base for macroscopic calculation of elastic properties, one has to bear in mind that for all "real" granular packing, due to the physics at nanoscopic if not microscopic scales, irreversible plastic processes do indeed take place.
In the framework of the Hertz-Mindlin model, several authors have obtained expressions for the macroscopic bulk and shear elastic modulii (see a review of models and references in [20]). For example a derivation of the macroscopic shear modulus yields the expression :

$$G = \left(\frac{1}{1-\upsilon_g} + \epsilon\frac{3}{2-\upsilon_g}\right)\frac{\mu_g}{5\pi}(\phi z)^{2/3}\left(\frac{3\pi(1-\upsilon_g)}{2\upsilon_g}P\right)^{1/3} \tag{1.7}$$

This equation expresses two limits : no sliding friction between the grains ($\epsilon = 0$) or infinite friction between the grains ($\epsilon = 1$). Note also that in this expression, a continuous variation of $0 \leq \epsilon \leq 1$ would correspond to the "*tangential coupling model*" studied numerically by Makse et al. [20]. Note importantly that this result is a Mean-Field approximation introducing a crucial assumption in the derivation, i.e. a direct relation between the macroscopic and microscopic strains. This has been shown to be a poor approximation to the microscopic granular displacement and leads to quantitative failure of the theory. This failure is especially important for the shear modulus [20]. Experimentally, the relationship between the elastic modulus and the confining pressure has also been studied by acoustic methods [22, 21, 94]. In practice, the scaling law $G \propto P^{1/3}$ is not fully recovered and many open questions remains such as to understand the relation between the packing fraction and the mean number of contacts per grain Z. Numerical simulations have explored this relation for packing of frictionless spheres, near the jamming threshold. The mean number of contacts per grain is a function of the volume fraction [25] and the relation is for $\phi > \phi_c$:

$$Z - Z_c \approx (\phi - \phi_c)^{1/2} \tag{1.8}$$

where in $3D$ the critical contact number is $Z_c = 6$ [25] and $\phi_c \approx 0.639$. For packing with friction, a critical like behavior can be recovered near jamming with a friction dependent value for the critical number of contacts $Z_c(\mu)$ [88]. Far from the jamming "critical" region, the situation is much less clear as in general, there is no one-to-one relation between Z and ϕ [2] and the macroscopic mechanical properties can be strongly preparation dependent [89].

1.3.4 Seuil de rupture, écoulement du milieu granulaire

In soil mechanics, granular material studies are motivated by the desire to understand the failure of foundations, slopes, and soils. The basic model which account for the rupture threshold is the Mohr-Coulomb model [16]. Its phenomenlogy follows the laws of solid on solid Coulomb friction but is adapted to the fact that the rupture problem in granular matter is essentially a tensorial

issue. This model is described by the stability condition :

$$\sigma \leq \sigma_n . tan\varphi \tag{1.9}$$

Where σ is the shear stresses, σ_n the normal stress and the angle φ is called the internal friction angle of the material. These stress components are taken in the reference frame corresponding to the eigen-directions of the stress tensor. With a cohesive granular medium, one must add a cohesion term c and the stability condition becomes :

$$\sigma \leq \sigma_n . tan\varphi + c \tag{1.10}$$

This law expresses that the material maintains its structure as long as the inequality is satisfied and yield occurs when the equality is reached. The angle of internal friction depends on the packing fraction (or the void ratio for soil-mechanicists). Many empirical models exist to account for this dependence. A celebrated one is the study of Caquot et Kérisel [11] who proposed the following relation to relate internal angle and compacity :

$$e.tan\varphi = K \tag{1.11}$$

where K is a constant which depends only on the nature of the material and e is the void ratio calculated by the relation : $e = (1-\phi)/\phi$. Actually, there is no authoritative relation but the increase of φ with ϕ is in practice a well establihed result.
The angle of internal friction depends also on the shape and the surface properties of the grains. An interesting heuristic model is the Rowe model [67] which considers a simple piling made of a bead A put on two beads B and C (see fig.1.5). The bead A sustain a normal force N and a tangential force T. The rupture limit corresponds to the force T just sufficient to move the bead A under the constant force N. Considering that the bead friction coefficient is $\mu_s = tan(\varphi_s)$ and β is the angle between the tangential contact plane and the horizontal direction (see see fig.1.5), a simple calculation of the mechanical conditions of rupture yields a value for the ratio of the tangential force to the normal force :

$$\frac{T}{N} = \tan\varphi = \tan(\beta + \varphi_s) \tag{1.12}$$

where φ represents the angle of internal friction. This model is certainly naive but it shows in a simple way the combined influence on φ of the packing geometry and compacity (through β) and of the granular friction (through ϕ_s).

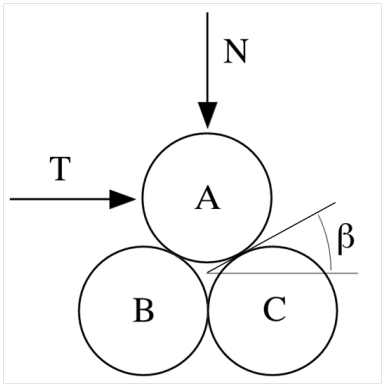

FIGURE 1.5: Rowe model [67] for the internal friction of a packing.

Note that the Mohr-Coulomb theory can be extented to account for the large plastic deformation of granular materials. The qualitative phenomenology described in 1.3 can be reproduced by sophisticated incremental plasticity model [65] which are based on many experimental tests to get empirical constitutive parameters. However, in this type of approach, which is the base for soil mechanics calculations, no real time dependence is contained. From the Rowe formulation (see equ.1.12), one can simply see that as long as compacity (encripted in β) and intergranular friction do not change with time, the Coulomb limit bears no dependence with time either. However, many tribology studies show that solid on solid friction coefficients generically display a slow ageing dependence due to nanoscopic plastic processes. Immediatly one can see that at long time scale, this could influence on the constitutive properties of granular matter [38] and also eventually change on the long time, the structual properties of the packing.

1.3.5 Fluage

As seen previously, mechanical properties of granular packing are usually described phenomenologically by rate independent constitutive relations [8]. However, there are also compelling experimental evidences that for granular assemblies in "real" environment (i.e. finite temperature, temperature variations or background noise), this limit is just a short-time approximation and that time dependent processes are significant on the long run. In soil mechanics and engineering, where the issue of long time resistance to stress is of practical importance, standard tests do actually reveal aging properties for a large class of granular materials [77].

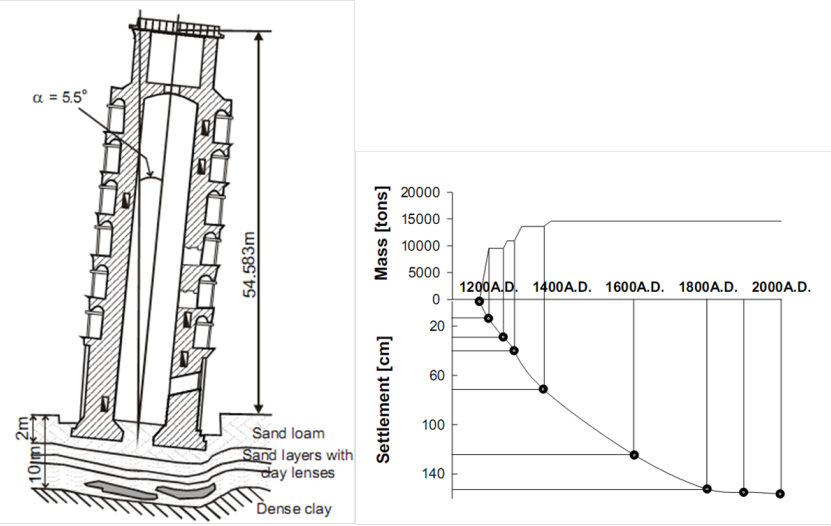

FIGURE 1.6: *Example of the in-situ creep deformation-Tower of Pisa, Italy*. Section of the Tower of Pisa together with the geological context below the structure (left), illustration of the tower's mean settlement and mass of the structure according to the time (right).

A famous example of creep is the uneven settlement of the Tower of Pisa in Italy. The construction of the tower started in 1173 and was completed in 1360. Due to creep deformation of soils in the form of lenses in the sandy base, the tower settled and tilted on one side. The mean settlement of the structure is a $1.5m$. An illustration of the tower's section and the mean settlement with mass of structure can be found in fig.1.6. There are a lot of other documented examples of in-situ creep

behavior, some of them ending with the total failure on the construction. One of the biggest disaster recorded in soil science was the catastrophy of the Vayont reservoir in Italy [3] where a dam broke as a direct consequence of soil creep.

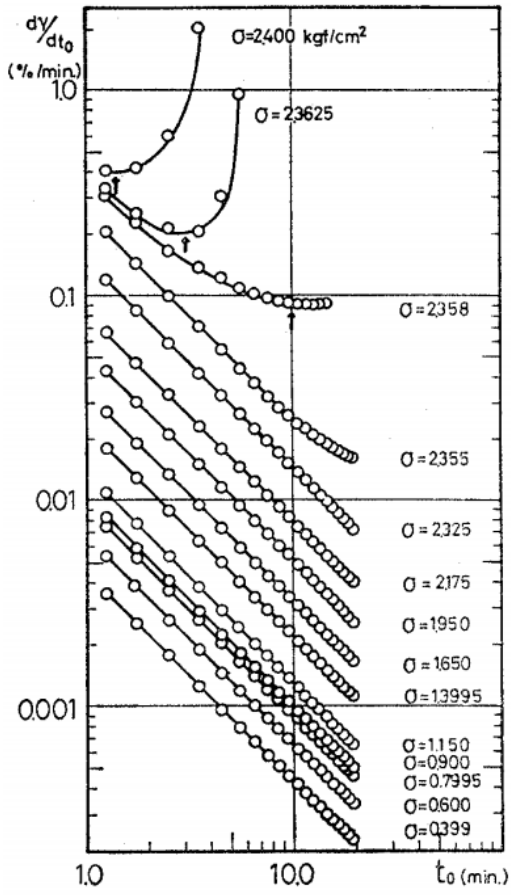

FIGURE 1.7: Strain rate as a function of time for the triaxial creep test, taken from [74].

In soil mechanics, the studies of material creep are usually done via triaxial compression tests [31, 39, 74] where a confining pressure and a deviatoric stress can be applied independently. For example, Murayama et al.[74] have studied the creep characteristics of sands under constant principal stress differences at various stress levels. The variation of the creep strain rate $d\gamma/dt_0$ with time are shown in fig.1.7. On may notice at low deviatoric stresses, the relation $log(d\gamma/dt_0) - log(t_0) \approx t^{-1}$. The relationships at high deviatoric stresses are expressed by a curve of concave-downwards shape probing an acceleration of the dynamics towards the material rupture. Several experiments in the physics community, pointed out towards the central importance of nanometric scales where humidity and/or contact plasticity [29, 38] do impact significantly the macroscopic behavior. Recently, it has been shown how temperature variations may also drive important packing reorganizations [28, 85]. Slow granular reorganization as the result of thermal cycling can be seen in the work of Divoux et al. [85]. The authors monitor the height of a granular column as a function of the number of thermal cycles. They observed the thermal-induced creep phenomenon : after 7 days, the decrease in height was about 1% of the initial height.

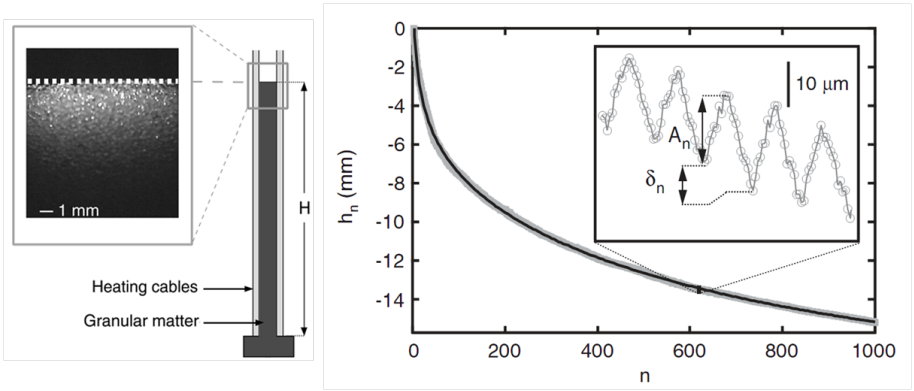

FIGURE 1.8: Height variation h_n as a function of number of thermal cycles n, a logarithmic creep at long time, the black curve corresponds to the a logarithmic law. Inset : Oscillations of the column height associated with the temperature cycles (A_n and δ_n), defined to be the amplitude of the increase and the drift of h_n at the cycles n. The amplitude of the cycles $\Delta T = 10.8°C$ and the frequency $600s$ [85].

Rheological models In classical rheology, the consitutive properties of materials is often seen a complex association of microscopic elements which express simple constitutive relations [4]. One of these "elementary brick" can be a linear Hooke's law (fig.1.9(a)) relating stress and strain. The second important elementary element represents viscous dissipation (fig.1.9(b)) and relates in a linear way, stress and strain rate. Macroscopically, the combination of such elements (provided that the underlying topology is euclidean) yields a visco-elastic behavior which can be represented in a simple scalar form by a relation of the type :

$$\dot{\sigma} = -\frac{\sigma}{\tau} + G\dot{\gamma} \tag{1.13}$$

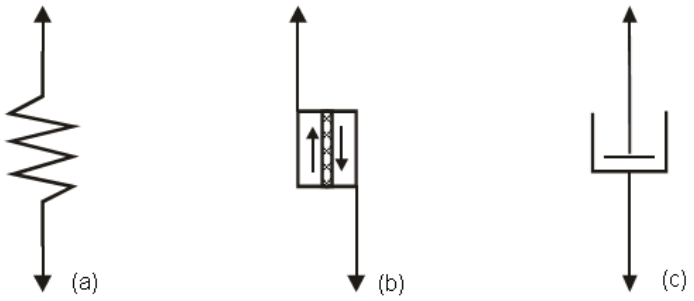

FIGURE 1.9: Basic elements used in rheological models, Hook's elastic element (a), , Newton's viscous element (b), Saint Venant plastic element (c).

Where σ is stress , γ deformation, G an elastic modulus and τ a characteristic time of stress relaxation. Importantly, note that in general a more complex tensorial relation holds, but each normal mode will have essentially a viscoelastic response akin to equ. 1.13. Viscoelastic rheological behavior is shared by many complex fluids such as polymeric fluids. However this approach

misses a large class of systems which display a threshold in stress and a plastic behavior such a granular materials. A solution is to include at the microscopic level other types of idealized elements that display "perfect plasticity" like Saint Venant's plastic elements (fig.1.9(c)) which above a given stress, flow at constant stress. This, of course, allows the emergence of a macrocopic threshold and may render a more rich elasto-visco-plastic phenomenology. However, it does not solve the fundamental problem of the microscopic origin for the plastic yields and fails to provide an account for complex relaxation processes, memory effects, shear-band localization, generally observed in many complex fluids or soft-glassy materials under shear.

Soft Glassy rheology and fluidity models .

Soft glassy materials is a generic term representing microscopically disordered systems where "slow" relaxation and complex dynamical processes take place under shear[6]. This notion encompasses a large class of materials, essentially disordered microscopically but widely differing from their microscopic physical chemistry and from the values assumed by their constitutive parameters. Note that the difference between "soft" glassy systems and "hard" glassy systems as amorphous solids or window glass, is not really conceptual difference but essentially is a question of stress scale at which flow can be triggered. A remarkable fact is that beyond the elastic domain, the response to shear displays in all these systems a very similar phenomenology. These observations have led to the proposition that only a limited number of "universal" scenario may describe plasticity and the consequent rupture modes. Thermal properties and in particular the vicinity of the glass-temperature transition, has of course a tremendous influence on the dynamics of the yield process. However, recent numerical and theoretical efforts have focused on the zero temperature mechanical behavior of sheared disordered solids like Lennard-Jones glasses [84, 62], with the aim to identify *localized deformation zone* that could be seen at the "building bricks" of a subsequent rupture process. Recently, it has been shown that due to the intrinsically disordered structure of the elastic energy landscape, the primary yield modes were elastic instabilities inducing localized irreversible deformations of few "molecular sizes" [84, 62, 30]. On Fig.1.10, I display the results of a numerical simulation of a shearing cell by Lemaitre et al.[30] that illustrates this point. On this figure appear highly localized regions of enhanced mobility, with a quadripolar symmetry.

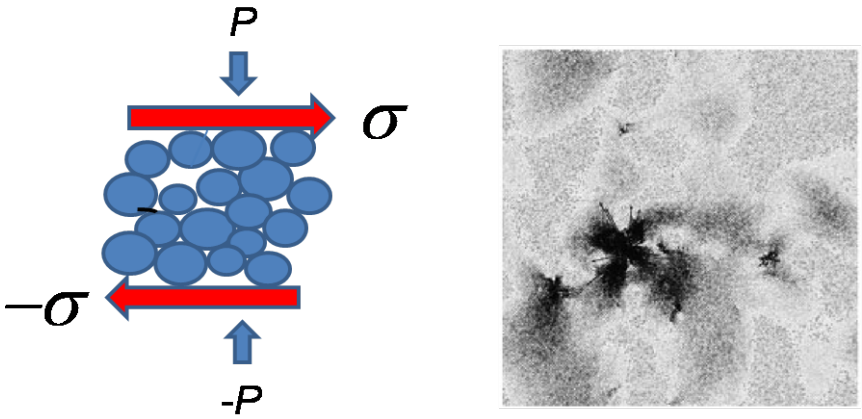

FIGURE 1.10: Schematics of a numerical simulation of soft-spheres under shear (left). Non-afine granular displacements exhibiting a localized zone of quadrupolar yield (from [30]). Arrows represent granular displacement (amplified for visulaization).

These irreversible reorganizations due to elastic instabilities were found to trigger at long range, other localized plastic processes[30]. Scaling behavior describing the spatio-temporal complexity of such an avalanching processes were identified either in direct molecular dynamic simulations or in mesoscopic models using these local features as elementary relaxation mechanisms [30, 19, 83]. Numerical simulations show that the spatial clustering of these zones can be the actual precursors of shear bands [19, 83].
Coming from a different background, the theoretical description of the complex rheology of yield-stress fluids, the "soft glassy rheology" [79, 80] and further developments, is based on ideas of a similar flavor. This approach introduces a statistical picture for the energy relaxation process and its spatio-temporal coupling. The simplest of these models is probably the one introduced by Hebraud and Lequeux[41]. In this model, one deals with an ensemble of sites, each of them can sustain a stress σ_c before yield and reorganization. The central quantity is the probability distribution function $P(\sigma, t$ of the local stresses, which is assumed to evolve according to the equation :

$$\frac{\partial}{\partial t}P(\sigma,t) = -G_0\dot{\gamma}\frac{\partial}{\partial\sigma}P(\sigma,t) - \frac{H(|\sigma|-\sigma_c)}{\tau}P(\sigma,t) + \frac{1}{\tau}\int_{|\sigma'|>\sigma_c} P(\sigma',t)d\sigma'\delta(\sigma) + D\frac{\partial^2}{\partial\sigma^2}P(\sigma,t) \quad (1.14)$$

Eq.1.14 is a simple evolution equation for the probability distribution function. The first term describes the elastic deformation of a block under application of a macroscopic deformation γ, with G_0 a constant elastic modulus. The second and third terms reflect the fact that if the stress of a block exceeds the critical value σ_c, then, a rearrangement occurs with a rate characteristic τ. Finally, the fourth term is a diffusive term which reflects the fact that the rearrangement of a block has an effect on the stress field of its neighbor. The 'stress diffusion constant' D is given by :

$$D = \alpha\frac{1}{\tau}\int_{|\sigma'|>\sigma_c} P(\sigma,t)d\sigma \quad (1.15)$$

The amplitude of the mechanical noise D is proportional to the number of blocks rearranged during the time interval τ. The coupling parameter α in eq.1.15 is the control parameter of the model. It could be interpreted as corresponding to the intensity of the elastic coupling between sites. For small values of α, the system is jammed, with a vanishing activity $D = 0$. In this thesis, I will not directly use such a model for analyzing my data. I will rather focus on a simplified "mean-field" version of it, where a local variable $f(t)$ emerges macroscopically and represents a time dependent rate of stress relaxation. This variable is called "fluidity" and can be associated to the viscoelastic equation (eq.1.13) where $1/f(t)$ is identified with the relaxation time τ. Different authors have proposed a constitutive relation for the evolution of $f(t)$ [13, 69]. In the simplest version of this class of "fluidity model", the constitutive relation can be written in a phenomenological form "'a la landau" of the type :

$$\dot{f} = \Psi(f,\dot{\gamma}) \quad (1.16)$$

where $\Psi(f,\dot{\gamma})$ can be expanded in the relevant powers of the local fields f and $\dot{\gamma}$ (see details in refs [13, 69]). This type of model can capture aging and memory effects and provides prediction on the rheological equation at large deformation rates (Herschel-Buckley rheology). Recently, a non-local version of this model was proposed in order to include the effect of spatial nonlocal coupling on the relaxation process [52].

1.4 Effet des vibrations sur un milieu granulaire

In the industry, vibration is commonly used as a practical way to handle and transport particulate materials such as foodstuffs, coal, and pharmaceuticals etc... Vibration in granular matter

may also play an important role in natural events such as earthquakes and avalanches triggering. The behavior of granular medium under vibration is complex and was the subject of many experimental and theoretical studies. The interaction of various key parameters of the system creates a wide phenomenology such as fluidization, convection, segregation and avalanches. Here, we are only interested in the question of weak vibration, and its consequences on the rheology in the low shear rate regime.

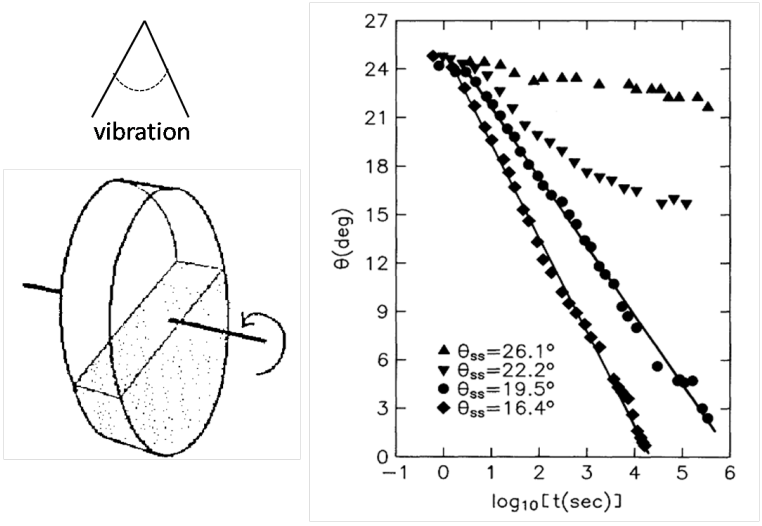

FIGURE 1.11: Schematic of a sand pile in a drum under vibration. A closed cylindrical drum (left) and the relaxation of θ in a stationary drum with glass beads. Vibration intensities increase from top to bottom, straight lines indicate $log(t)$ behavior (right) [40]

In 1989, Jaeger et al.[40] found that the slope of a sandpile may decay logarithmically when a weak level of vibrations is introduced via the forcing of sound waves coming from a loud-speaker. Their experimental setup, a rotating closed cylindrical drum, is shown on fig.1.11 (left). with no vibration, the stability of the pile is characterized by the avalanche maximal angle a steady state angle θ_{ss} for a steady rotation rate Ω and a relaxation angle after an avalanche (obtained in the limit when $\Omega \longrightarrow 0$). For an initial preparation at an angle $\theta(t=0) > \theta_r$ the vibration triggers an avalanching process. For an initial preparation at an angle $\theta(t=0) < \theta_r$ weaks vibrations trigger a slow relaxation logarithmic relaxation process. At a higher vibration level the time dependence of the relaxation process can be changed.

Furthermore, even under a low level of mechanical forcing, vibrations may influence directly the granular rheology. Recently, Caballero et al.[72] studied the sonofluidization of a granular packing. They monitored the motion of various intruders when sound waves are injected. The resulting effective friction coefficients were shown to decrease significantly with the vibration acceleration (see fig.1.12). Eventually, the Coulomb threshold was found to vanish and a linear relation between force and velocity was obtained. These relations strongly depend on the shape and the size of the intruders. On fig.1.12, is displayed the effective friction corresponding to the drag of a thread in the packing with no vibration and with vibration (in situ RMS acceleration $\gamma = 0.4g$).

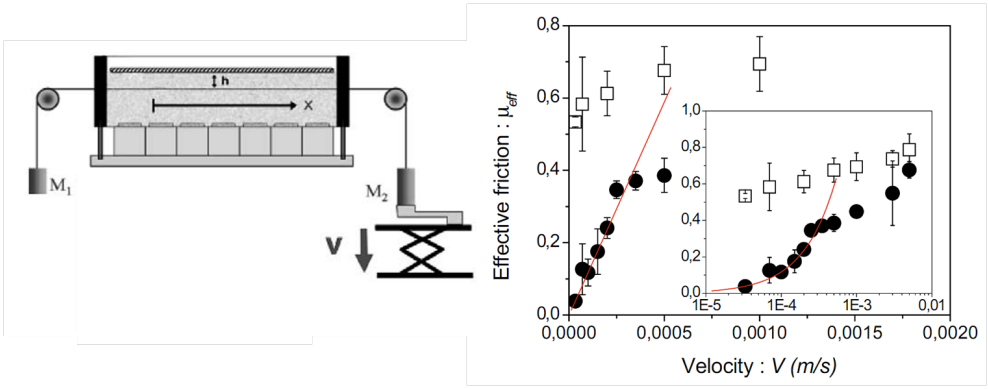

FIGURE 1.12: Rheology of a sonofluidized granular packing (after [72]). The driving of the intruding thread is at a constant velocity V, the masses are such that $M_2 > M_1$, the vibration is introduced by seven piezoelectric transducers at the bottom (left) and effective friction on the wire intruder μ_{eff} as a function of the pulling velocity; no vibration (open square) and with vibration (full circular), in the inset is the same graph but in a lin-log scale (right).

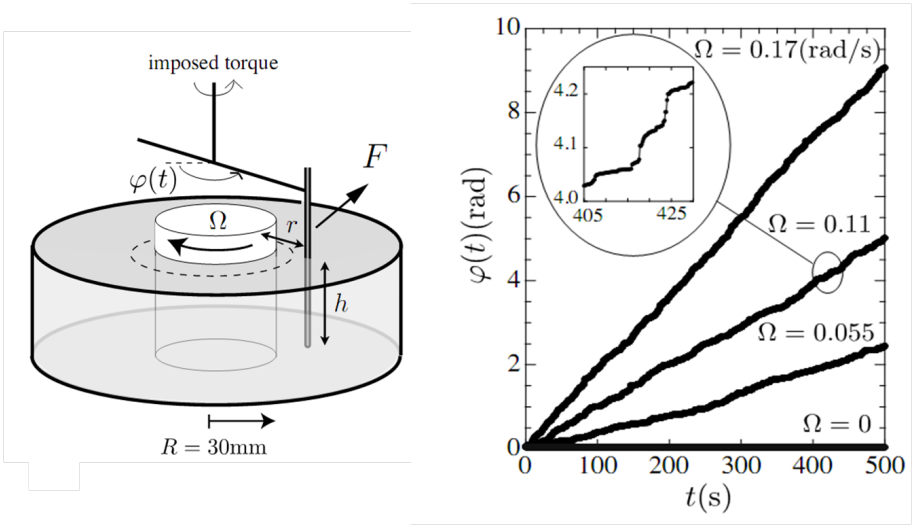

FIGURE 1.13: Experimental setup (left) and rod angular displacement $\varphi(t)$ for different Ω and at a fixed applied force (right) [47].

Other means of mechanical activation were proposed [10, 49, 47]. For example Nichol et al. [49] and Reddy et al.[47] used remoted shear bands noise as mechanical actuators for a granular packing. In particular, Reddy et al.[47] have shown that this type of forcing may modify the granular rheology (see fig.1.13). When a shear band is activated, the intruder far from the shear band, could move at a force F less than F_c, the force required to move the intruder in the absence of shear band. On short times scales, the motion of the rod is highly intermittent and consists of periods of slow creep followed by rapid moves (see the inset of fig.1.13 (right)). A linear relation between force and velocity was established as in a viscous fluid. So, from all these experiments, it appears that mechanical vibrations may phenomenologically play a role similar to temperature for thermalized states of matter. It may help to unjam a granular packing as temperature would do in the Liu

and Nagel qualitative jamming diagram. However, the fundamental activation mechanism and its precise role on the jamming onset as well as on the effective material rheology are still open issues.

1.5 Mécanismes de cohésion entre grains par capillarité

1.5.1 Granulaires mouillés non saturés

There are a numerous of studies on the role of the liquid content in wet granular medium [66, 78]. With a unsaturated granular, the liquid and the gas phases coexist in the pore space. On the basis of the amount of water trapped in a granular medium, one can distinguish different regimes (see fig.1.14).

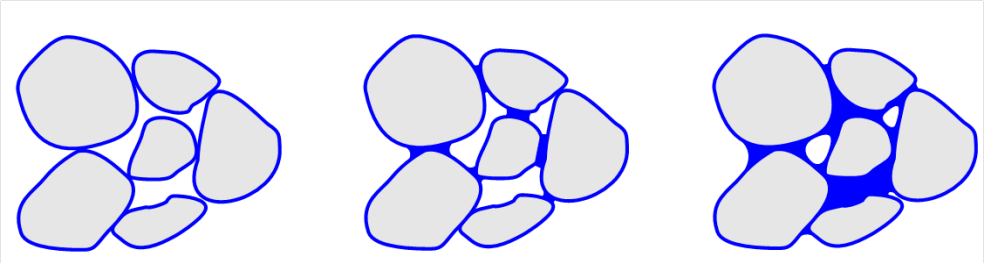

FIGURE 1.14: Different regimes of water trapped in a unsaturated granular packing, hygroscopic regime (left), pendular regime (middle) and funicular regime (right).

In the hygroscopic regime, the water is essentially retained by the rough asperity present at the granular surface. With an amount of water slightly larger, capillary bridges appear between the grains ; this is the pendular regime. At a higher water content, air can be trapped as bubbles and this state corresponds to the funicular regime.

1.5.2 Ponts capillaires : forces capillaires

The presence of small amount of liquid on the particle surface modifies important physical properties of the granular medium. For two grains in contact, if the amount of liquid is sufficient to form a liquid bridge at the contact point, the capillary cohesion force between the grains becomes :

$$F_{cap} = 2\pi\overline{\sigma}cos(\theta)R \tag{1.17}$$

where $\overline{\sigma}$ is the surface tension and θ the angle of partial wetting. Here we consider the case of two spherical grains of radius R. The striking results is that as soon as the volume of liquid trapped around the granular contacts is large enough to overflow the asperities, the capillary force becomes independant of the volume of the liquid bridge. If a pendular bridge is established between two separate grains or if two grains in contact separate due to packing reorganization, the inter-granular force diminishes and eventually the bridge become unstable and breaks. Note that in this case, the shape of the force curve and the breaking distance both depend on the amount of liquid in the bridge. See on fig.1.15 as an illustration, the measurement by Willet et al. [14] of the capillary forces arising from a microscopic pendular liquid bridges. The attractive forces is measured for two identical spheres as a function of the separation distance. They found a monotonic reduction in the force until the bridge rupture occurs.

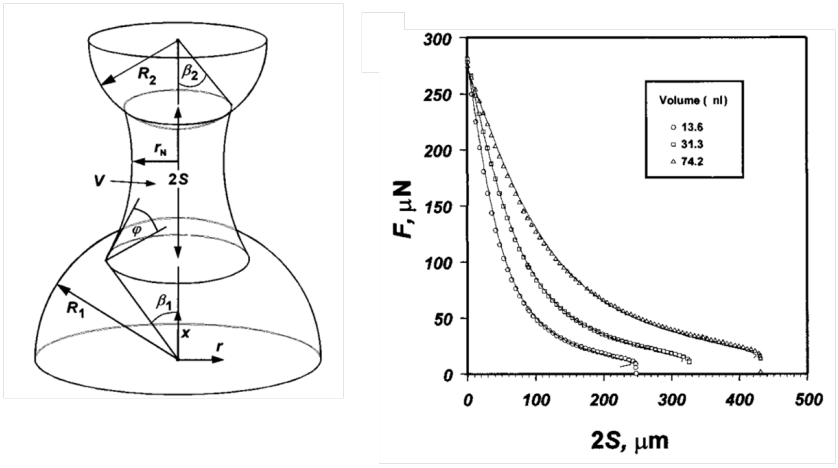

FIGURE 1.15: Schematic representation of a liquid bridge of volume V between two spheres of radii R_1 and R_2 separated by a distance $2S$ with a neck radius r_N, a liquid-solid contact angle θ and half-filling angles β_1 and β_2 (left). Measured capillary force (right) for different volumes in the liquid bridge as a function of the separation distance between the spheres , where the radii are $R_2 = R_1$. The curves represent the values calculated by a numerical solution of the Laplace-Young equation (after [14]).

In a packing of grains, the presence of water creates a distribution of capillary bridges. The increasing number of capillary bridges as a function of water content was studied by several authors [61, 95]. Fig.1.16 are displayed results from Scheel et al.[61] who used X-ray tomography technique and fluorescence microscopy on a wet packing to identify the number of capillary bridges and the total number of liquid clusters (defined as connected regions of liquid wetting more than two beads) as well as the volume of the biggest liquid cluster.

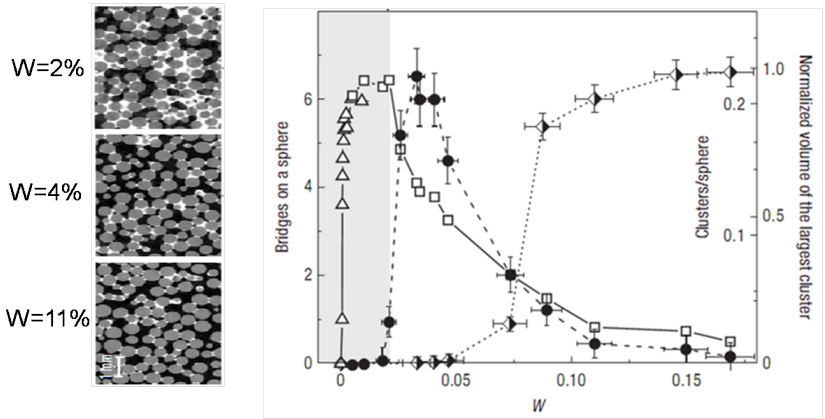

FIGURE 1.16: Images : Section through $3D$ X-Ray tomography of wet granular packing at water content $W = 2\%$, 4% and 11%, from top to bottom [61]. Main panel : Frequencies of liquid structure as extracted from X-ray tomography data. Left axis (open symbols) : Average number of capillary bridges on a sphere (triangles : fluorescence microscopy ; squares : X-ray tomography). Right axis : Average number of clusters per sphere (filled symbols) and normalized volume of the largest cluster (haft-filled symbols).

These quantities are shown as functions of the water content W in the packing. In this report, W is defined as the liquid volume divided by the total sample volume. As W increases, the liquid structures merge into larger clusters. At $W = 11\%$, the largest cluster contains about 90% of the liquid.

1.5.3 La cohésion macroscopique

Several studies were dedicated to the mecanical consequences of the presence of liquid in a granular packing, either experimentally [42, 91, 81, 61] or numerically [57, 56]. These studies show that cohesion increases with water content and eventually saturates to a value corresponding more or less, to a constant value of the number liquid of bridges per grain (about 6 according to Scheel et al. [61]). Then, increasing the water content will just increase the volume of the bridge but will not affect the capillary force as seen previously. This situation will last until the whole pore space is filled (funicular regime) and then, the cohesive force with start to decrease [81].

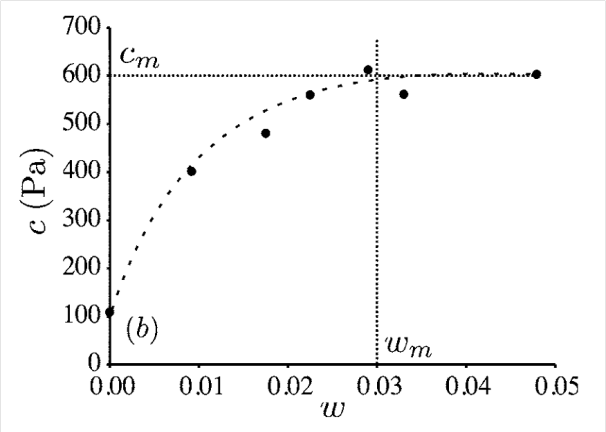

FIGURE 1.17: The Coulomb cohesion as a function of water content, the dashed line is drawn as a guide to the eyes [91]

Fig.1.17 are displayed experimental measurements obtained in a direct shear cell by Richefeu et al.[91] of the cohesion stress c of a wet granular materials as a function of water content With their preparation method, they found that the Coulomb cohesion (see eq.1.10) increases nonlinearly with W and saturates for a value of $W > 0.03$.

CHAPITRE 2

LA CELLULE DE CISAILLEMENT

Contents

2.1 Motivations

The work presented in this thesis focuses on the identification and characterization of some rheological properties of granular materials, whose experimental study is particularly delicate. For this reason, the first part of this thesis is devoted to the description of the experimental set-up that I built and developed during my thesis in the laboratory of Physics et Mécaniques des Milieux Hétérogènes (PMMH) at the ESPCI. The results obtained from the different experimental campaigns are presented and summarized in the following chapters.

The device is a shear apparatus which allows us to prepare granular packing at controlled packing fractions by using a fluidized bed technique. We added to the set-up two further possibilities in order to change the nature of the granular packing : external vibration and cohesion by changing the water content. This setup was especially designed to measure very small deformations and shear stresses. It can perform different types of tests : elastic response, response to a stress ramp and creep dynamics. We particularly focused on the study of the creep dynamic at a constant of shear stress by implementing a feedback technique.

2.2 Dispositif expérimental

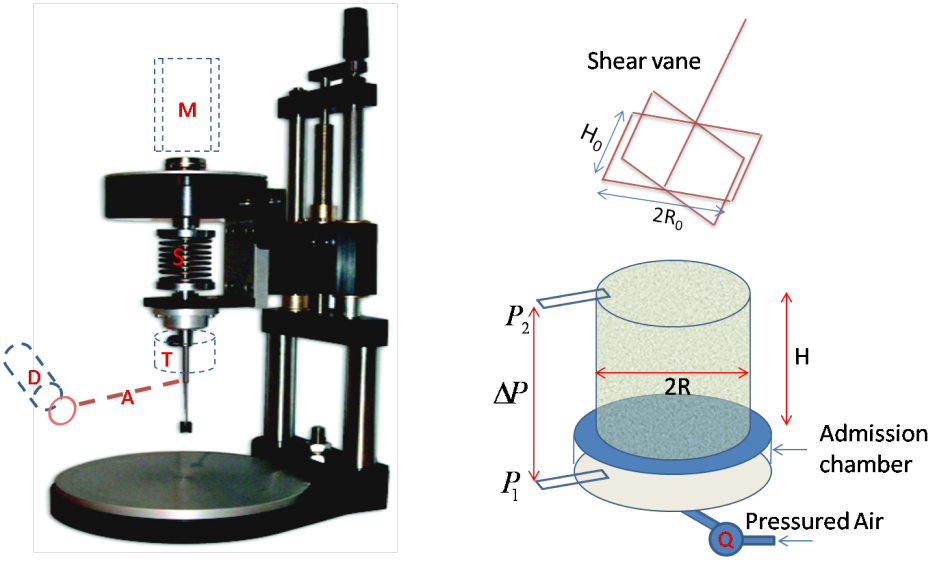

FIGURE 2.1: System of shear vane cell made industrially by Sols-Mesures (left) and schematics of shear vane and fluidization bed (right). (M) : motor, (S) : torsion spring, (T) : torque probe, (D) : induction distance probe, (A) : transversal arm, (Q) : flowmeter, P_1 : differential pressure probes.

The shear exerted on the granular material is obtained by rotation of a four blades vane (see fig.2.1 left) inserted inside the packing. The original shear vane system was bought from a company *Sols-Mesures* (*http ://www.sols-mesures.com/*) and we adapted this device to our needs. We fixed a brushless motor (M) on the top to command the rotation of the torsion spring (S), the motor rotation angle β can be imposed at a $2\pi/10000$ precision. At the end of the torsion spring, we mounted a sensitive torque probe (T) directly connected to the shear vane (see fig.2.1). To measure the rotation of the vane, we fixed radially an aluminum arm (A) and its displacement was moni-

tored by an induction distance probe (D). The system is made of iron with a stiffness of 200GPa. The whole system is well fixed on the table by a steel frame. The shear vane is in steel, the diameter of the axis is $3,3mm$, the blade height $H_0 = 2,54cm$ and the radial extension $R_0 = 1,27cm$ and the thickness of the blades is 0,5mm.

The grain container is designed as an air fluidized bed (fig.2.1 right). It is a plastic cylinder of inner diameter $D = 10cm$ and the cylinder height is $H = 10cm$. The cylinder is connected at its bottom to an admission chamber and is designed to produce an homogeneous flow of pressured air at the level of the separation metal grid. The mesh of the metal grid is $10\mu m$, small enough to block the grains (see fig.2.2).

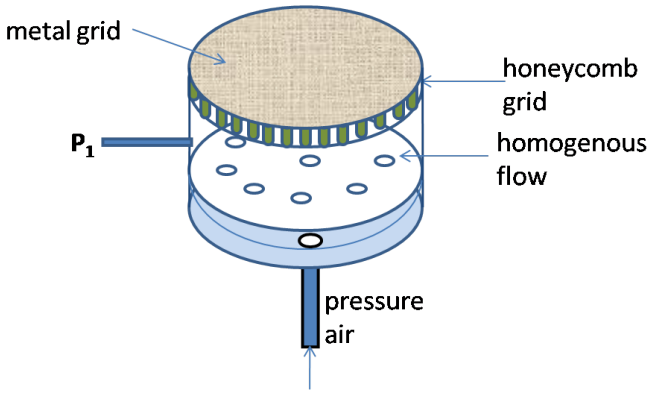

FIGURE 2.2: Admission chamber of the fluidization bed

Pressured air is introduced at the bottom of the admission chamber and just below the honeycomb grid, we placed a differential pressure probe to obtain a measurements of the pressure drop $\Delta P = P_1 - P_2$ between the bottom and the top of the packing. In this study we used glass beads from *SiLibeads (www.sigmund-lindner.com)* with a density of $\rho = 2500kg/m^3$ and a mean diameter $d = 200\mu m$ (R.M.S. polydispersity $\Delta d = 30\mu m$), we could not make any detailled characterization of the roughness (a difficult issue indeed).

2.2.1 Compacité contrôlée par la méthode de tapping

To produce granular packing at a fixed packing fraction and obtain reproducible results on the mechanical tests, we elaborated a well defined preparation protocol. First, to assure that the granular medium was completely dry, we store the granular material at $50°C$ in a stove. Then, for each experiment, the granular material is removed from the stove and left in open air for about 30 minutes to come back to room temperature (about $20 \pm 5°C$). The airflow in the fluidized bed, is powered by the ESPCI compressed air system (5 Bar). A fixed air flow rate can be maintained and controlled using valves and a flow-meter (range 25 L.min^{-1}). Prior to the filling process, the container is placed on an electronic scale and at its top, a plastic cylinder of the same inner-diameter is adjusted so that, it just prolongates the tube. Then, the air-flow is switched-on at $Q = 15\ l/min$, a value just below the fluidization threshold. The pouring of the grains is done changing the position of the source to spread evenly the quantity of grains on the surface (fig.2.3). The filling is stopped at each granular height increment corresponding to $2cm$ roughly. Then, using a wooden stick, a tapping of the walls is performed in order to compact the grains. At each height increment, the number of taps is the same (10) but the energy of each tap has to be increased to reach denser

compaction. The process is repeated until the top of the container is reached (the extension cylinder is partially filled). Then the air-flow is switched-off, the extension cylinder is removed and the grains at a height larger than the container height $H = 10cm$ are also removed using a ruler, leaving a flat surface at he top. Finally, the mass M of grains contained in the cylinder of diameter $D = 2R$ and height H is measured, which provides a good and precise value for the average compaction :

$$\phi = \frac{M}{\pi R^2 H \rho} \tag{2.1}$$

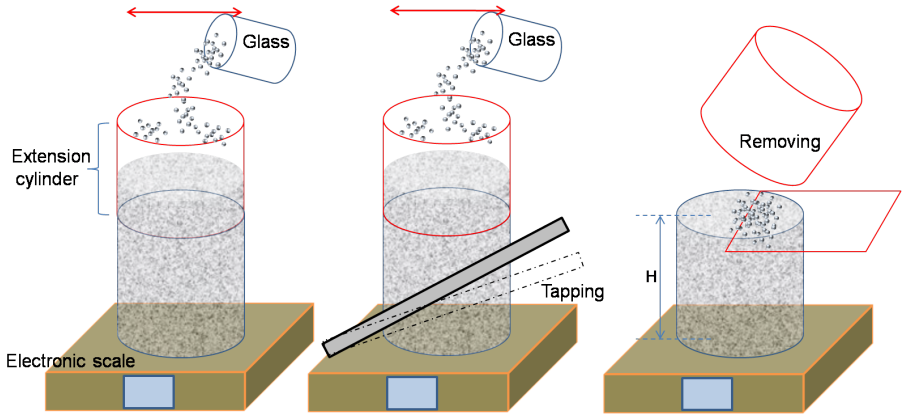

FIGURE 2.3: *Sample preparation*, pluviation of grains to have a loose packing (left), tapping around the cylinder to reach a higher packing fraction (middle) and removing the extension container (right).

I found that using this method, I could obtain a range of packing fractions between *0.56* and *0.63*. The relation between intensity of the tapping and the final value of the compaction remains little bit qualitative but it is remarkable that with some practice I could reach rather predictable values of compaction with a good accuracy. Note however that this is true in a rather dry environment (humidity about 35 %), I noticed that with high humity the final value of compacity has a tendency to decrease at the same tap intensity. Further more I made some trial changing the tapping position on the container but I found no change in the final result.

2.2.2 Permeability as a function of packing fraction

.

In the following, we present a calibration curve that I established to relate the porous material permeability $K(\phi)$ to the packing fraction. I found this relation very useful as it provides a practical way to relate the pressure drop on both sides of the packing to the actual compaction. Then it is quite easy to check if the mechanical tests have led to any change in compaction or in some cases, to handle granular packing with a height which is not necessarily the container height H. From Darcy' Law[5], we have the relation :

$$K\frac{\Delta P}{H} = \eta\frac{Q}{S} \tag{2.2}$$

where Q is volumetric flux, K is permeability; H is height of column (between inlet and outlet), S is the area of the cross section and the pressure drop ΔP as measured with the pressure probe,

η is the dynamic viscosity of dry air. With our experiment set-up, we measured the flow rate Q by using flow-meter and the pressure difference ΔP between the two ends of the cylinder by using the pressure probes as a function of average velocity of air $U = Q/S$. Note that for these control measurements, the fluxe values are much lower than the fludization threshold. On fig.2.4 (left), is displayed for different packing fractions determined from the method described in the previous section, the relation between the pressure drop and the flow rate Q. The relation is linear :

$$\Delta P = \lambda.Q \text{ with } Q = U.S \tag{2.3}$$

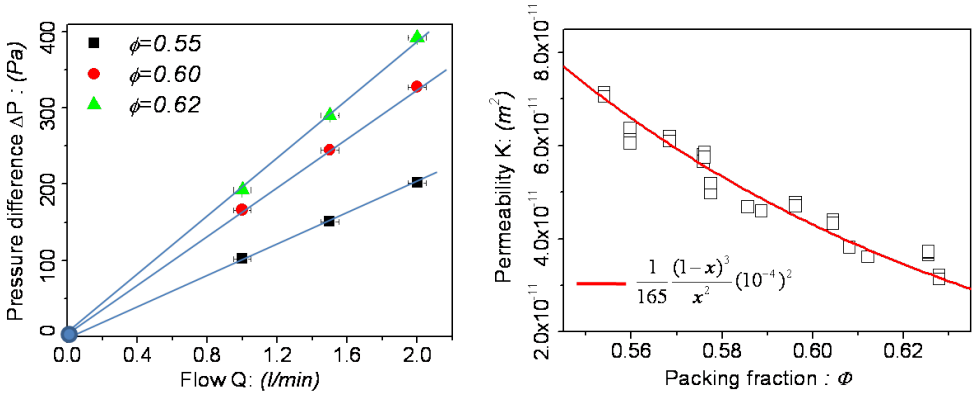

FIGURE 2.4: Pressure difference as a function of the flow rate, with different packing fractions (left)and permeability as a function of the packing fraction (right).

Therefore, from the fitted slope to get λ, one can determine the permeability :

$$K = \frac{\eta H}{S\lambda} \tag{2.4}$$

The value for the air viscosity at $20°C$ is $\eta = 1.8510^{-5}$. Fig.2.4 (right) is displayed the relation between K and ϕ. It can be fitted using a classical Kozeny-Carman (KC) equation [5] :

$$K(\phi) = A\frac{(1-\phi)^3}{\phi^2}d^2 \tag{2.5}$$

with one adjusting parameter $A = 165$. This last relation determines our calibration curve. Now for any granular mass M poured in the container, if one measures the linear pressure drop characterized by the slope λ, one can compute the actual packing fraction from the relation :

$$K(\phi)\ \phi = \eta\frac{4\ M}{\lambda\pi D^2\rho} \tag{2.6}$$

This determination is displayed on fig.2.5.

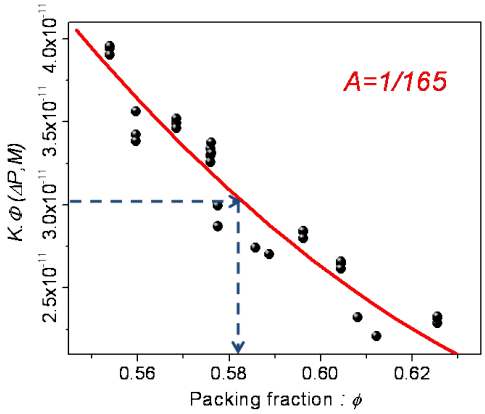

FIGURE 2.5: Relation between $K(\phi)\phi$ and ϕ, the solid line is calculated from eq2.6 with parameter $A = 165$.

Importantly, this relation is valid as long as the fluidization threshold is not reached that we estimated at a value slightly larger that $Q = 15 l/min$ (flux chosen for the preparation procedure).

2.2.3 Préparation d'un échantillon avant les tests mécaniques

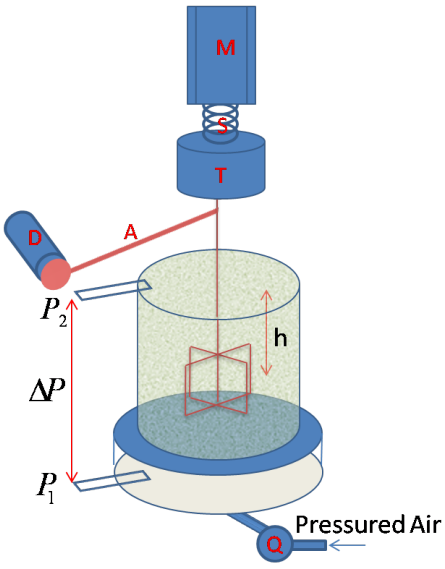

FIGURE 2.6: Schematics of the shear cell after installation all the probes and insertion of the shear vane at a depth h.

The experimental procedure to prepare the granular packing before the application of the mechanical tests can be divided into several steps. The first one has been described in a previous section, it consists in preparing on an electronic scale, a sample of mass M at a controlled packing fraction using the tapping method (see eq.2.1). Then, the fluidized bed is transfered below the test apparatus at a well defined position such that the cylinder symmetry axis corresponds to the axis

of the shear vane. Thereafter, the air flow is switched-on at a value $Q = 15(l/min)$ (below the fluidization threshold) to release as much as we can the compression due to gravity. This last condition is essential as it allows the insertion of the shear vane at the right position i.e. at a depth $h = 5cm$ for most experiments (see fig.2.6). Furthermore, in the experimental campaign where the granular material is vibrated, the piezo-transducers and the accelerometer are inserted during this phase. I tested that working this way, the packing fraction did not vary and this led to reproducible mechanical results. After preparation and installation, the air flux is switched-off and the system is left still for about ten minutes before the onset of the mechanical tests.

2.2.4 Mesure de la contrainte de cisaillement

.

To measure the shear stresses applied on the sample by the shear vane, we use a torque probe of range 0.2 Nm (*http ://www.tme-france.com/*). This probe has a high precision 10^{-5} N.m and is directly connected to the shear vane and to the torsion spring (fig.2.1).

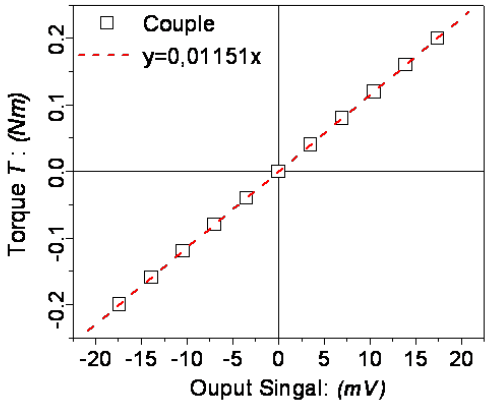

FIGURE 2.7: Calibration of the torque probe by the manufacturer. The torque T varies linearly with output signal.

.

From the torque measurements, we defined the value of the mean shear stress σ at a radial distance R_0 over a surface corresponding to the blade height H_0 :

$$\sigma = \frac{T}{2\pi R_0^2 H_0} \tag{2.7}$$

By torque conservation, the mean shear stress in the granular packing varies with the distance r from the center as :

$$\sigma_{(r)} = \sigma(\frac{R_0}{r})^2 \tag{2.8}$$

2.2.5 Mesure de la déformation

In this set-up configuration, we do not have a direct access to the local deformation field. However, the mean shear deformation γ, (fig.2.8) is related to the angular rotation α of the shear vane

and we define it as :

$$\gamma = \frac{\alpha R_0}{R - R_0} \tag{2.9}$$

The rotation α is obtained using the induction probe (D) positioned close to the radial arm (A) at a distance l from the axis (see fig.2.8 left). The displacement Δl is measured and then :

$$\alpha = \frac{\Delta l}{l} \tag{2.10}$$

Note that the measurements are based on the position of a conductive target (the arm) in an open magnetic circuit of high permeability (the probe) creating then an inductance change caused by a metal object in a magnetic field. The target used in our setup is made of duralumin. The induction probe has a typical measuring range of $2mm$. Note that we can vary the deformation measurement range by moving the induction probe along the arm. On fig.2.8 (right), we present two calibration curves relating the probe displacement Δl to the electric tension V measured as the probe signal. The first calibration points (symbols) are obtained with a linear micro-metric stage moving the probe position. The second points (blue line) where obtained by the controlled rotation of the motor (no spring, direct connection) which rotates the arm. The probe is situated at a distance $l = 19cm$ which corresponds to the typical range of deformation measurements. We see that except in the two extremes of the measurement range both results agree with a linear relation (no detectable influence of the surfaces angular position). Note that before each measurement, I always positioned the induction probe such as its surface was parallel to the transversal arm and at the same initial distance for all the tests $\Delta l_0 = 0.4mm$. From the linear fit and also the constructor's specification one can estimate the precision of the displacement to be 0.1 μm :

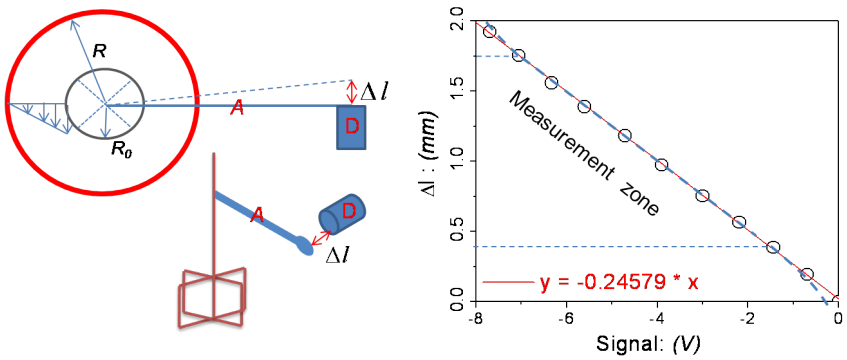

FIGURE 2.8: *Calibration of the induction probe.* Experimental setup where (D)is the induction distance probe, (A)is the transversal arm (left), relation between the displacement measured and the output signal in two cases : the probe surface and transversal arm are parallel (red line) and not parallel because of a rotation of the transversal arm (blue dot line) (right).

Note that the advantage of this typoe of probe are :
- A very good precision (but however a short range).
- No friction between the probe and the device.
- A fast response time, enabling the study of very short rheological transitions.

2.2.6 Système d'acquisition

On fig.2.9, we show a schematic of the acquisition chain. The experiment is monitored and controlled by computer using a 'LabView' system allowing data acquisition and output transfer of information after processing. 'LabView' was a parallel system dedicated to acquire and to save the signals from each probe. The system includes a data acquisition system, equipped with 12 channels. This unit enables simultaneous acquisition of a large number of channels with frequencies from $1Hz$ to $10kHz$. In the case of standard utilization, resolution on the analog signal from $0V$ to $10V$ was $0.03mV$. The tensions coming from the induction and the torque probes are input signals. They are processed by Labview to yield the deformation γ and the stress σ (see fig.2.9). In parallel, we used a software (sim 2) to control well the motor speed and to pilot the direction rotation. Thanks to this set-up, we can acquire all the signals at the same times, which allows us to have the relationship between the shear stress and the stress strain corresponding to each motor speed.

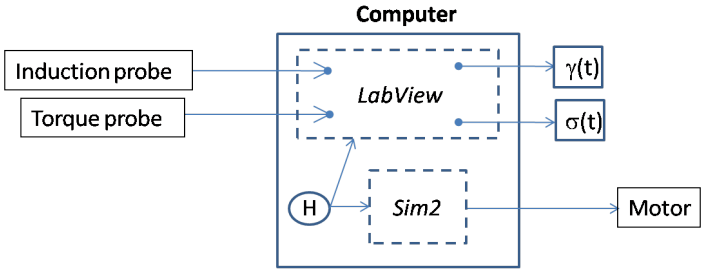

FIGURE 2.9: Schematic of the acquisition system, with the same times scale (H) for all the signals.

The motor is driven directly by the computer and it can be monitored by Labview to perform a feed-back loops between the shear stress and the motor rotation (fig.2.10). The feed-back loop is used to perform a creep tests at a constant shear stress (we present in detail in chapter.3).

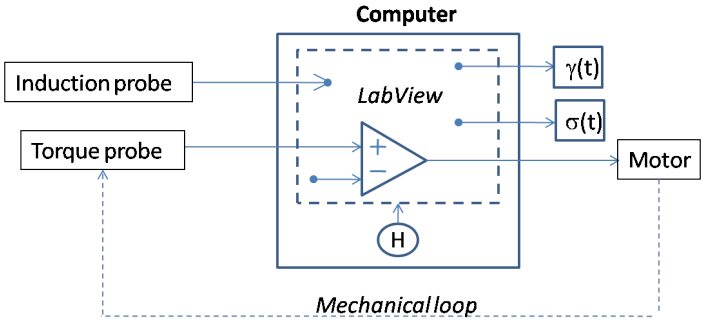

FIGURE 2.10: Schematic of the acquisition system is used to perform a creep tests.

Fig.2.11 shows an example when the system is stationary and with no external stress. We find that the noise of the deformation and shear stress is stable and very small. This noise can be interpreted by the electrical noise or may be by the mechanical noise in the laboratory.

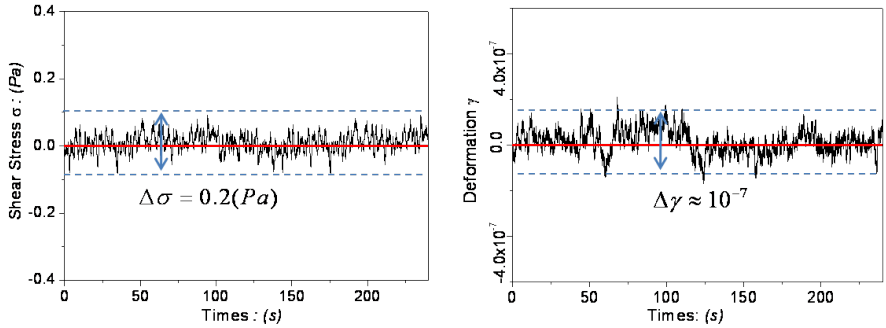

FIGURE 2.11: Output signals recorded after averaging smoothing of $0,5s$ with a acquisition frequency of $41Hz$, torque probe signal (left) and induction probe signal (right) are obtained without any external stress.

2.3 Empilement granulaire sous faible vibration

2.3.1 Activateurs piézoélectriques

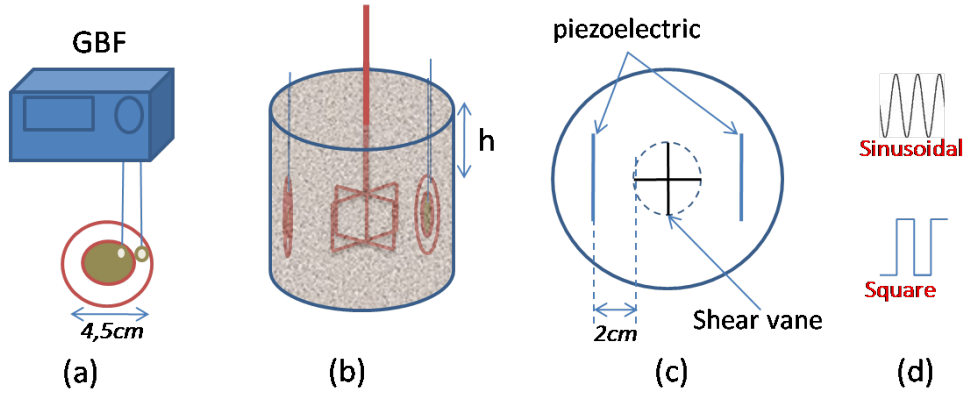

FIGURE 2.12: GBF control the input signal (a), experimental set-up used for the vibration experiment with two piezoelectrics are introduced at the same depth of the shear vane (b, c) and symbols for two types of vibration : sinusoidal and square tension input (d).

We have seen in the introduction chapter that in previous works, several options have been proposed to produce vibrations in a granular packing [40, 53, 72]. In the following study, we use piezoelectric transducers as in [72] which generate easily a reproducible level of vibration induced by sound propagation. The vibration is weak and adjustable in frequency (between 100 Hz and 10000 Hz) and in amplitude varying the voltage input between 0 and 10 Volts, all the parameters are tunable by a "*Générateur de basses fréquences (GBF)*" (fig.2.12 a). On fig.2.12, we display a schematic of the piezo-transducer (*www.radiospares.com*), the cylindrical piezo-ceramic is mounted on a circular bronze foil of diameter $4.5cm$. The small overall thickness of $0.2mm$ of the whole device allows an easy insertion in the packing (see preparation procedure). In the study presented in chapter 4, the vibrations were produced by inserting two transducers in a radially symmetric

position (see fig.2.12 b, c). The activation surfaces are perpendicular to the radial direction and we manage to activate both transducers in phase opposition.

2.3.2 Accélération

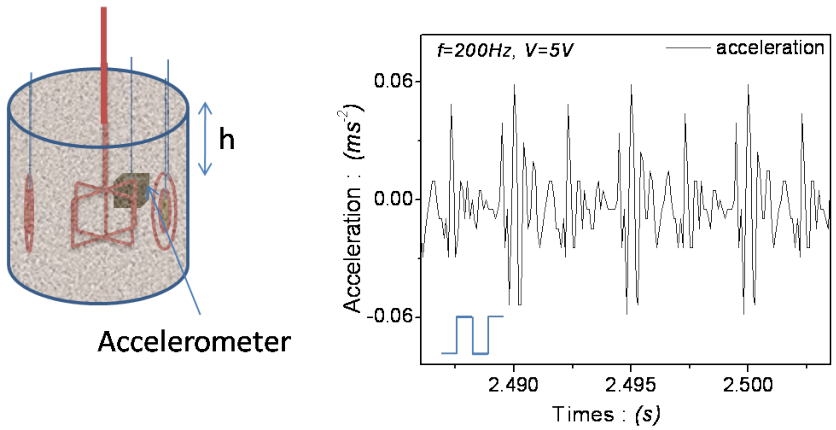

FIGURE 2.13: Two piezoelectrics are introduced at the same depth of the shear vane and the accelerometer (left) and acceleration measured by the accelerometer buried in the packing for a signal of frequency $f = 200Hz$ and square voltage $V = 5V$ (right).

With this setup, agitation in the granular medium was completely disordered and very low in comparison with the accelerometer gravity g. With a low excitation, the main excitation mode in the system was the rotation of grains and the reorganization of granular contacts. To measure the acceleration as a function of the input signal : the frequency and the electrical tension, we used a very sensitive piezoelectric accelerometer (500 mV.g^{-1}), (Brüel and Kjaer instruments). This is a single-axis sensor, used as a reference to monitor the intensity of piezoelectric transducers. According to the model, the sensor size was $1cm$ square (fig.2.13). Considering grains $0.2mm$ in diameter and a cylindrical accelerometer $1cm$ in diameter and $1cm$ in height, the number of grains in contact with the accelerometer was about 3×10^4, which allows us to have a very efficient average. There were of course some drawbacks with this type of accelerometer. In particular, we must take extreme care for this implantation in the granular medium, in order to avoid disturbance the preparation by creating heterogeneities. Fig.2.13 (right) shows a typical measure of acceleration for an input square signal of frequency $f = 200Hz$ and voltage $U = 5V$.

In our study, the select parameter was the root mean squared (R.M.S) acceleration Γ induced in the granular packing, calculated by means of the acceleration measured in the bulk. To acquire all the signal of vibration, we must work with very high frequency of acquisition (up to $10kHz$), the value of Γ is compute by Labview from this data. We also studied the spectra of vibration with two types of vibration : square and sinusoidal vibration. An example is shown on fig.2.14.

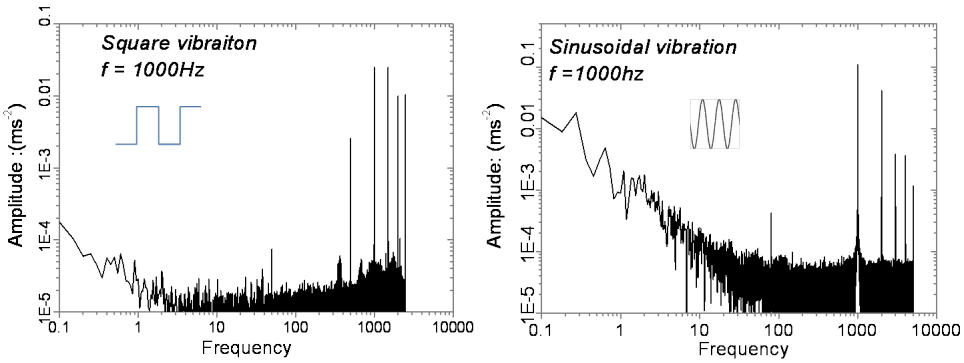

FIGURE 2.14: Amplitude of signal as a function of frequency with frequency $f = 1000Hz$, square tension input (left) and sinusoidal tension input (right).

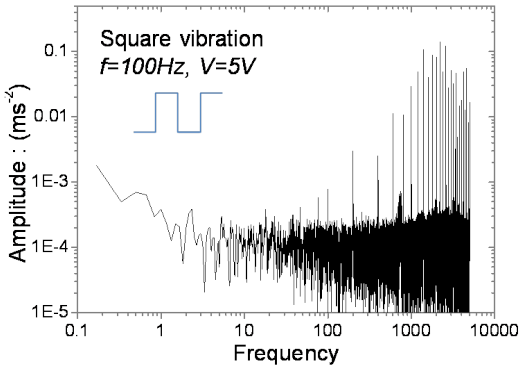

FIGURE 2.15: Amplitude of signal as a function of frequency with frequency $f = 100Hz$ and square tension input $5V$.

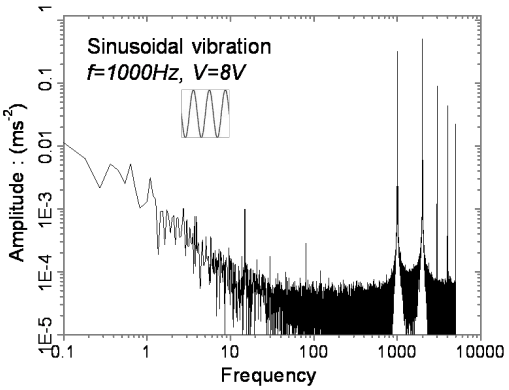

FIGURE 2.16: Amplitude of signal as a function of frequency with frequency $f = 1000Hz$ and sinusoidal tension input $8V$.

We found that at a same frequency input, with a square tension input, the vibration spectra was larger than with the sinusoidal tension input. Fig.2.17 shows clearly the harmonic output signal of acceleration according to the sinusoidal tension input $3V$, a resonance frequency of $f = 1000Hz$ is observed.

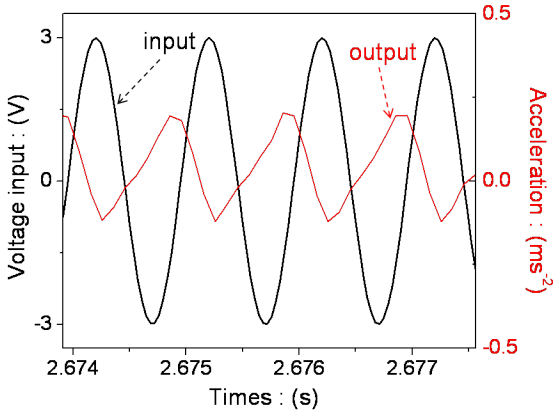

FIGURE 2.17: Sinusoidal tension input $V = 3(V)$ with frequency $f = 1000Hz$ (black) and correspondent output of acceleration (red).

With a frequency of $f = 1000Hz$ and a sinusoidal tension input, we found that at low voltage input the response of material is harmonic and the resonance frequency is $1000Hz$. When $V > 6V$, the spectra became large and the resonance frequency of packing is at $2000Hz$ (fig.2.16). Fig.2.18 shows the relationship between the the amplitude obtained from a FFT analyze as a function of the sinusoidal voltage input according to the frequency input $f = 1000Hz$. We found also a transition around $6V$. When $V < 6V$, a linear relation was observed. It is corresponding to the vibration spectra response. With a square tension input and a frequency of $100Hz$, the spectra response is very large (fig.2.15).

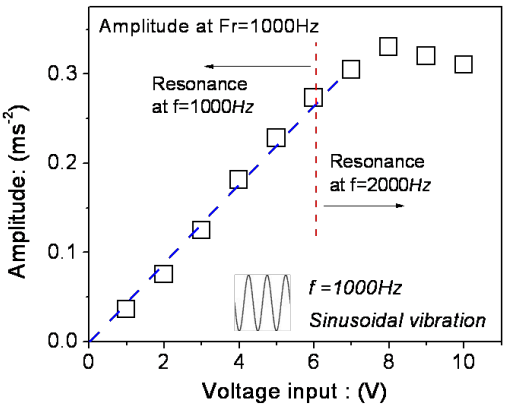

FIGURE 2.18: Amplitude obtained from a FFT analyze at $f = 1000Hz$ as a function of the sinusoidal voltage input, with a frequency input at $f = 1000Hz$. The dashed line is linear fit.

2.3.3 Calibration du RMS d'accélération pour une tension entrée créneau

In this section, we present the calibration curve of the vibration intensity according to the square tension input. The vibration spectra according this signal is large (see FFT on the fig2.14 (right)). We obtained, the value of r.m.s acceleration Γ, for different frequencies and voltages applied to the piezoelectric transducers. Fig.2.19 (right) shows how the r.m.s acceleration measured in the bulk dependend on the input singal voltage. Measurements were done at $f = 100Hz$ and packing fraction $\phi = 0.625$. The different behavior for low and high voltage are noteworthy, with a transition around $6V$. This phenomena might correspond to the threshold voltage at which the transducer manage to break the force network between the grains and the wall of the cylinder. With the voltage input is inferior of $6V$, we found the linear relation between Γ and voltage input.

On fig.2.19(left), we show the r.m.s acceleration as a function of the frequency with a square voltage input of $5V$. We found that the maximum value of vibration $\Gamma = 0.17g$ (g is the gravity acceleration) corresponding to the frequency around $\approx 2,5kH$.

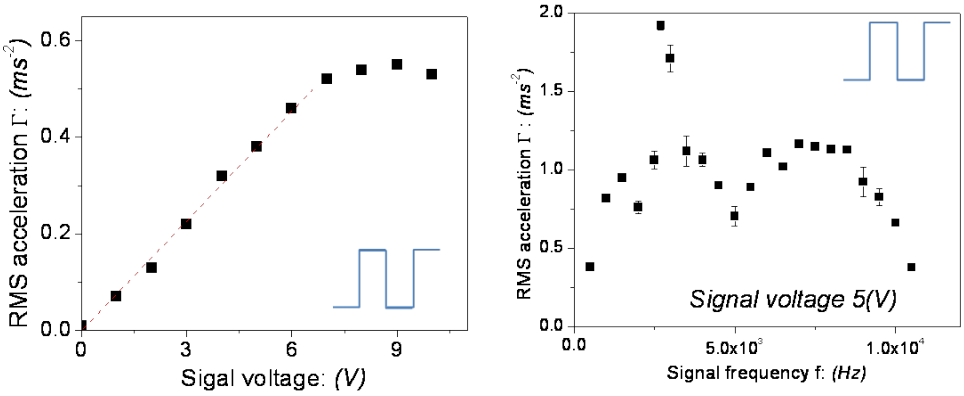

FIGURE 2.19: Roof mean square acceleration as a function of voltage according to the input signal frequency $f = 100Hz$, fit line : y=0.076x (left) and roof mean square acceleration as a function of signal frequency according to the input signal voltage $V = 5V$ (right). The packing fraction is $\phi = 0.625$, the accelerometer was placed at a depth of $5cm$, exciting tension shape is square.

2.3.4 Calibration du RMS d'accélération pour une tension entrée sinusoïde

In this section, we present the response of a granular medium to a sinusoidal tension input. A piezoelectric vibration provides an horizontal sinusoidal amplitude Z_0 and frequency f. The movement of the piezoelectric follows a law given by :

$$z = z_0.\sin(\varpi t) \tag{2.11}$$

with ϖ is pulsation ($\omega = 2\pi f$), then, we calculated the r.m.s acceleration Γ :

$$\Gamma = \|\gamma\| \text{ with } \gamma = \ddot{z} = -z_0\omega^2\sin(\omega t) \tag{2.12}$$

Fig.2.20 (left) shows the quad-rate relation between the r.m.s acceleration and the voltage input for different of frequencies. Fig.2.20 (right) shows the relation between the r.m.s acceleration and the frequency at a sinusoidal voltage input of $3V$. Interestingly, the resonance frequency at $f \approx$

$2,5kH$ was observed, this is the same resonance frequency with the case of square tension input. For a sinusoidal vibration, the relationship between and f seem to indicate also a cube relation for $f < 2500Hz$ (see fig2.20 right).

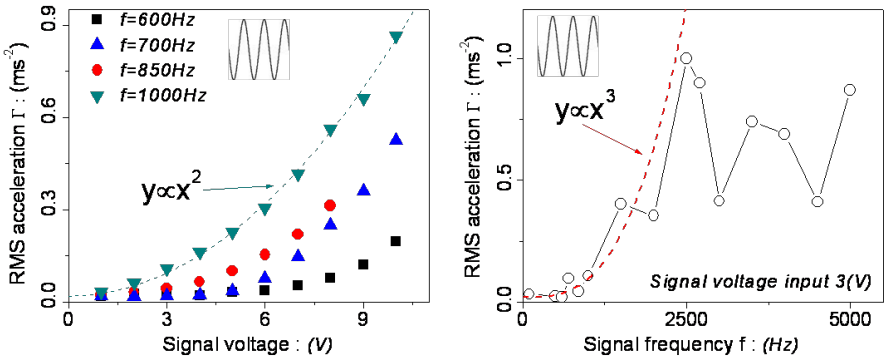

FIGURE 2.20: Roof mean square acceleration as a function of voltage for different frequencies (left) and roof mean square acceleration as a function of signal frequency with input signal voltage $V = 3V$ (right). The packing fraction was $\phi = 0.60$ and the accelerometer was placed at a depth of $5cm$, and the excited tension was sinusoidal.

2.3.5 Homogénéité du RMS d'accélération

To verify the homogeneity of vibration in the granular packing, we measured the root mean squared acceleration Γ at different depths for different packing fractions (fig.2.21). We found vibration intensive is homogeneous in the bulk from the depth of $2,5cm$. We checked in two cases of packing fraction : the densest $\phi = 0.623$ and the loosest $\phi = 0.57$. We did not detect the different of r.m.s accelerations according the same input signal voltage and frequency.

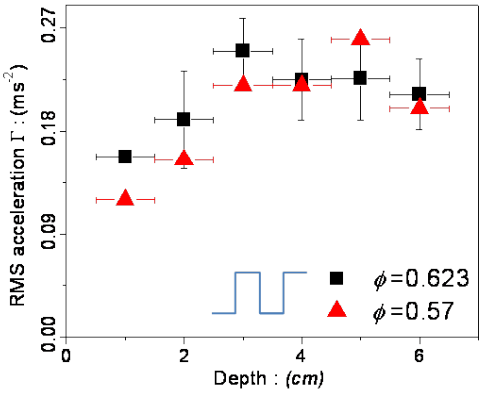

FIGURE 2.21: RMS acceleration as a function of depth below the surface with input signal frequency $f = 100HZ$ and square voltage $V = 3V$ for packing fraction $\phi = 0.623$ and $\phi = 0.570$.

The result on the fig.2.21 allows us to use the calibration curve of r.m.s acceleration as a function of voltage input for all the value of packing fraction.

2.4 Empilement granulaire humide

It appears logical to start by investigating how the granular medium acquires its amount of water as described by a water content, i.e how water is introduced within into the granular material. When a dry granular material and water are brought into contact, water soaked into the granular pile by means of capillary forces. This process is commonly called spontaneous imbibition, and one might ask to what extent the structure of the imbibition and the final distribution of liquid occur within the granular material. The process of imbibition of a liquid into a random medium also plays a key role in many other problems of general interest, such as oil recovery, or irrigation in agriculture. The shaking method was already used to make wet sample [91, 61]. In our study, with a granular packing at a well defined packing fraction ϕ, the process of imbibition was controled by passing the humid air through the sample. And the humid air was produced by air through water.

2.4.1 Dispositif expérimental utilisé pour obtenir un flux d'air humide

A schematic representation of the set-up is shown on fig.2.22 : a shear vane cell installed with two humidity probes and a flux bubble system. The bubble system constituted a 'heating element' which heated the water and a 'bubble air container' which allows air to pass through warm water. One humidity probe was located inside the cylinder to measure the relative humidity ($RH(\%)$) and temperature before passing through the sample, the second probe was located at the top of the sample and measure $RH\%$ of humid air flow after passing through the sample.

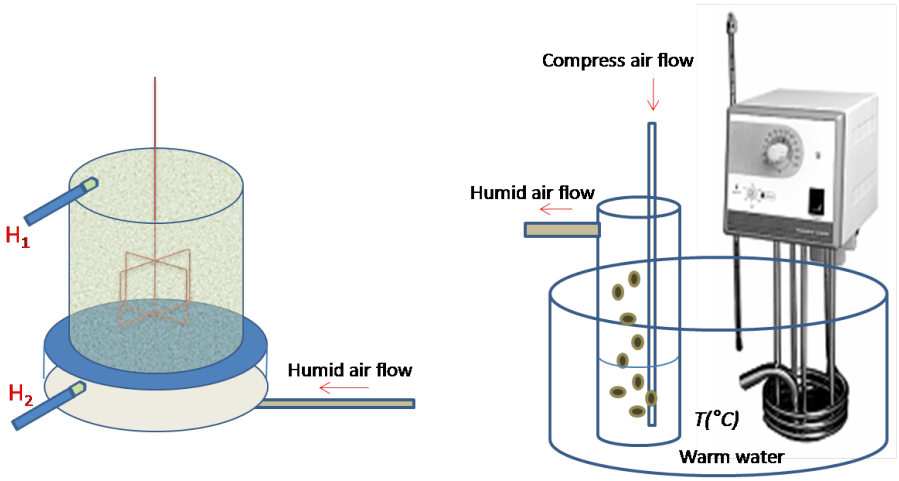

FIGURE 2.22: *Experimental se-tup*. Shear vane cell with two humidity probes(H) (left) and bubbling system for producing the humid air flow (right).

First of all, we heated the water by using the 'heating element' to a desired temperature between $20°C$ and $100°C$. Then, the dry air passed through this water with a very low flow $Q \approx 2l/min$ in order to obtain the humid air flux. A stationary relative humidity was thus reached within a few minutes. We started our calibration when this stationary level was obtained. Using the relative humidity probe, we measured the RH between 80% and 100%. With a bubbling temperature of $30°C$,

RH = 100% already reached (fig2.23 (left)). Then, weak fluxes of humid air is set to flow through the cylinder from the bottom to the top, maintaining a constant and homogeneous level of humidity. We found that at a room temperature of about $20 \pm 5°C$, the temperature of humid air was not changed until it reached the sample.

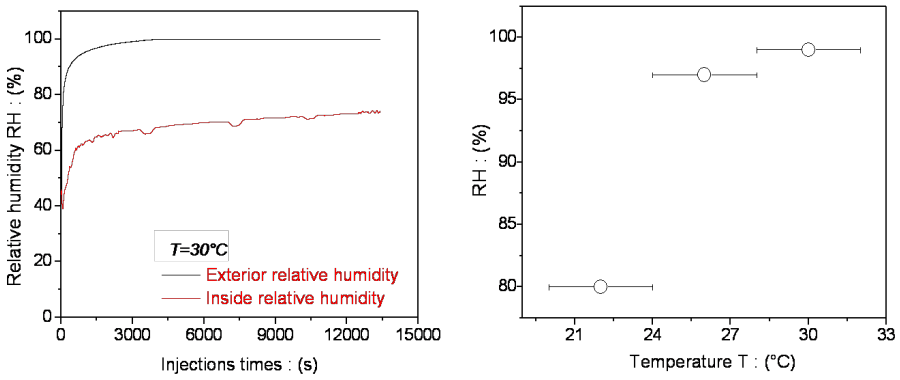

FIGURE 2.23: *Relative humidity of humid air flow*. Evolution of relative humidity of humid air flow before and after going through the sample with a temperature of water of $30°C$ (left) and dependence of maximum relative humidity according to the temperature of bubbling (right).

Fig.2.23 (left) shows that a stationary $RH\%$ reached after about 10 minutes. This figure shows also a decrease of 20% for RH between the bottom and the top of the cylinder. Moreover, the stationary value of RH also depends on the temperature of bubbling as described on fig.2.23 (right).

2.4.2 Mesure de la quantité d'eau

The water content was determined by comparing the mass of a sample of the material before and after injection of humid air. After injection of humid air, we collected about $10g$ of granular material and heated it up to $200°C$ using a balance equipped with a dessicator. Thus, the total mass of grains and water decreased with dessication times due to the evaporation of water until a constant mass corresponding to the mass of dry grains. The analogue output of the dessicator was connected to a PC, which continuously recorded the weight loss i.e the amount of water removed with a precision of about 0.005% (fig.2.24). In this study, the water content is given by $W = m_w / m_s$, where m_w and m_s are the masses of water and grains, respectively.

In our study, when the desired water content is reached, we stop the humid air injection and the experiments are performed at ambient conditions. The loss of water content never exceeds 2% for a $2h$ experiment under ambient conditions. This loss was only due to evaporation, it was small enough to assume a constant water volume in the packing.

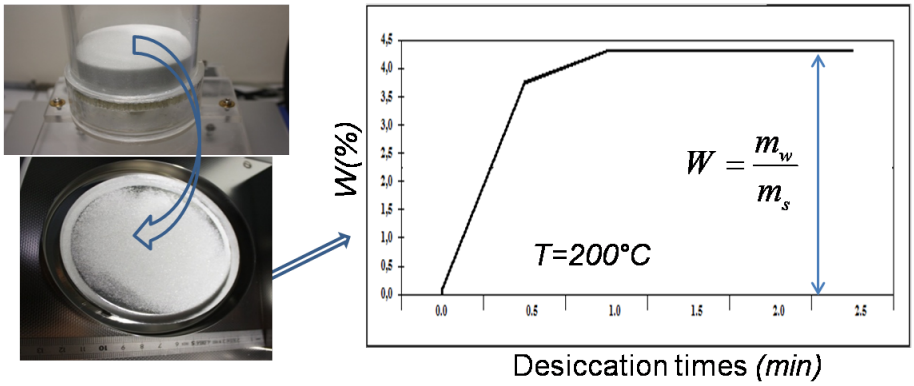

FIGURE 2.24: Granular sample and dessicator interior (left) and the water content $W\%$ as a function of dessication times with $200^{\circ}C$, the plateau corresponded to the mass of dry grains (right).

2.4.3 Influence du gradient de température

When we increased the temperature of water up to $80^{\circ}C$, the water content was not homogeneous in the cylinder. We measured the water content as a function of depths for a sample with a height of $5cm$. We measured from the sample surface $z = 0$ to the sample bottom $z = 5cm$. Fig.2.25 shows that the water content increased with depth and duration of injection times. Interestingly, the amount of water seems to increase linearly with air flux at the different depths.

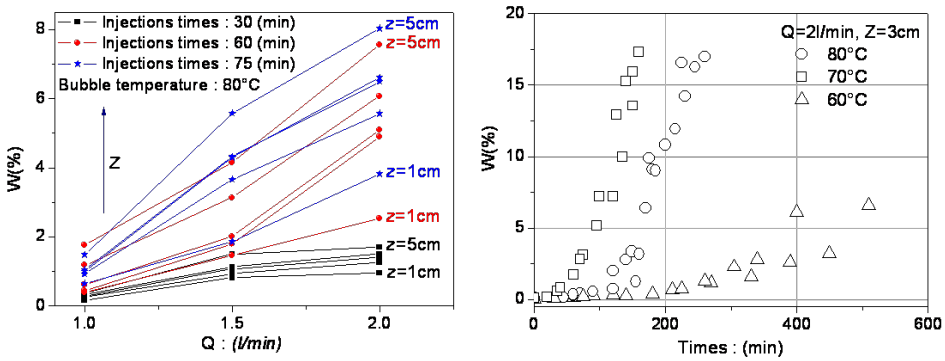

FIGURE 2.25: Water content (W) as a function of air flux (Q) at different depths below the surface z, and for different of injections times with a bubbling temperature at $80^{\circ}C$ (left) and water content as a function of injections times for three different of bubbling temperatures with $Q = 2l/min$ and $z = 3cm$ (right)

.

We found on fig.2.25 that the water content increases strongly with times for a hight bubbling temperature. Note that, when $W \approx 16\%$, the granular medium is very humid. A packing of glass beads with a packing fraction of ≈ 0.60 is saturated at $W \approx 25\%$.

2.4.4 Courbe de calibration

The water content was not homogeneous in the packing at a high bubbling temperature. Thus, we worked at a weak temperature (just above room temperature) to avoid this problem. Then, the amount of water depended weakly on the sample height.

On fig.2.26 (left), we resume the protocol used to calibrate the water content obtained with injections times. The value of W was measured for different of test, and W depends on two parameters : the bubbling temperature T and the injections times t. In fig.2.26 (right), we show the calibration curve of the water content $W(\%)$ as a function of the injections time for different weak bubbling temperatures. Initially, there was a very small amount of water content $W(\%) = 0.05 \pm 0.02(\%)$ corresponding to the temperature and $RH\%$ in the room. This means that there was already a very small amount of water on the grains surface. Then, the amount of water increased very slowly as a function of injection times for three different bubbling temperatures.

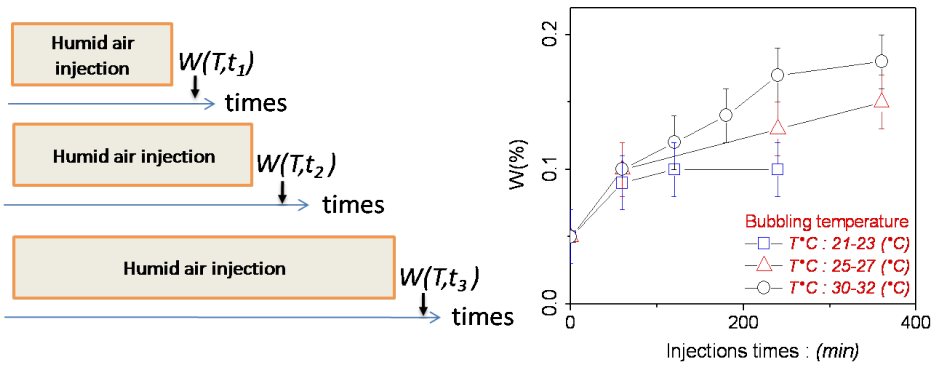

FIGURE 2.26: Calibration protocol (left) and amount of water content $W(\%)$ as a fonction of the injection times for different bubbling temperatures $T^{\circ}C$ (right)

For all our tests, we prepared the humid sample with a bubbling temperature at $30^{\circ}C$ to obtain an homogeneous sample with a low water content. We assume that the weak air flux does not perturb the system, we notice no evolution of the force when the flux is stopped. The main advantage of this method was that we can control the packing fraction and the water appeared evenly distributed with very weak temperature of bubbling ($\leq 30^{\circ}C$).

2.5 Pont capillaire

From previous measurements of Hornbacker et al. [18] on rough bead packing, the relationship between the roughness amplitude δ and the saturation bridge volume w_b is given by $w_b \approx 2R\delta^2$, where R is the mean bead radius. Remember (see chapter.1) that the "saturation bridge volume" is the water content where all the asperities are filled with water. Measurements with atomic force microscopy establish in their case, a roughness amplitude of 500 nm, hence a value $W_b = 0.07\%$. Our preparation method leads to a maximal water content of $W = 0.18\%$. We do not have a precise measurements of the roughness, however if we keep a number of the same magnitude, inspection of the curve (see fig.2.27) between the mean number of capillary bridges pergrain, N and water

content W, shows that it is likely that I prepares samples in the "pendular state" regime and in the rising part of the curve ($1 < N < 6$).

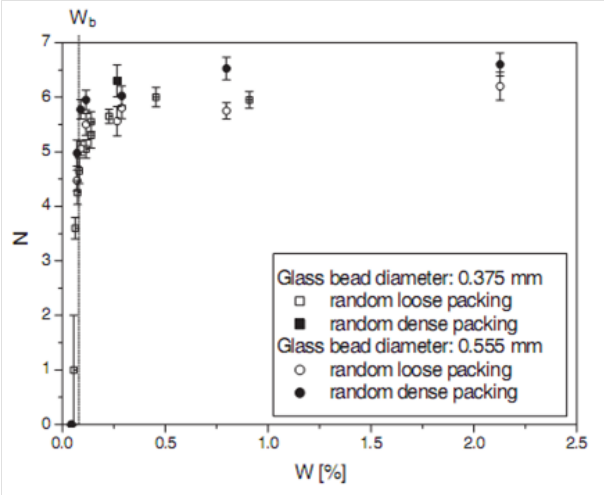

FIGURE 2.27: Average number of capillary bridges (N) per grain as a function of the water content W, taken from [95].

2.6 Conclusion

We presented the set-up and the different related calibration curves required to measure the shear stress and deformation. The packing fraction is well controlled with the system developed which uses a fluidization bed. To generate the vibration, we selected a method which uses a piezoelectric transducer producing two types of vibration : square and sinusoidal input tension, the roof mean square acceleration being controlled and calibrated for different voltages and frequency inputs. A set-up following to add a controlled amount of water in the granular medium was also established.

CHAPITRE 3

RÉPONSE ÉLASTIQUE ET FLUAGE D'UN MILIEU GRANULAIRE

Contents

3.1 Introduction

In this chapter, I present my results on the mechanical response of a dry granular medium, under shear stress in the absence of vibration. To this purpose, we use the vane shear cell described in the previous chapter (fig.3.1). Annular shear cell or Couette shear cells, similar to this apparatus are classical geometries used to study rheological properties of complex fluids. In the case of granular materials, it has been extensively used both experimentally [37, 50, 59, 92] and also in discrete particle simulations [60, 76, 73]. However, those studies were working essentially in a steady regime at constant rotation rate of the inner cylinder. Note that in this case, one observes generically a localization of the deformation in the vicinity of the rotating cylinder. The regime where I am working is closer to the standard quasi-static regime investigated in Soil mechanics usually explored by triaxial tests [31].

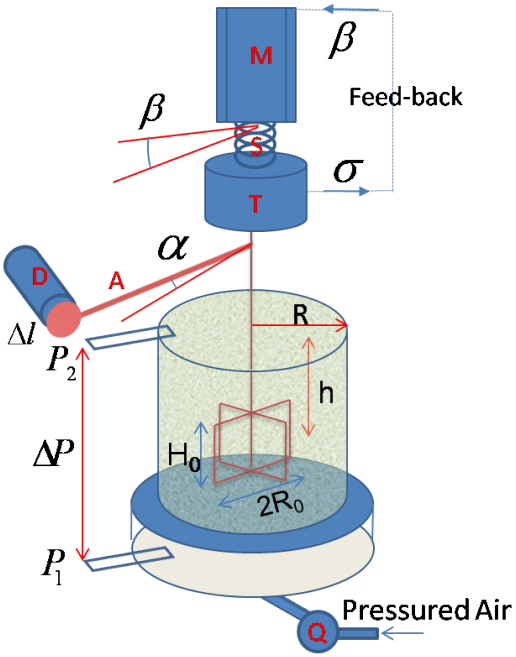

FIGURE 3.1: Schematics of the shear cell with all the parameters that we measure : α the rotation angle of the shear vane, β the rotation angle of the motor, σ the shear stress and ΔP the different pressure.

With this apparatus, I designed a method for measuring the elastic response of the granular medium and studied the evolution of the shear elastic modulus G as a function of the packing fraction ϕ. Furthermore, I studied the mechanical response on the granular medium under a ramp of shear stress to identify the yield stresses for different packing fractions. Then, I present a systematic exploration of the creep dynamics, as a function of applied shear stress and packing fraction.

The rheological results are analyzed using a conceptual framework developed earlier for complex fluids i.e. the fluidity parameter that represents a rate of stress relaxation [13]. On the basis of the experimental results, we determined the model parameters based on control parameters such

as packing fraction and shear stress.

Finally, I present an experimental analysis done in collaboration with a team at the University of Rennes. We implemented on the rheological set-up a diffusing wave spectroscopy (DWS) technique. Hence, we could map spatially the deformation field at the top surface of the packing. We studied in details the creep dynamics and identified localized plastic event ("'the hot-spots"') that we relate to the fluidity parameter evolution.

In this chapter, all the granular sample were prepared according to the method described in chapter 2. Note that we always worked under controlled air humidity ($RH = 35 \pm 5\%$). It is indeed known that this parameter may have a strong influence on the physical properties of a granular medium, particularly because of aging properties [29, 38]. We also worked in a room with a low background mechanical noise, we measured the residual background noise by placing an accelerometer in the packing and found the RMS acceleration to be of the order of $0.02 m/s^{-2}$. Note importantly that we place our shear vane probe in the bulk of the granular material but not to deep to as much a we could boundary effects as well as Janssen's effect. In most of the results, the depth of insertion is $h = 5cm$ (see fig.3.1), which is to be compared with the radius of the cell $R = 5cm$.

3.2 Réponse élastique

3.2.1 Méthode de mesure

Once the packing is prepared at a fixed compacity, we performed motor rotation cycles which led to oscillations of the applied shear stress. The resulting deformation was monitored in parallel (see on the fig.3.2). The oscillation frequency was chosen to be $1/12 Hz$. The frequency of stress and strain acquisition was $41 Hz$. All cycles were performed under a confining pressure corresponding to $P_0 = \rho\phi g h$ and under a mean shear stress $\sigma = 0$. The amplitude of the rotation were small enough such that resulting deformation was about 10^{-5}.

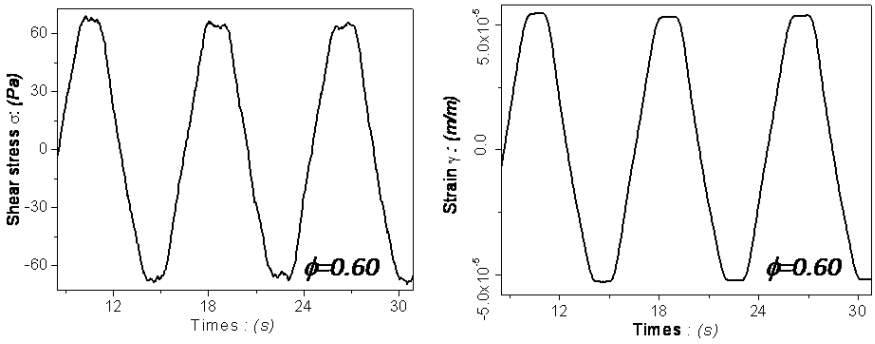

FIGURE 3.2: Elastic response recorded for a packing fraction $\phi = 0.60$. Response of the material submitted to a shear stress (left) and response of the material in shear strain (right).

We found that the value of the shear stress and the shear strain did not change after successive charges and discharges and the maximum and the minimum of shear stress and shear strains were

always symmetric around 0. On fig.3.3, I display the relation between the shear stress to the shear strain for different packing fractions : the lowest $\phi = 0.56$, $\phi = 0.60$ and the highest $\phi = 0.625$. Within the experimental accuracy, the cycles are closed and reversible which confirms that the response of the material is essentially elastic. We define the effective elastic modulus G as the slope of the dotted line in fig.3.3 (middle) :

$$G = \frac{\Delta\sigma}{\Delta\gamma} \tag{3.1}$$

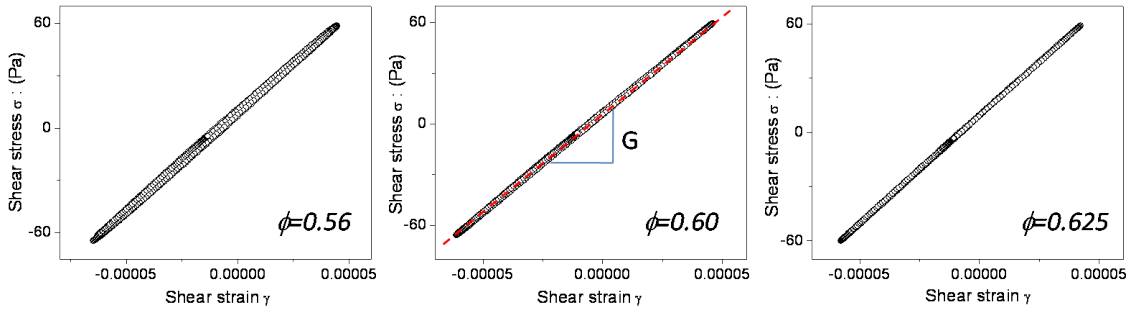

FIGURE 3.3: Relation between the shear stress and the shear strain for a packing fraction $\phi = 0.56$ (left), $\phi = 0.60$ (middle) and $\phi = 0.625$ (right), straight line $y = Gx$.

G is displayed on fig.3.4 as a function of ϕ. Interestingly, the relation seems linear $y = G_* x$, with a good accuracy.

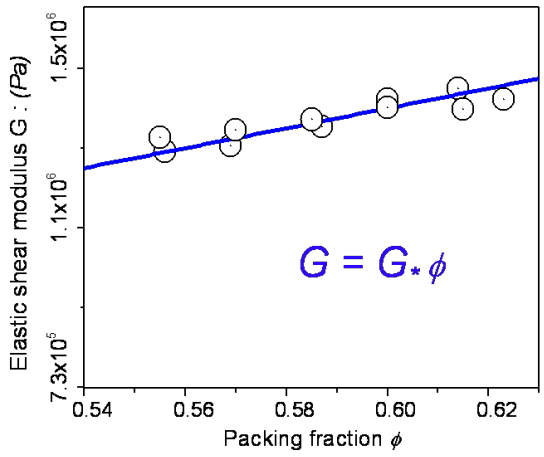

FIGURE 3.4: Shear modulus G as a function of the packing fraction ϕ under gravity confinement P_0, straight line $y = G_* x$ with $G_* = 2,28.10^6$Pa.

3.2.2 Discussion sur la rigidité de la pale

A question is to relate the effective elastic modulus G to granular material shear modulus G_{gra}. If the apparatus stiffness was infinite, both quantities would be the same. We provide here two esti-

mations of the apparatus rigidity, one is an upper value, the other is a lower bound. To estimate the upper value, I calculated theoretically the axis rigidity. The lower bound is obtained experimentally by measuring the stiffness of the whole shear vane in the absence of grain between the blades. Once an estimation of the effective angular stiffness of the apparatus C_{app} is provided, we can calculate the shear elastic modulus of the granular medium G_{gra} from the shear elastic measured G (the value of G is shown on fig.3.4).

Theoretical calculation of the axis rigidity.

We performed a simple theoretical estimation of the elastic compliance of a stainless steel rod of length L and diameter r, connected to the shear vane to the torque probe (fig.3.5). We have the rod shear stiffness (steel) $G_{steel} \approx 80GPa$. The rotation angle measured from the arm rotation α (eq.2.10) is the sum of two angles :

$$\alpha = \alpha_1 + \alpha_2 \tag{3.2}$$

where α_1 and α_2 are respectively the total rotation angle of the steel rod and the granular medium when a torque T is applied (fig.3.5). Here, we assume that the connection of the inside of the vane filled with the granular material is very stiff, this is why this value is an upper bound. We have a relationship between the shear elastic modulus measured G and the angle α :

$$T = G.2\pi R_0^2 H_0.\frac{R_0}{R-R_0}\alpha \tag{3.3}$$

where H_0 is the height of the shear vane, R_0 and R are the diameter of the shear vane and the sample, respectively (fig.3.5). The shear elastic modulus of material G_{gra} is such that :

$$T = G_{gra}.2\pi R_0^2 H_0.\frac{R_0}{R-R_0}\alpha_2 \tag{3.4}$$

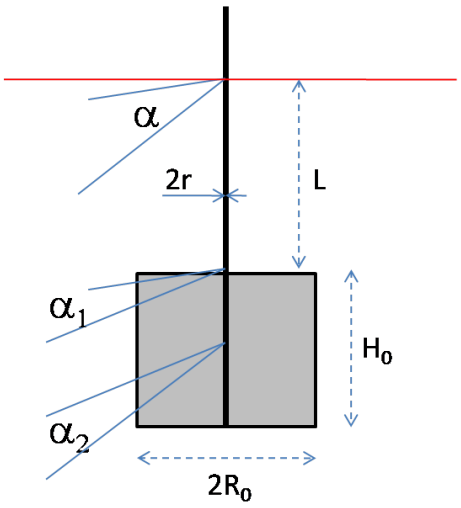

FIGURE 3.5: Schematic representation of the shear vane

The relation between the applied torque and the total relation angle α_1 is :

$$T = C_{app}.\alpha_1 = \frac{G_{steel}.\pi r^4}{2L}\alpha_1 \tag{3.5}$$

where C_{app} is the stiffness of steel rod. Then, we have :

$$\frac{\alpha_1}{\alpha} = \frac{G(\phi)}{G_{steel}}\frac{4LR_0^3H_0}{\pi r^4(R-R_0)} = 1,5.10^{-7}.G(\phi) \tag{3.6}$$

From the eq.3.3, eq.3.4 and eq.3.6, the shear elastic moduli of the granular medium G_{gra} is calculated from the value measured G by the following relation :

$$G_{gra} = \frac{\alpha}{\alpha_2}G(\phi) = (1-\frac{\alpha_1}{\alpha})^{-1}G(\phi) = \frac{G(\phi)}{1-1,5.10^{-7}.G(\phi)} \tag{3.7}$$

Experimental measurement of the vane rigidity.
To verify this theoretical results experimentally, fig.3.6 shows a experimental results for which two opposite blades were blocked rigidly and a torque equivalent to a shear stress $\sigma = 10^3 Pa$ was applied. Since this measurement is performed in the absence of granular material between the blades and also with two blades out of 4 blocked, this is a lower bound for actual stiffness.

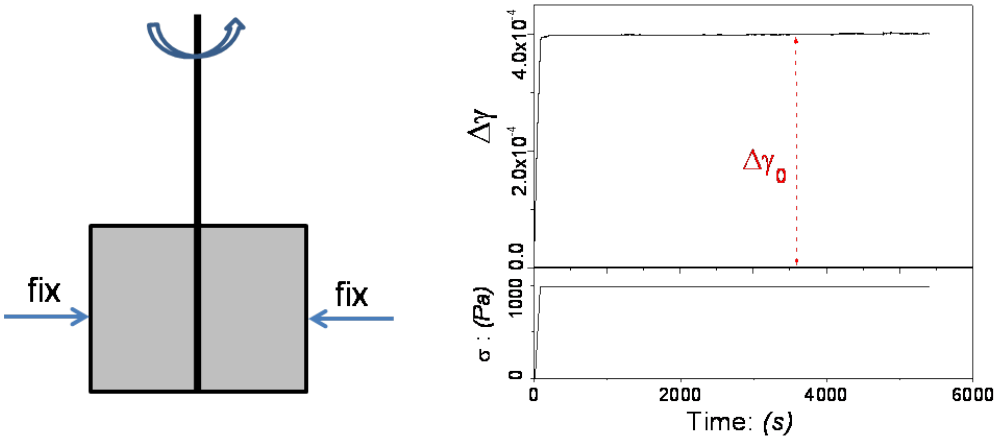

FIGURE 3.6: Shear vane was blocked (left) and a deformation during the shear vane blocked according to a $\sigma = 1000Pa$ (right).

The resulting deformation $\Delta\gamma$ was about $4,3.10^{-4}$, see fig.3.6(right). Then, the stiffness is :

$$C_{app} = \frac{2\pi R_0^3 H_0.\sigma}{\Delta\gamma.(R-R_0)} = 20,38(Nm/rad) \tag{3.8}$$

Thus, the granular sheat stiffness is :

$$G_{gra} = \frac{G(\phi)}{1-4,3.10^{-7}.G(\phi)} \tag{3.9}$$

On fig.3.7 the relationship between the granular shear elastic modulus and packing fraction is displayed for the three different cases : infinite stiffness, lower and high apparatus stiffnesses. Essentially, the results stays the same within the experimental uncertainties : the relation between shear stiffness and packing fraction is linear. The difference is in a prefactor of magnitude 2.5 at the maximum (same order of magnitude). In the rest of the study, I choose the lower bound apparatus experimental estimation to compute the granular shear moduli.

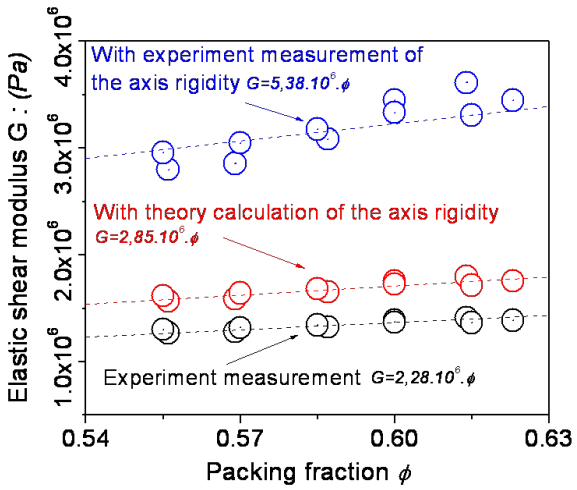

FIGURE 3.7: Relation between the shear elastic modulus G and the packing fraction ϕ, in three different cases : experimental measurement (black cycle), with theory calculation of the axis rigidity (red cycle) and with experiment measurement of the axis rigidity (blue cycle), dotted lines results from linear fitting.

3.2.3 Champ moyen de l'élasticité de Hertz

At the microscopic level there is a non-linear relation between force and displacement for two spheres in contact. This is the Hertz theory of contact [86]. For an assembly of elastic spheres under compression, theoretical calculations established a macroscopic relationships between shear and strain for a cubic [22] or random packing [93], this is the effective packing shear modulus. In all these cases, mean-field approximations (MFT) were made on the contact distribution. Essentially (within prefactor), all relations come out [43] as :

$$G_{gra} \propto G_0(\phi Z)^{2/3}\left(\frac{P_0}{G_0}\right)^{1/3} \tag{3.10}$$

where Z is the mean contact number, G_0 is the material Young's modulus and P_0 is the confining pressure. Following the framework of the (MFT), one can see that the macroscopic value of the elastic modulus mainly reflects two contributions for the packing fraction. First, a density of contacts proportional to ϕ which gives a contribution as G_{gra} in $\phi^{2/3}$. Second, for gravity confinement, a confining pressure term also proportional to ϕ which yields a $\phi^{1/3}$ contribution to the shear modulus. Overall, both contributions would predict, in our case, a linear variation of shear modulus with packing fraction , which was found experimentally (see fig.3.7). In other words, within our experimental accuracy, we could not identify anomalous stiffness properties as expected

in the limit when the mean number of contacts approaches the jamming threshold, i.e. when the packing is about to loose its stiffness rigidity (see [88] and refs inside).

3.3 Réponse à une rampe de contrainte de cisaillement

Here, I describe my results about the response of the granular packing to a shear stress ramp. The applied shear stress is changed by rotating at constant rate the motor which drives the torsion spring. We concentrate our study on the characterization of the material resistance i.e. we determine the maximal stress that the packing can hold before yielding of reorganizing. In the this study, we vary some important control parameters, essentially the packing fraction, but also the motor rotation speed, the spring stiffness and the insertion depth.

3.3.1 Résistance d'un empilement soumis à une vitesse de chargement constante

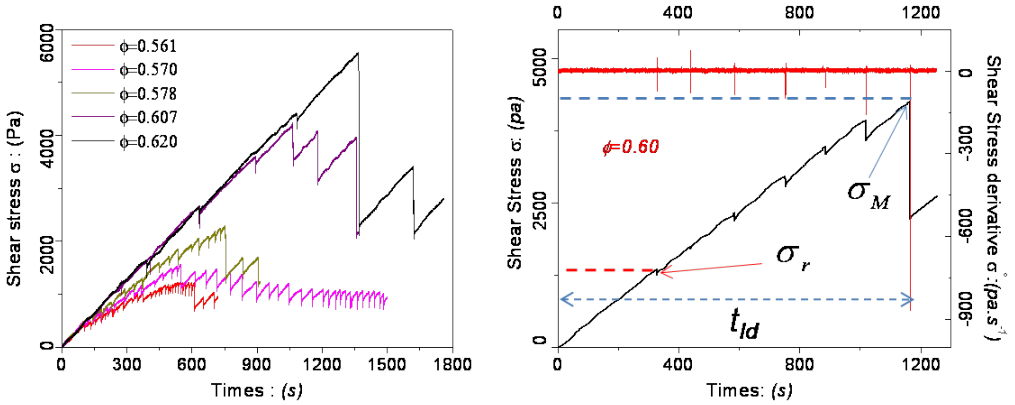

FIGURE 3.8: *Response to a stress ramp at* $\dot{\beta} = 0.00104 rd/s$ *and depth of shear vane* $h = 5cm$. Shear stress as a function of time for different packing fractions (left) and shear stress σ as a function of time at packing fraction $\phi = 0.60$, the first rupture stress σ_r and maximum stress σ_M are displayed as horizontal dotted lines, t_{ld} is called *loading time* ; Top : shear stress derivative as a function of time (right).

Shear stress ramps were applied at a constant and a slow driving velocity ($\dot{\beta} = 0.00104 rd/s$) using the softest spring constant available ($k = 2,45.10^{-3} Nm/rd$). On fig.3.8 (left), we present the shear stress as a function of time for different values of packing fraction. First we see that for each packing fraction value the medium can only sustain a maximal stress value. The higher is the packing fraction, the higher is this value that we call σ_M (see fig.3.8 (right)). Second, we observe clearly the presence of shear stress drops before reaching the maximum, for all the values of packing fraction studied. Note that similar behavior was reported by Albert et al.[71], for the drag force on an intruder near jamming.

We observe that for a higher packing fraction ($\phi \geq 0.6$), shear stress increases almost linearly with time and once the maximum is reached its value decreases progressively to a steady limit. However, for lower packing fraction ($\phi \leq 0.6$), the curve seems to bend until it reaches the upper

value. This type of behavior is often described in classical soil mechanic tests and is related to so-called dilatancy effects. However in our case, we could always identify a stress maximum before the occurrence of the steady stick-slip regime. Furthermore, I measured the global packing fraction variation using the air fluidized technique described previously, but I could not detect any variation. Note that the density variation could well occur locally but are not sensitive to it. Now we focus on the small rupture events that seem to combine to give the overall shape of the response curve. Essentially, we are interested here in the first part of the response i.e. for stresses below the maximum value σ_M. On figure 3.8 (right), we display the stress response and the shear stress derivative as a function of time ($\phi = 0.60$). At first, a linear increase of the stress is observed with a slope corresponding essentially to the spring constant. Then, at a given stress level σ_r, we observe the emergence of a well marked and sudden granular material reorganization (see top view on fig.3.8 right). These events are very well marked as witnessed by the derivative curve. We define this stress value as the "first rupture stress" : σ_r. Then, we observed rather equidistant events corresponding to stress drops and large plastic deformations. The shear stress can still be increased up to a maximum value σ_M where the large stress jump is evidenced and a subsequent stick-slip dynamics is observed. For each packing fraction, I determined the number of rupture events N_r corresponding to the number of large shear stress jumps and the loading time t_{ld} corresponding to the required time to reach the maximum shear stress (fig.3.8 right). On fig.3.9 both quantities are plotted as a function of packing fraction. We observed that N_r decreases strongly with ϕ. The overall shape of the stress response curve is directly associated to the number of those rupture events. However from these data it is difficult to establish clearly if something specific happens at $\phi \approx 0.6$ often described as the dilatancy threshold [44].

From fig.3.9 (right), we see that the loading times increases almost linearly with the packing fraction and by linear interpolation, the value of t_{ld} reach 0 when $\phi = 0.525 \mp 0.05$, hence probing the essential fragility of the packing at low packing fraction. Note for comparison, that the compacity of a cubic packing of mono-disperse spheres is $\pi/6 \approx 0.523$.

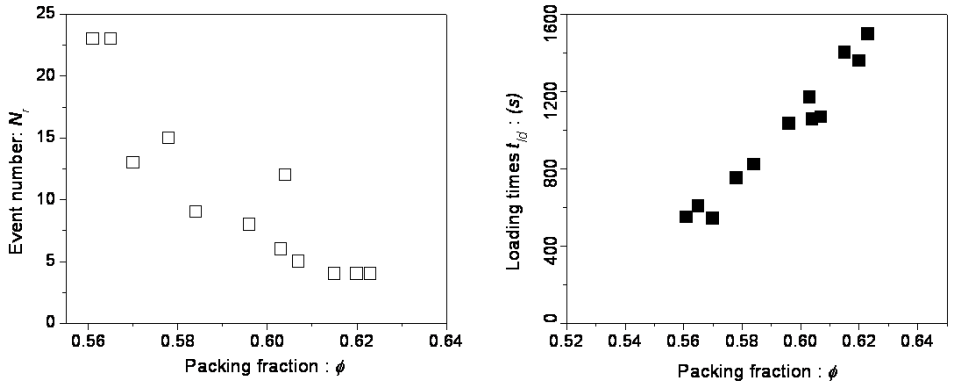

FIGURE 3.9: Event number as a function of the packing fraction (left) and loading time as a function of the packing fraction (right).

To observe clearly these stress drops, we plotted on fig3.10, the relationship between shear stress and shear strain for two values of packing fraction, at the level of the first yield σ_r. Prior to the main rupture corresponding to a significant deformation jump ($\gamma \approx 10^{-3}$), one observed a precursor plastic creep. This phenomenological behavior will become important later in section

3.5 when the deformation field is spatially resolved using Diffusion Wave Spectroscopy technique. Note that, the deformation 10^{-3} corresponds to a small blade displacement $\approx 40\mu m$ which is 1/5 of the mean diameter of the grains. The typical time-scale for these events to occurs is around 2 seconds, this value depending on our set-up rigidity.

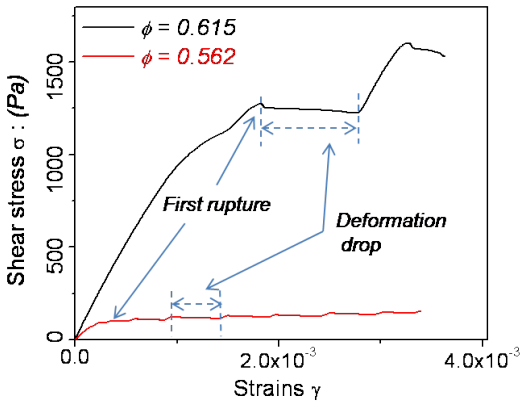

FIGURE 3.10: Response to a stress ramp at $\dot{\beta} = 0.00104 rd/s$. Shear stress as a function of deformation for two values of packing fraction $\phi = 0.615$ and $\phi = 0.562$.

On fig.3.11, the shear stresses corresponding to the first (σ_r) and the last rupture (σ_M) are displayed as a function of packing fraction for a fixed rotation rate $\dot{\beta} = 0.00104 rd/s$. Both values increase strongly with the packing fraction. Interestingly, these stress values (σ_r and σ_M) are strongly related since their ratio remains constant : $X = \sigma_M/\sigma_r = 3.5 \pm 0.2$ (see upper part of fig.3.11).

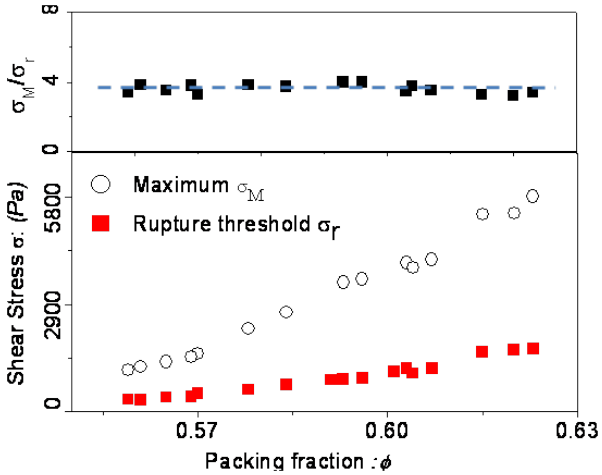

FIGURE 3.11: Response to a stress ramp for the same rotation rate, σ_r, σ_M and the ratio $\frac{\sigma_M}{\sigma_r}$ according to the packing fraction.

Note that these results can be put in perspective with other recent experimental results obtained by Metayer et al.[44], where the maximal stress needed for pulling a thin, rough, metal plate vertically in a granular column appeared to be a function of ϕ. The authors showed that the yield

stress increases exponentially with ϕ above 0.595 and claim the existence of a phase transition related to dilatancy. Though a dilatancy-like transition behavior can be observed for the shape of the response curve (see fig.3.8 left), we see no transition effect in the behavior of σ_M nor in σ_r. Furthermore, the actual values increases monotonously with packing fraction and does not vary of more than a factor 5 in the same range of density. This difference of behavior is not understood. However, since in this last reference, the probe is buried deep in the column, we point out that the presence of stiff boundaries may play a dominant role on the kinematic constraint (quasi fixed volume condition).

For a granular non-cohesive material the rupture stress is associated with a Coulomb-like threshold which means that its value of σ_M should be essentially proportional to the mean confining pressure P_0. On fig.3.12), I display results where the confining pressure P_0 is changed by varying the vertical position of the shear vane. In principle, the value of P_0 should change linearly with the mean depth h_m : $P_0 = \rho g \phi . h_m$. At larger depth a linear relation of the type $\sigma_M = \mu \rho g \phi (h_m - h_0)$, with $h_0 = 5mm$ is observed.

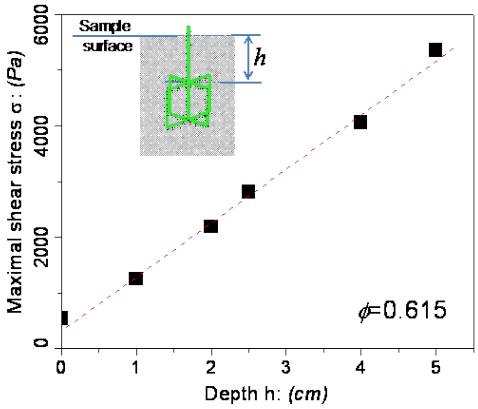

FIGURE 3.12: Maximum shear stress σ_M as a function of depth h with packing fraction $\phi = 0.615$, the drashed line is drawn as a guide to the eyes.

3.3.2 Influence de la vitesse chargement

So far, I presented results obtained at slow and fixed motor rotation rate of $\dot{\beta} = 0.00104 rd/s$. Now I explore the influence of the loading rate on the ramping response. At a fixed packing fraction, the motor rotation speed is varied and the corresponding value of σ_r and σ_M are displayed on fig.3.13(left) for $\phi = 0.6$. We observe that the maximum shear stress is decreased from a value corresponding roughly to $4000Pa$ down to 70% of this value at higher speed. Interestingly, the variation of yield stress with loading rate is observed for other complex fluids like Lennard Jones glasses [54] , polymer melts [58], however in general the variation is more an increase rather than a drecrease as recorded with our granular packing. Note that the partial ruptures events almost diseapear at high loading rate. On fig.3.13 (right), I displayed loading curves corresponding to 4 different compacity and clearly, the rupture events do not show up. So the rupture events, when they occur, seem to consolidate the granular material. This is a notion that we will recover in the next section when we explore the creeping properties under constant shear stress. The effect of maximum stress variations with the rotation rate, seems to occur at values of the order of $3.10^{-3} rd/s$

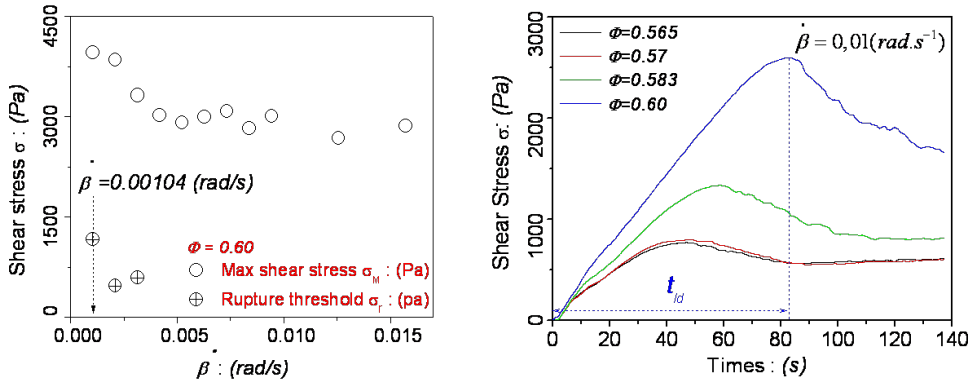

FIGURE 3.13: *The Coulomb yield.* Maximum shear stress σ_M and first shear stress σ_r according to the motor rotation rate $\dot{\beta}$ for a packing fraction $\phi = 0.60$ (left) and relation between the shear stress and the time for different packing fractions at a constant motor rate $\dot{\beta} = 0.01(rd/s)$ (right)

which would correspond to a shearing rates of $10^{-3}s^{-1}$. Indeed, the rupture event of typical magnitude $\Delta\gamma \approx 10^{-3}$ take place in out set-up on a time scale of the order of a second, which correspond to the right magnitude of shearing rate. So we expect that at lower $\dot{\beta}$ values σ_M and σ_r will not change much, this is why we choose the value $\dot{\beta} = 0.00104rd/s$ to perform the systematic study in the previous section.
Finally, we see that at high loading rate, the shear stress always reaches a maximum before decreasing and this, for all packing fractions explored. In the granular material literature, the presence of such a maximum is often associated to a dilatancy behavior. Here, it is surprising to observe such an effect persists at lower packing fraction (down to $\phi = 0.56$). It may mean that the dilatancy transition effect is not only geometrical but also, has a dynamical component. Fig3.13 (left) shows that the difference $\sigma_M - \sigma_r$ is about constant as long as these rupture events show up. This would still be true for very small rotation speed.

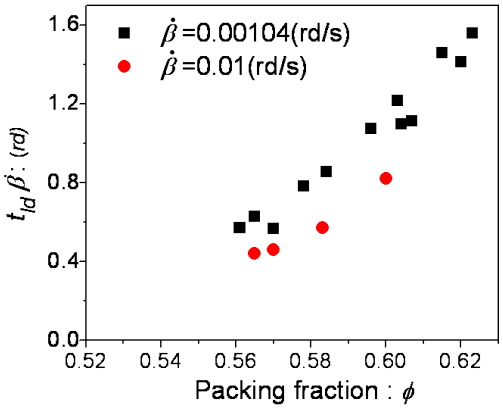

FIGURE 3.14: Rescaled loading times $t_{ld}\dot{\beta}$ as a function of the packing fraction for two different motor speeds : $\dot{\beta} = 0.00104(rd/s)$ (black) and $\dot{\beta} = 0.00104(rd/s)$ (red).

For all my measurements at different packing fractions and different rotation rates, I extracted the loading time t_{ld}, i.e. the time to reach the stress maximum σ_M. On fig.3.14, I display the rescaled loading time $t_{ld}\dot{\beta}$ as a function of packing fraction. The data points seems to rescale significantly on an increasing linear relation. However, there is also a clear tendency to observe a higher rescaled loading time at lower loading rates. This behavior indicates that the criterion which determines the onset of a major plastic yield would be that a critical deformation value $\gamma_c(\phi)$ of the granular packing is reached. The larger is ϕ the larger is $\gamma_c(\phi)$. Moreover, the actual value of $\gamma_c(\phi)$ seems to increase as much as 20% in the limit of low loading rate.

3.3.3 Influence de la raideur du ressort

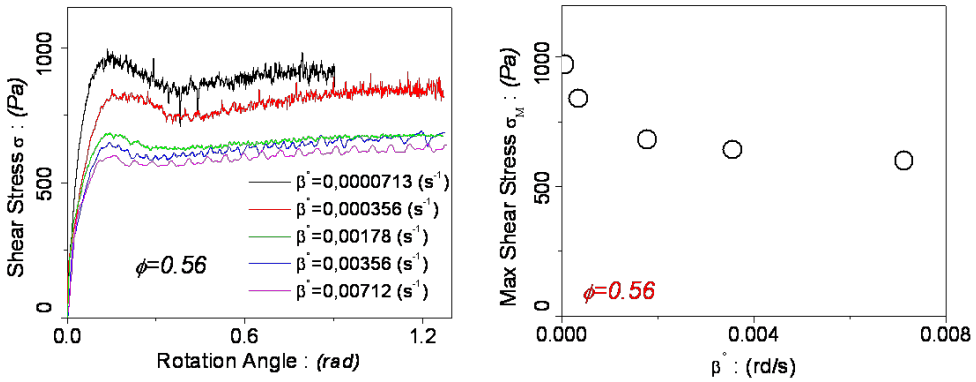

FIGURE 3.15: *Using the hardest spring*. Relation between the shear stress and the motor rotation (left)and maximum shear stress σ_M according to the motor rotation rate $\dot{\beta}$ for a packing fraction $\phi = 0.56$ (right).

In this section, we vary the apparatus stiffness. But by lack of time, we did not perform a full systematic variation of this parameter. We only present here results where we tried to get the stiffest system we could. To this purpose, we connected a rather thick plate in steel between the motor and the torque probe. The geometry of this steel rod junction of length $L_j = 5cm$ and rectangular cross section $(3mmx5mm)$ provides a rotation stiffness equivalent to the one of the steel rod composing the vane. Still by lack of time, I could not test systematically the ramp response of this configuration with the packing fraction. I only present here results for a loose packing at $\phi = 0.56$. On fig.3.13 (left), are displayed ramping curves for different $\dot{\beta}$. On the right part of this figure is displayed the maximum value as a function of the rotation rate. We see indeed that a decrease in σ_M with the rotation rate is recorded. However the loading time (t_{ld}) to reach the maximal stress is almost independent on the loading rate over two decades in $\dot{\beta}$. But in this case as discussed in section 3.2, the deformation inside the granular material is equivalent to the deformation of the apparatus shaft. Therefore, these results are consistent with the previous findings. The fact that t_{ld} is independent of $\dot{\beta}$ confirms the criterion for a major plastic yield based on deformation value $\Delta\gamma_c$ on the order of 10^{-2}. Note, however that we cannot observe clearly the first rupture corresponding to σ_r, because we do have the motor angular resolution (here $2\pi/10000$) to get a good precision on the deformation.

3.3.4 Influence de l'humidité relative

The influence of relative humidity RH on the rheology of a granular packing was analyzed in different studies [38, 36, 55]. Experimentally, Ovarlez et al.[38] showed that the resistance of a granular medium increases strongly with the relative humidity. On the other hand, dramatic influence of RH on the stability was studied by Restagno et al.[36, 55]. Their experiments showed that the cohesion force in a humid atmosphere was related to the dynamics of nano-size water bridges between the grains and surface asperities. I did some qualitative tests to estimate this dependence by flowing humidified air in the granular packing and measuring the relative humidity at the top of the packing. On fig.3.16, I present the evolution of σ_M as a function of the relative humidity RH. Variation as large as 30% in the value of σ_M was observed for packing fraction at $\phi = 0.60$ for humidity in the range $20\% < RH < 95\%$.

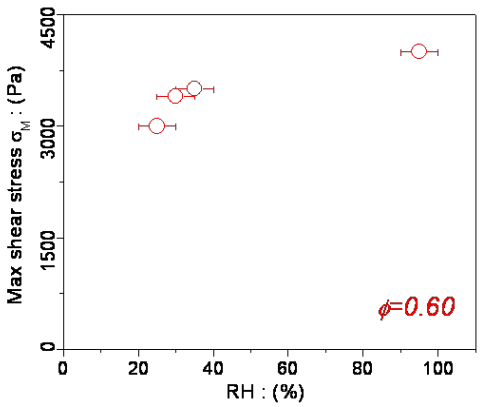

FIGURE 3.16: Maximum shear stress σ_M according to the relative humidity RH for a packing fraction $\phi = 0.56$.

This explains why in our study, we took special care to make experiments at a value $RH = 30 \pm 5\%$, which was a "natural" value of RH in the room during regular climatic conditions.

3.4 Réponse à un fluage

In this section, we explore systematically the creep question of a dry granular packing at a constant shear stress, in order to reveal and characterize the internal relaxation processes.

3.4.1 Feedback

To maintain a constant shear stress on the packing, a feedback procedure was programed on Labview. The key of this feedback loop is that the motor will rotate the torsion spring according to the signal provided by the torque probe such that its value is maintained within a given tolerance $\Delta\sigma$. The motor can rotate step by step at precision of $1/10000$ of a cycle. If stress goes beyond of below the allowed range, after about $0.1s$, a command is sent to the motor in order to rotate the torsion spring and adjust the torque within the appropriated range.

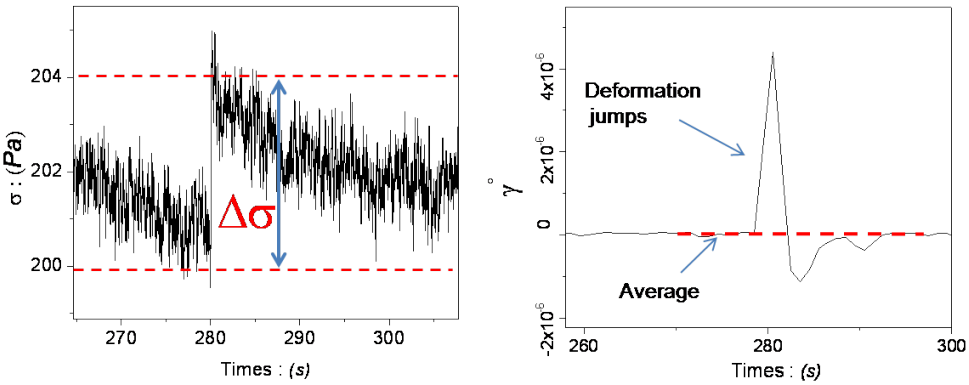

FIGURE 3.17: *Feedback response at a creep test* on the shear stress (left) and on the creep curve derivative (right)

.

On fig3.17 (left), we zoom a response of feedback on the shear stress. Due to the feedback mechanism, from time to time, the motor angle changes abruptly ($\Delta\beta = 6.410^{-}4rd$) to keep the shear stress in the specified domain ($\sigma + / - \Delta\sigma/2$).

However, when monitoring the deformation, one can see that a consequence of the sudden motor rotation is that the deformation rate displays a characteristic response which is a significant peak followed by a damped oscillation (see fig.3.17 right). We verified that after less than 20s the deformation rate always comes back to the value assumes before the sudden motor rotation. This happens from time to time, may be 3-5 times in a data sequence of 6000s or more. In the following, to compute the shear rate evolution, we filtered these artificial events. In practice, we simply replace the values corresponding to the fast rate variations (about 20 points i.e. 20s) by the average of the time series corresponding to one minute before the jump and one minute after the deformation rate has comes back to its original value.

3.4.2 Déformation par fluage

In this section, we present the creep deformation of the granular packing under a constant shear stress. We focus on the determination of the macroscopic creep dynamics when varying the applied shear stress and the packing fraction. From results of the stress ramp tests in previous section, we have determined the maximum shear stress σ_M corresponding to each packing fraction, which allows us to work in the stress range $0 < \sigma < 0.8\sigma_M$. Typically, the creep dynamics is monitored over long times (about 70000 seconds). The procedure consists in two steps : first a monotonic loading up to the desired shear stress value σ. This initial procedure is fast with respect to the creep dynamics (typically less than $200s$ at the slowest motor rotation velocity) (fig.3.18 left). Note that we verified *a posteriori* that the loading time scale is much smaller than the inverse of the observed initial shearing rate.

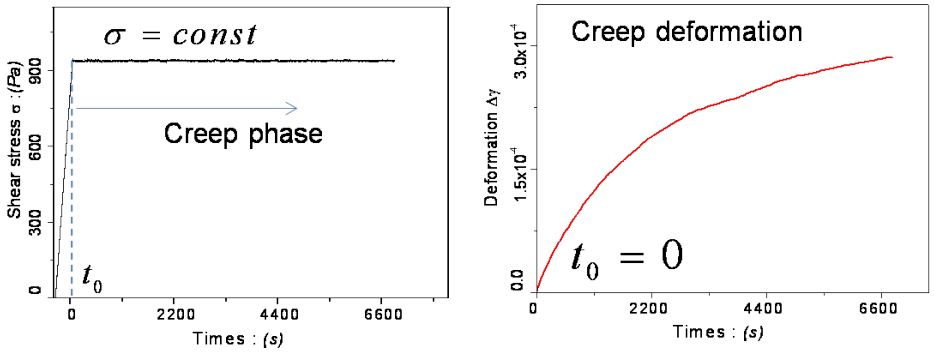

FIGURE 3.18: Creep test for packing fraction $\phi = 0.60$. Note the initial load phase lasting 200s, the creep phase where the shear stress is maintained at $\phi = 930 \pm 2(pa)$ (left) and the creep deformation $\Delta\gamma$ (right). The origin of times $t_0 = 0$ is taken at the beginning of the creep phase.

Then, the feedback mechanism is applied to control the stress value with a tolerance of $\pm 2Pa$ around the fixed stress σ. For all creep tests, $t_0 = 0$ is the time from which creep strains are measured (fig.3.18 left). We observe, for all experiments, a creep dynamics corresponding to a slow increase in the deformation $\gamma(t)$. With the same value of applied shear stress σ, we found logically that the creep deformation decreases with the packing fraction (see fig.3.19 a). The creep dynamics seems to increase with the value of σ (see fig. 3.19 b) these stress values smaller than the yield stress.

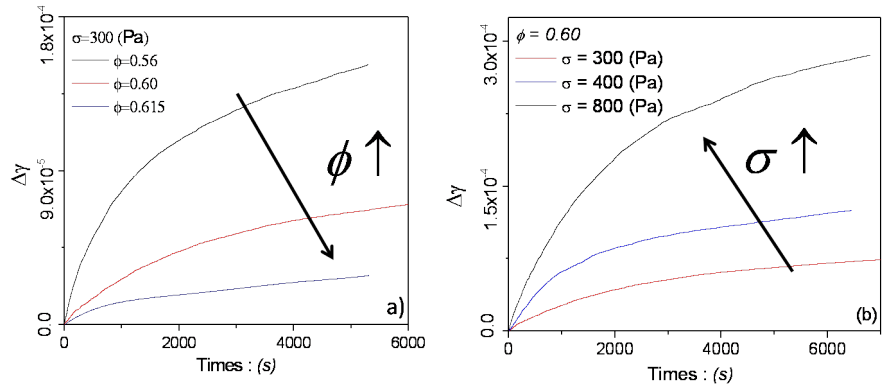

FIGURE 3.19: Creep deformation $\Delta\gamma$, under different packing fraction at shear stress $\sigma = 300Pa$ (a) and different shear stress as a packing fraction $\phi = 0.60$ (b).

3.4.3 Glissement aux parois extérieures

In the creep regime that we explore, it is important to be sure that what we are indeed measuring bulk properties and that the creep dynamics is not due to a significant slippage at the external cell wall. To confirm that it is not the case, we have filmed the outer surface of the packing for one hour in standard experimental conditions. We used a CCD camera to observe the grains horizontal

motion by zooming a point corresponding to a light reflection on a glass bead visible at the vertical wall of the cell.

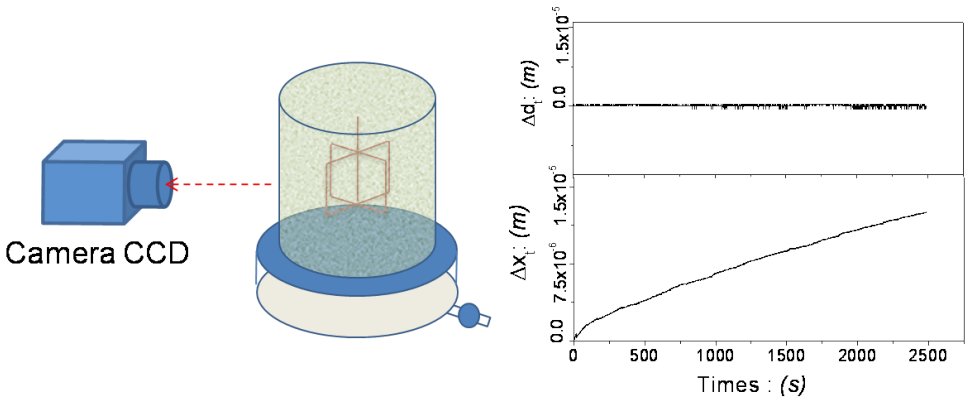

FIGURE 3.20: Experimental setup (right) and creep test at σ=1600Pa and at packing fraction ϕ = 0.60 ; 'Top' : slippage at the outer wall, 'Bottom' : rotation of the granular material (left)

We worked at a packing fraction $\phi = 0.60$ and a shear stress value of $1/2$ of the maximum shear stress is applied (see fig.3.20 (left)). Fig.3.20 (right) shows on the same scale the horizontal position of the grain (top) and the distance variation :

$$\Delta x(t) = \Delta\alpha(t).R \tag{3.11}$$

where $\Delta\alpha(t)$ is the rotation angle of the shear vane and R is the sample diameter. So $\Delta x(t)$ would corresponds to a solid displacement the grains and thus to the maximal slippage effect one can observe. We see indeed that $\Delta x(t)$ is much larger than $d(t)$ the grain displacement, indicating that the observed creep is essentially due to bulk deformations of the packing .

3.4.4 Déformation logarithmique par fluage

In all the tests we performed, we observed a long time creep deformation typically proportional to the logarithm of time. To determine quantitatively this dynamics, we first filtered the deformation rate jumps due to the motor feedback (see fig.3.17). Then, we determine the initial value of the shear rate $\dot{\gamma}_0$ by fitting a third order polynomial over the first 1000 s (see fig.3.21).

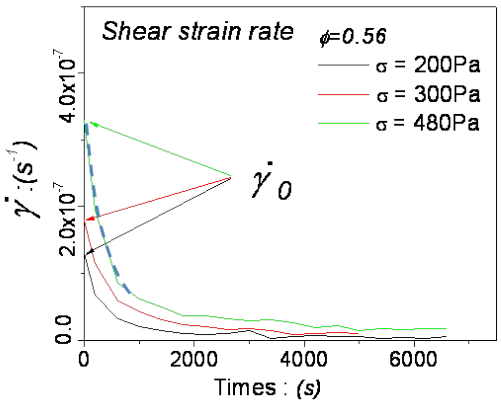

FIGURE 3.21: Different shear strain rates with different value of σ for creep tests with $\phi = 0.56$, dotted line is a third order polynomial fitting.

To establish the logarithmic creep, we computed $\dot{\gamma}^{-1} - \dot{\gamma}_0^{-1}$ as a function of time (see on fig.3.22). Here, we used an average of the shear rate over a time centered window of $\Delta T = 400s$. In all cases we obtain with good approximation, a linear relation passing through zero. Therefore, all the experimental curves were characterized using an empirical relation of the type :

$$\dot{\gamma}^{-1} - \dot{\gamma}_0^{-1} = Ct \tag{3.12}$$

with C being a constant determined by a linear fit. Thus it would correspond to a deformation creep law of the type :

$$\gamma = \gamma_0 + \frac{\dot{\gamma}_0}{C} \ln(1 + Ct) \tag{3.13}$$

which displays a long time logarithmic dynamics.

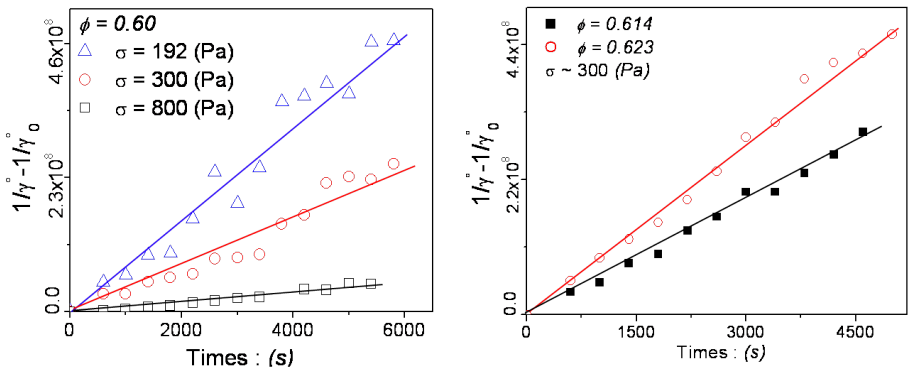

FIGURE 3.22: Plot of $\dot{\gamma}^{-1} - \dot{\gamma}_0^{-1}$ as a function of time for creep experiments, performed at a constant packing fraction $\phi = 0.6$ for different shear stresses (right), and at a constant shear stress with different packing fractions (right). The straight lines are linear fits : $y = Ct$.

The creep curves performed at different packing fractions and shear stress values, are then characterized by an initial shear rate $\dot{\gamma}_0(\sigma,\phi)$ and a creeping slope $C(\sigma,\phi)$. On fig.3.23, we display $\dot{\gamma}_0$ as a function of σ. We see a linear relation which slope seems to increase with packing fraction.

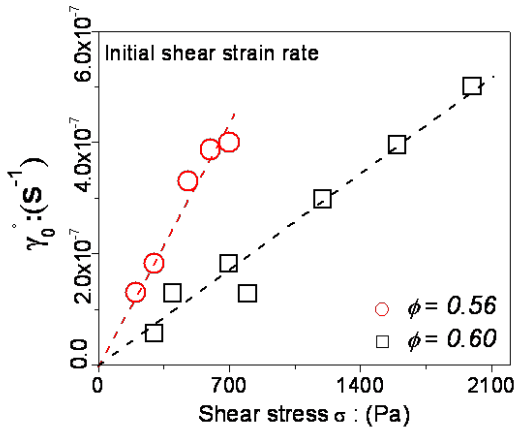

FIGURE 3.23: Initial shear strain rate as a function of the shear stress for two different packing fractions $\phi = 0.56$ and $\phi = 0.60$, the dotted lines are linear fits.

On fig.3.24, we display C as a function of σ for different packing fraction. We observe a non-monotonic decrease with σ, the value of C is large corresponded to a large creep deformation. The displays of non-monotonic behavior demonstrates the existence a value of σ which changes the creep properties for each packing fraction.

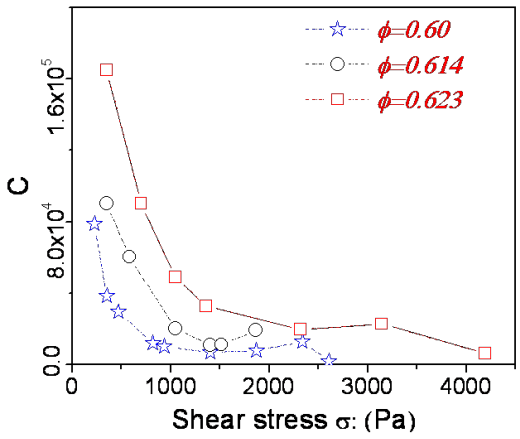

FIGURE 3.24: Values of C with a function of σ for three values of packing fraction.

3.4.5 Vibrations résiduelles

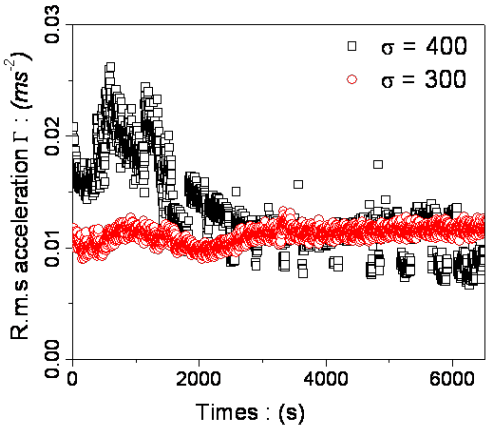

FIGURE 3.25: R.m.s acceleration measurements as a function of time during a creep experiment at $\sigma = 300Pa$ and $\sigma = 400Pa$.

As we will see in the next chapter, the mechanical vibrations have a strong influence on the creep dynamics. Therefore, even for the experiments performed in a "quiet room" condition, I estimated the mechanical background noise. To this purpose, I measured the r.m.s acceleration Γ in a granular medium by placing in the packing an accelerometer. The acquisition rate is $10^4 Hz$ and the average was done over $1s$. Measurements done without the motor yielded a value $\Gamma = 0.02 \pm 0.01 m/s^2$. I also display on fig.3.25 the values of the RMS acceleration Γ during a creep experiment as a function of time for $\phi = 0.60$ under various applied stress. Our results show that the presence of the motor hardly changes the background noise value, at least in the limit of our measurements capacities. Note that we do not know precisely which part of this small residual noise is physical or is due to electronic noise.

3.4.6 Modèle théorique de fluidité

Experimental results of creep test allow us to study the internal dynamical processes taking place in a granular packing below the yield stress. To analyze quantitatively the data, we used a theoretical model proposed by Derec et al.[13] in the context of complex fluids rheology. We propose here to adapt it to the creep flow of a granular packing.
This model introduces an internal phenomenological variable called "fluidity" f whose physical interpretation is simple as it represents a time dependent rate of stress relaxation. It extends naturally the standard Maxwell visco-elastic rheology. The second (and central) issue is to provide a constitutive relation for the dynamique of $f(t)$. Since the original theoretical propositions of 'Soft Glassy Rheology' [79] or 'Shear Transformation Zone' [35], various models have tried to capture the complex dynamics of energy reorganization taking place in amorphous solids or yield-stress fluids. These models can be quite sophisticated as their describe at a microscopic level, fluctuation processes which macroscopic emergence can be seen as the material "fluidity". In this thesis I will pursue a much simpler path along the lines originally discussed by Derec et al.[13]. In this case, the fluidity dynamics would results from the combined influence of aging and stress rejuvenation

processes. The set of coupled dynamical equations is :

$$\partial_t \sigma = -f\sigma + G\dot{\gamma} \tag{3.14}$$
$$\partial_t f = -af^2 + r\dot{\gamma}^2 \tag{3.15}$$

with G the constant elastic modulus, σ the applied shear stress, $\dot{\gamma}$ the shear strain rate, and a parameter a which is the aging parameter and r the shear rate induced rejuvenation parameter ; a and r are dimensionless positive parameters. The first equation is the visco-elastic relation. When $f = 0$, we have an elastic relation as described in section 3.2, when $G = 0$ and f is a constant, the stress response is that of a simple Newtonian fluid. The second equation is a phenomenological equation for fluidity. Note that the steady-state solution of this model ($\partial_t \sigma = 0$ and $\partial_t f = 0$) correspond to a rate independent dynamical shear stress : $\sigma_D = G\sqrt{a/r}$. We will focus our study on the case of a constant shear stress relaxation i.e. $\dot{\sigma} = 0$. Thus, in this case, one obtains the relation $f\sigma = G\dot{\gamma}$ and then :

$$\partial_t f = -a(1 - (\frac{\sigma}{\sigma_D})^2)f^2 \tag{3.16}$$

The fluidity algebraically decreases towards zero as : $f \propto 1/t$: there is no other time scale than the time lapse since the application of the shear stress (the system age).

Equivalent aging parameter

Introducing an equivalent aging parameter :

$$a_{eq} = a(1 - (\frac{\sigma}{\sigma_D})^2) \tag{3.17}$$

the solution of equation 3.16 is then :

$$f(t) = \frac{f_0}{1 + a_{eq} t f} \tag{3.18}$$

The shear rate variation is :

$$\frac{1}{\dot{\gamma}} - \frac{1}{\dot{\gamma}_0} = \frac{G}{\sigma} a_{eq}.t \tag{3.19}$$

This relation leads to a long time logarithmic creep as observed experimentally. Moreover, the experimental slopes C on fig. (3.24b) can be identified using the relation :

$$a_{eq} = C.\frac{\sigma}{G} \tag{3.20}$$

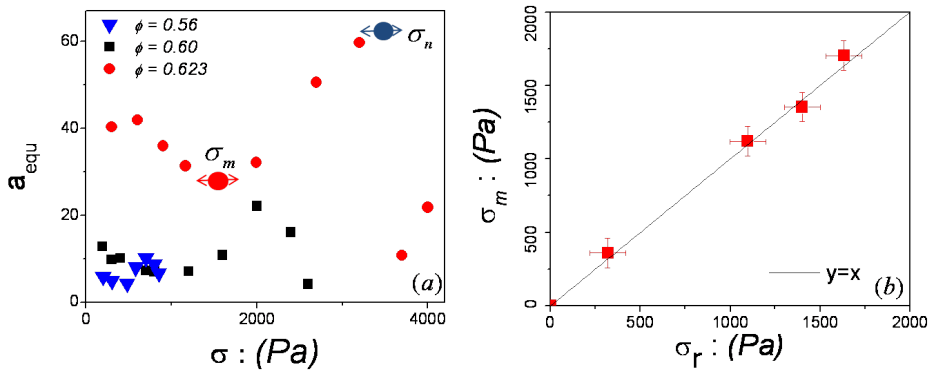

FIGURE 3.26: Effective aging parameter a_{eq} as a function of shear stress for different values of packing fraction (left). Comparison between σ_m and σ_r (right), straight line : $y = x$.

Analysis of the experimental results, based on the empirical determination of $C(\sigma,\phi)$ and $G(\phi)$ show that the equivalent aging parameter a_{eq}, depends strongly on the shear stress and the packing fraction. We point out here two important limits : when a_{eq} increases toward infinity, the material becomes purely elastic solid. On the other way, when a_{eq} decreases toward 0, the material becomes a fluid. For all packing fractions, a_{eq} displays a non monotonic behavior as a function of σ with a minimum value σ_m and a maximum value σ_n and reaches zero at a value $\sigma_D(\phi)$. These results indicate a dynamical hardening taking place when $\sigma_m < \sigma < \sigma_n$ (fig.3.4.6 left). In other words, the granular material seems to strengthen as its creep dynamics is slow down. For each packing fraction, I display on fig.3.4.6 (right), the values of σ_m as a function of σ_r, the "first rupture" stress measured, at various packing fractions, in the previous sub-chapter during the stress ramp test. The striking results if that both values seem to be the same : the onset of creep hardening σ_m can be identified with the first rupture process σ_r corresponding to reorganizations in the granular packing.

Initial fluidity

The concept of initial fluidity was also found to be very useful and we believe that it is the first time it has been used in the context of granular matter. It allows an interpretation of the linear relation found in section.3.2, where at different packing fractions, a linear relation between the initial shear rate $\dot{\gamma}_0$ and applied σ stress was found. Then we can compute the initial fluidity parameter :

$$f_0 = \frac{G(\phi)\dot{\gamma}_0}{\sigma} \tag{3.21}$$

Here, we calculate the value of f_0 considering that G is constant and independent of σ. The linear relation between σ and $\dot{\gamma}$, can be interpreted a Newtonian viscous relation where $\eta = G/f_0$ would be an effective viscosity and f_0^{-1} an internal material time scale. On fig.(3.27) the initial fluidity is displayed as a function of packing fraction, for all the values of stress studied. Interestingly, all data seem to collapse onto a linear curve ; the denser is the packing, the lesser is the initial fluidity. The linear extrapolation of this curve to $f_0 = 0$ yields a value $\phi_0 = 0.635 \pm 0.002$, close to random close packing of mono-disperse spheres. This can be interpreted as a stopping value for the creep dynamics corresponding to the jamming limit for ϕ in the case of a random assembly of frictionless

spheres [82]. The effective "'initial viscosity", then defined as :

$$\eta_0 = \frac{G(\phi)}{f_0(\phi)} \tag{3.22}$$

diverges when approaching the jamming threshold from below : $\eta_0 \propto (\phi_0 - \phi)^{-1}$. Indeed, in principle, we are below any thermalized regime where the viscosity concept could apply, this result is quite remarkable.

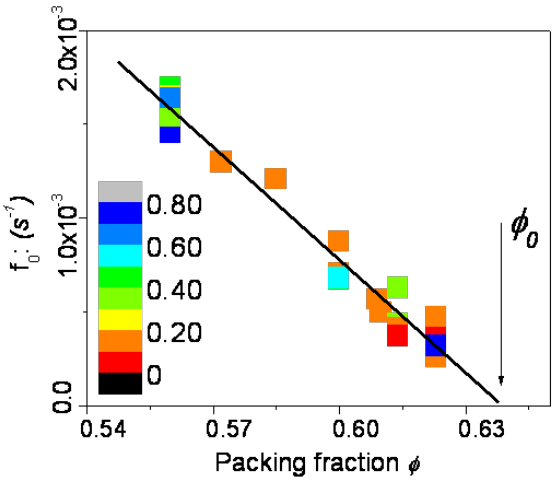

FIGURE 3.27: Initial fluidity f_0 as a function of the packing fraction for different shear stresses. The color index reflects the ratio σ/σ_M. The straight line is a linear fit $y = F(\phi_0 - \phi)$ with $F = 0.0086 \pm 4.7E-4$ and $\phi_0 = 0.635 \pm 0.002$.

Rescaling of the creep dynamic

Furthermore, the aging dynamics can be characterized by computing the equivalent aging parameter a_{eq} according to relation (3.20). If a and r are independent of the shear stress, a_{eq} should decrease quadratically and reach a zero value at a finite stress corresponding to the dynamical stress σ_D according to relation 3.17. However, the experimental results display a non-monotoneous relation between a_{eq} and σ, where σ_r, seems to be the onset of a "re-hardenning" process. On the other hand, the short-time dynamics of the creeping process reveals an internal time scale f_0^{-1}. This is why I propose, to characterize the aging properties of the packing, to represent a rescaled aging parameter $Y = f_0 a_{eq}$ as a function of the adimensionalized stress $X = \sigma/\sigma_r$ (see fig.(3.28)). The striking feature is that all data, at different packing fractions, collapse onto a single curve for the whole range of stresses and packing fractions studied. For values above $X \approx 2$, the creep dynamics increases again before reaching the dynamical stress threshold ($a_{eq} = 0$) at $\sigma_D \approx 2.4\sigma_r$. This means that in the steady regime, the shear stress is constant at $\sigma = 2.4\sigma_r \approx 0.7\sigma_M$. This result is consistent with the value of shear stress determined from shear stress ramp test at steady regime, an example is given for $\phi = 0.57$ (see on the fig.3.8). For smaller values of shear stress, i.e. below σ_r, the predictions of Derec's model (see relation (3.17)) can still be validated with a dynamical stress $\sigma_D = 1.5\sigma_r$ (see dashed line on fig. (3.28)). However, from a

phenomenological point of view there is clearly an effect missing and it would be interesting to see in further developments of the fluidity theories how such a behavior may be accounted for by extra terms in the fluidity equation. By extrapolation, it appears that aging is still present in the limit of zero applied shear stress. This may point out to the role of thermal activity or background mechanical noise in the phenomenology.

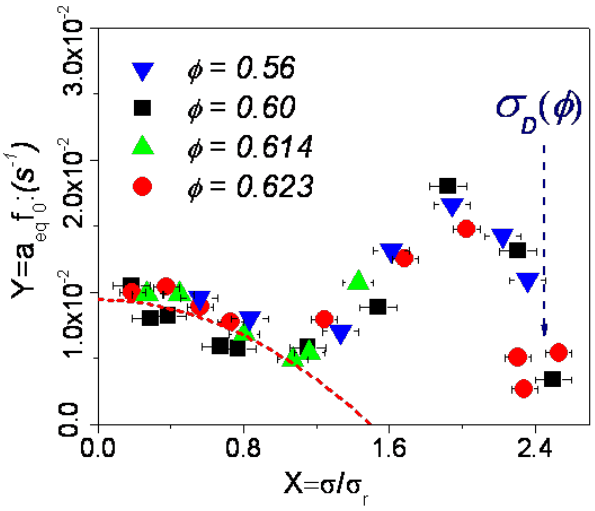

FIGURE 3.28: Rescaled aging parameter $a_{eq}f_0$ as a function of rescaled of shear stress $\frac{\sigma}{\sigma_r}$ for different packing fractions, dotted line is : $y = \frac{1}{t_*}\left(1-(\frac{x}{1.5})^2\right)$ with $t_* \cong 106s$.

Interestingly, on the basis of a linear relation between f_0 and the packing fraction, and using eq.3.19, we can propose the shear strain rate dynamics under the following form :

$$\dot{\gamma}(t) \propto \frac{\sigma}{G(\phi)} \frac{(\phi_0 - \phi)}{1 + \Phi(\frac{\sigma}{\sigma_D(\phi)})t} \tag{3.23}$$

Where $\phi_0 \approx \phi_{RCP}$ and $\Phi(X)$ is a function representing the nonmonoteneous behavior of the aging process which takes the value $\Phi(1) = 0$

Finally, this extensive study of creep test shows that down to vanishing low applied shear and up to the yield stress value, internal relaxation processes are present in a granular packing. The logarithmic creep hence evidenced was analyzed under the scope of a simple visco-elastic model introducing a time dependent rate of relaxation (the fluidity). The dynamics can be viewed as a competition between intrinsic aging and stress rejuvenation. The model allows a dynamical characterization of the initial packing fluidity which is shown to decrease linearly with the packing fraction and vanish at the random close packing limit. However, under finite stress, we identified the onset of major internal reorganizations, slowing down the creep process and setting the yield stress to higher values. This process could be related to the onset of stress induced anisotropy [27, 48] or shear band formation. The internal dynamical processes present in the granular packing are the sign of a peculiar fragility for this type of solid, possibly mediated by thermal activation or by background mechanical noise. However, it may also be intrinsically related to the

nature of elastic instabilities leading to the plastic response in amorphous solids [30]. Indeed, the inherent fragility of granular matter under shear presented in this work has strong similarities with creep properties evidenced in a large class of yield stress fluids [12]. Presently, there are few propositions on how, in an amorphous solid, plastic events can be triggered and organized by thermal or mechanical energy [87] and more generally, how under finite shear, a solid may flow [34] or break [70].

3.5 Spectroscopie par diffusion multipe de la lumière (DWS)

This section describes the results coming from a collaboration with Axelle AMON and Jérôme CRASSOUS at the *Institut de Physique* in Rennes to exploit the capabilities of our shear vane system and their knowledge in diffusing-wave spectroscopy (DWS) applied to granular matter.

It is well known that assessing experimentally the stress and strain fields in the bulk of a granular material is quite a challenging issue. This is why, numerous experiments were designed in 2D where in some case, a determination of the local fields was made possible. Otherwise, one has to rely on discrete particle numerical simulations where the full information can be obtained. However, the results may depend on the exact choice of granular interactions and was also limited to the computational power in terms of number of particles and computer time available. This restriction is particularly crucial in our case where creep deformations effects take place over long times and the question of the real impact of the detailled microscopic interactions is still unclarified. This is why, there is a need to back the macroscopic measurements of the previous section by a vision of the strain spatial distribution. Recently, the group of Rennes has shown that using the DWS backscattering technique, one could get a spatially resolved deformation map at the outer edge of a granular packing. Thus, to obtain a quantitative vision of the actual strain spatial distribution, we combined the mechanical tests with sample observation by back scattering DWS. Details on this technique and tests on various diffusive materials including granular packing can be found in [63]. In the present thesis, we only recall the general principles and the main results as applied to granular matter. Experiments were done at the ESPCI with Axel Amon and Jérôme Crassous group but the analysis of the speckle patterns was performed in Rennes using the softwares they developped.

3.5.1 Mesures locales de déformation

When a highly diffusing material, such as a packing of small glass beads is illuminated with coherent light, photons undergo scattering and propagate inside the sample, following different optical paths. The coherent light waves have different phases and interfere locally. As a consequence, the backscattered light shows a random interference pattern called a "*speckle*" pattern. If the sample is deformed, the optical paths inside the packing are modified and the resulting phases at a given place in space is changed. As a consequence a different speckle pattern is observed. Analyzing the correlations between speckle patterns recorded for different deformations of the sample gives information about spatial distribution of the strain field [63]. This makes the technique quite sensitive to very small deformations. The spatial resolution of the technique is defined by the typical spatial extension of an optical path travelling inside the sample. This extension is characterized by the so-called transport mean free path of the light, l^* which depends on the optical properties of the material. Typically, for a granular sample made of glass beads, $l^* \approx 3$ beads diameters [17]. In

this work, we will essentially present analysis of the results obtained from the speckle images post-processing done the by the Rennes group. Correlations between speckle sub-images is performed and meta-pixel images are created where logarithm reflects the deformation field between two moments where the speckle pattern was recorded [64, 63]. More precisely, the intensity correlation function between two images 1 and 2 is :

$$g_I(1,2) = \frac{\langle I_1 I_2 \rangle - \langle I_1 \rangle \langle I_2 \rangle}{\sqrt{\langle I_1^2 \rangle - \langle I_1 \rangle^2} \sqrt{\langle I_2^2 \rangle - \langle I_2 \rangle^2}} \tag{3.24}$$

here I_1 and I_2 represent the intensities at a given pixel in images 1 and 2 as illustrated on fig.3.29, $\langle . \rangle$ designates an average over all the pixels in the microscopic zone.

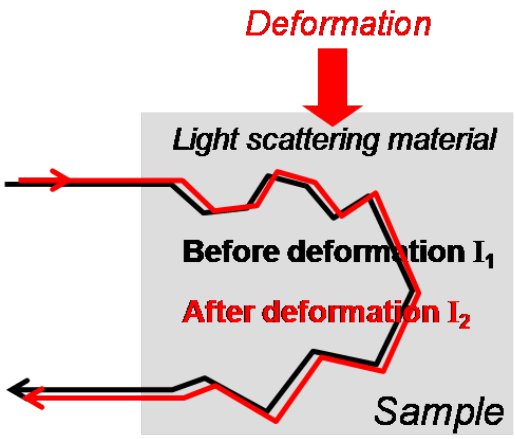

FIGURE 3.29: Illustration of the intensity before and after deformation

For a general deformation field, the theoretical modeling of light rays interference assuming the motion of random scattering centers, shows that the correlator $g_I(1,2)$ and the local values of deformation are related by a relation of the type :

$$g_I(1,2) \simeq \exp(-C\bar{\varepsilon}) \tag{3.25}$$

where $C \approx 6.9\sqrt{2\pi l^*/\lambda} \approx 1.5 \cdot 10^3$ is a numerical constant related to the ratio between the transport mean free path $l^* \approx 3.3d$ and λ the optical wavelength [64] ; $\bar{\varepsilon}$ represents a mean squared deformation which is an average of invariant elements of the deformation tensor ε.

3.5.2 Dispositif expérimental

The experimental setup is shown in fig.3.31. It combines the shear vane cell (see Chapter.2) and the DWS back-scattering method. For all theses theses experiments, the vane is introduced at a depth $h \approx 0$ (see fig.3.31) with the protocole described before. Experiments with two upper boundary conditions were done : free surface and loaded surface. To load the surface, we placed a circular piece of glass on the surface. Its diameter being identical with the sample diameter and a hole was drilled at its center to let the vane rod going through. Above the glass, we put weights to reach a vertical pressure corresponding to $P \approx 830Pa$, i.e. a load similar to the granular static pressure of the previous experiments. To avoid friction between the blade vane and the glass, we

introduced the blade at a depth $h \approx 2mm$ (fig.3.30)

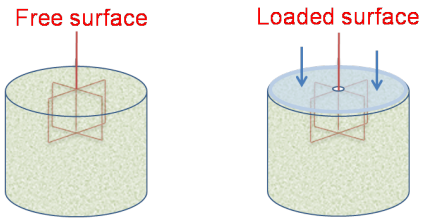

FIGURE 3.30: Free surface (left) and loaded surface with a desired load P (right).

To illuminate the sample, we used a Ventus continous-wave linearly polarized laser of wavelength $\lambda = 633nm$ and maximum power $\approx 50mW$. About a quarter of the top surface was illuminates (processed surface S=13cm^2). The scattered light was collected using an optical setup described elsewhere [63]. The top surface was imaged with a lens on a camera operating at a frame rate of 1 Hz. This camera was a DALSA PT-41-04M60 with a 2352×1728 resolution with a 7.4μm pixel size. An iris diaphragm allows to control the size of the coherence areas on the camera and a polarizer was introduced to enhance the speckle pattern contrast. All the signals were acquired at the same time to synchronize the values of stress σ, deformation γ and the speckle images. Two types of tests were performed : the packing response to a stress ramp and creep tests at a packing fraction $\phi = 0.60$. No vibration was applied and dry grains were used. To comply with the symmetry of the problem, the values of the intensity correlations are calculated from the average along a quarter of the circle at a distance r to the center : $\bar{g}_I(r) = \langle g_I(r,\theta) \rangle_\theta$.

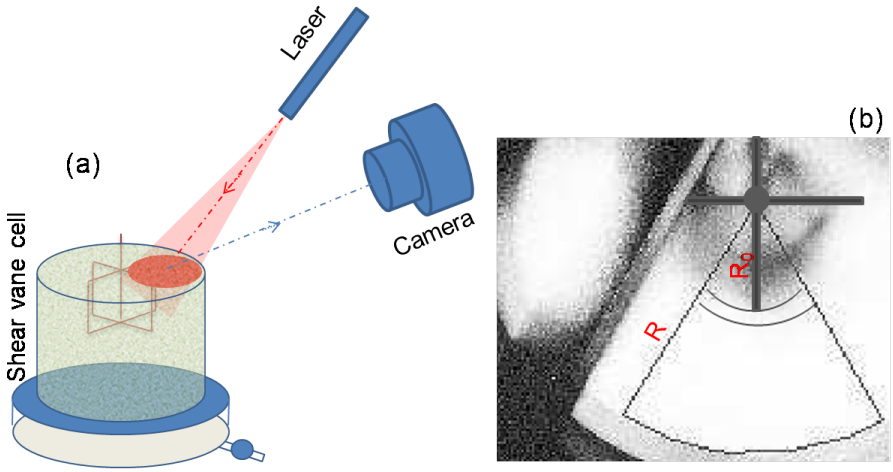

FIGURE 3.31: Shear vane cell and a schematic description of the diffusing-wave spectroscopy (DWS) method, which consist in illuminating the surface of the cell by a laser and collecting the image reflected by the granular speckle with a camera (a). Schematics of how the shear vane is inserted below the surface. The observation area is limited to a quarter of a circle and taken between the radius of the vane R_0 and the radius of sample R (b) .

3.5.3 Réponse à une rampe de contrainte

We first monitor the mechanical behavior of the granular medium submitted to a shear stress ramp obtained by rotating the torsion spring at constant rate. The radial variation of shear stress allows to explore the relation between the shear stress and the deformation. Then, we monitor the relation between the stress value and the dynamics of the correlation maps which reflects the spatial heterogeneity of the deformation distribution. In particular, we focus on the scenario when approaching the first rupture stress.

Stress ramp

A shear stress ramp is applied on the unloaded sample prepared at $\phi = 0.60$. The ramp is done at a constant motor velocity $\dot{\beta} = 0.00104 rd/s$. The speckle pattern is recorded every $1s$. Post-processing of the speckle dynamics allows to extract a relationship between the shear stress and the deformation at the surface observed for two subsequent images. On fig.3.32 , the macroscopic shear stress is plotted as a function of time. Below this figure the radial disribution of the correlator (averaged over 1/4 of a circle) $\bar{g}_I(r)$ is plotted. The gray code is such that $g_I = 1$ is white and low correlations are in black, which corresponds to important deformations. We can observe clearly on shear stress-time curve and on the radial correlation map, the effect of the 'first rupture' and subsequent series of partial ruptures.

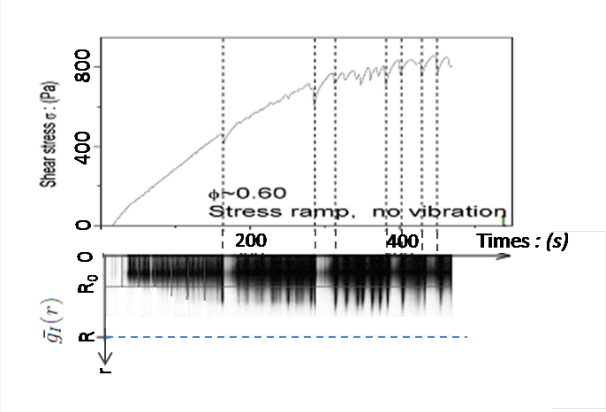

FIGURE 3.32: *Response to a stress ramp on the sample surface.* Shear stress as a function of times for a packing fraction $\phi = 0.60$ and $\dot{\beta} = 0.00052 rd/s$ with the juxtaposing of $\bar{g}_I(r)$

Hot spots

The most triking feature observed on the correlation maps is the presence of localized features corresponding to important localized deformations. For correlations between two images taken at a time lag of $\delta t = 1s$, the intensity correlation stays at $g_I = 0.99$ except over small areas, the hot spots, where a significant localized correlation drop down to $g_I = 0.95$ is observed. The extent of these spots is typically $3mm$, i.e. about 15 grain sizes. Fig.3.33 shows the correlation of a typical event and the distribution of the events size.

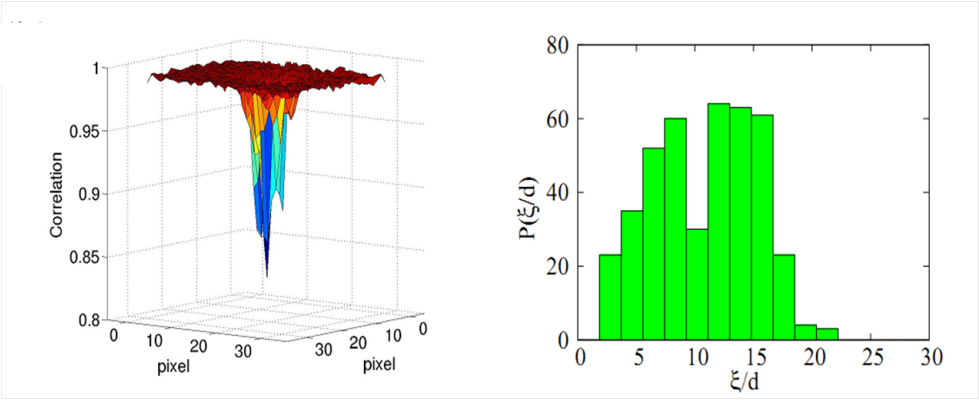

FIGURE 3.33: 3D representation of a typical event (left) and distribution of the event size ξ in units of beads diameter d in a creep test at shear stress $\sigma = 1200Pa$ for the loaded surface.

First rupture scenario

In this subsection, we focus our observations of the approach of the first rupture identified previously at a value σ_r, an example of the first rupture is presented on fig.3.34.

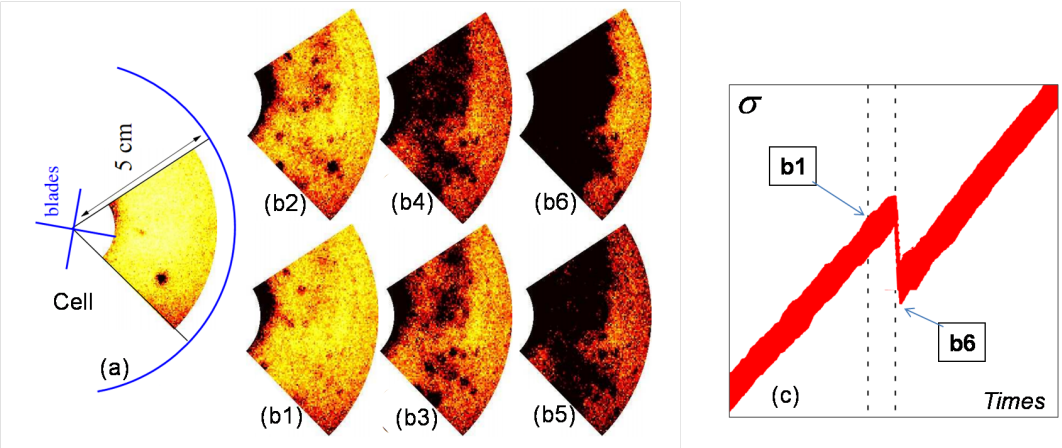

FIGURE 3.34: (a) Part of the surface of the cell that is used for the correlation maps showing a typical localized spot : typically, in average $g_I \simeq 0.99$ (yellow) and $g_I \sim 0.95$ for the black spot. (b1) to (b6) Correlation maps between successive images corresponding to the first stress drop. (c) Zooming of shear stress as a function of shear strain when the first rupture appeared.

Figures 3.34.(b1) to (b6) show successive maps corresponding to the vicinity of the first rupture stress σ_r. As the deformation is increased, more and more decorrelation events appear as described on fig. 3.34.) with the images (b1) to (b3). These events aggregate at a radial position fig. 3.34.(b3) and (b4). Finally, a large and totally uncorrelated zone appears at the place where the spots had previously aggregated (fig. 3.34.(b6)). This large decorrelation zone, corresponds to a shear band and is associated to the stress drop identified previously at the first rupture stress value (see on fig.3.34 (c)). Thus, our results seem to indicate the existence of a precursor scenario, here the "hot-spots" density increases in a region where a large rupture will occur. After that, the

frequency of hot spots events resumes at a lower pace until a new similar scenario is reached for the next large amplitude stress drop.

3.5.4 Déformation par fluage

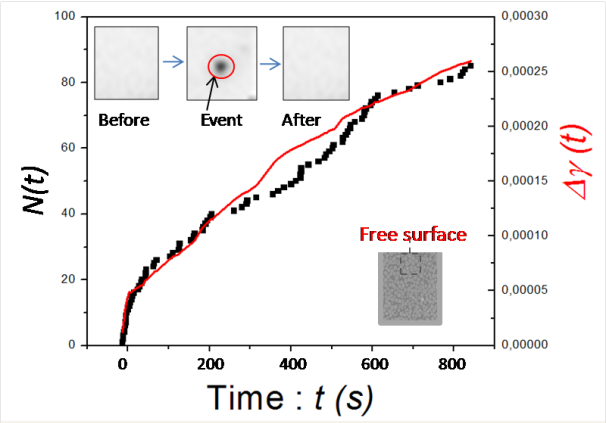

FIGURE 3.35: Creep deformation and accumulation of events as a function of time for a packing fraction $\phi = 0.60$ at shear stress $\sigma = 250Pa$ for the free surface. Inset : sample surface when an event appears (before-event-after).

In order to clarify the link between these localized zone and the plastic deformation of the material, we performed stress controlled creep experiments. In parallel with the creep deformation measurement, the "'hot spots"' dynamics was monitored. In the present report, experiments were performed for free and loaded surfaces (fig.3.30). We only focused on shear stresses of moderate amplitude, i.e. on values smaller than the corresponding σ_r. After processing the correlation maps, the spot location was identified by image analysis. Then, the cumulated number of localized events $N(t)$ was counted from the time $t = 0$ corresponding to the moment of application of the constant shear stress.

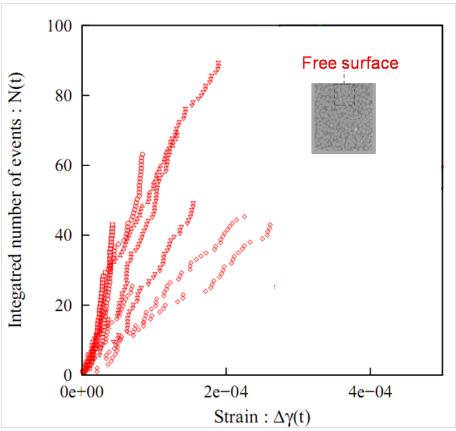

FIGURE 3.36: Integrated number of events in a free surface experiment for different applied stresses : 50 Pa (□), 100 Pa (∘), 150 Pa (△), 200 Pa (▽) and 250 Pa (◊).

On fig.3.35 the deformation $\Delta\gamma(t)$ (in red) and the cumulated number of events $N(t)$ (in black) are represented on the same graph. Their evolution seems to be strongly associated and in the following, we are going to relate explicitly the rate of apparition of the "hot spots" event to the global plastic deformation.

For a free surface loading condition, we display on fig.3.36, the relation between the cumulated number of events $N(t)$ and the creep deformation $\Delta\gamma(t)$. We see that the relation is roughly linear and that the slope decreases with the amplitude of the applied stress. The analysis that we propose is carried in the framework of the simple visco-elastic model presented in section 3.4. By integrating eq.3.15 from the origin of time to a time t after creeping at constant σ, one obtains :

$$\Delta\gamma = \frac{\sigma}{G}\int_{t_0}^{t} f(t')dt' \tag{3.26}$$

From fig.3.35, we found that the fluidity f was identified with the localized event.

$$\Delta\gamma = \frac{\sigma}{G}\int_{t_0}^{t} f(t')dt' \propto \frac{\sigma}{G}N(t) \tag{3.27}$$

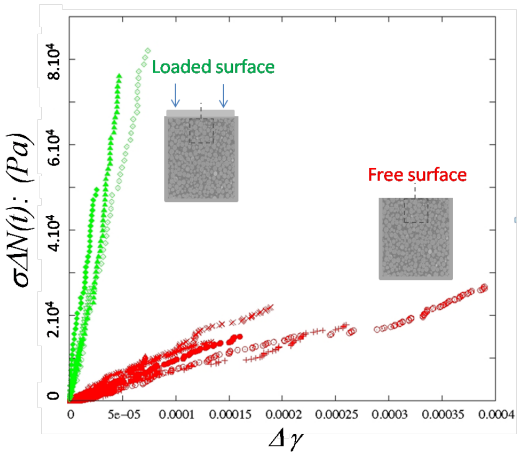

FIGURE 3.37: $\sigma\Delta N$ as a function of the creep deformation for a packing fraction $\phi = 0.60$ and different shear stresses. Measured in two cases : free surface (red) and loaded surface (green).

Fig.3.37 shows the relationship between $\sigma\Delta N$ and the creep deformation $\Delta\gamma$ for two types of test : free and loaded surface. With each type of test and for all the shear stress studied, all the data collapse onto a single curve. The slop on fig.3.37 is proportional to the shear modulus G. Due to Hertz elasticity, the effective shear modulus G should increase with the confining pressure P. The creep experiment results display the same quasi-linear relation between $N(t)\sigma$ and $\Delta\gamma(t)$ and also the expected qualitative stiffening (a factor 20 approximatively) (fig.3.37). However, from a simple account of the Hertz-law, we should only expect here a factor 5. This significant difference is possibly due to the presence near the free surface of a strong stiffness gradient and a diverging elastic susceptibility but we have no real explanation for the quantitative discrepancy. We directly measured the elastic response of the loaded packing and found $G = 1,6.10^6 Pa$. Our torque probe was not sensitive enough to access to the elastic regime of the free surface packing.

3.5.5 Dissipation d'énergie

The simultaneous monitoring of macroscopic mechanics response and local visulatisation using DWS technique, established a direct relation between the rate of creep deformation and the apparition of mesoscopic events. The fact that the event do cluster in the vicinity of major yield events *prior* to their macroscopic apparition, reinforces the idea that they play a leading role in the plasticity process. However, it is not a priori obvious that these are the only and sufficient modes of rupture to account for the full plastic flow dynamics. Therefore, we propose a simple model to estimate the energy released by the events in order to compare it with the elastic energy release in the bulk which could be at at the origin of the macroscopic irreversible deformations. The energy dissipation of one plastic event per unit of depth is $\sigma\varepsilon\xi^2$, where σ is the local stress, $\varepsilon = \sigma/G$ the typical plastic deformation during one event and $\xi = 3mm$ the typical in-plane extension of such an event. During creep experiment, the density of energy release through the elastic bulk relaxation processes is $\sigma\Delta\gamma(t)$. Therefore, for $N(t)$ hot spots visualized during the creep process, one can write an energy balance per unit depth, between the localized plastic dissipation and the bulk elastic relaxation. One obtains :

$$S\sigma\Delta\gamma(t) = \sigma\varepsilon\xi^2 N(t) \tag{3.28}$$

which yields a linear relation :

$$\sigma N(t) = K\Delta\gamma(t) \tag{3.29}$$

with $K = GS/\xi^2$ which is same type with what we found experimentally. Quantitatively, the relation can be tested on the loaded surface. We obtain $K = 10^9$ which is very close to the value obtained in fig.3.37. Therefore, within the consistency of the model, it seems that the energy released by the hot-spots is of an appropriate magnitude to account for macroscopic plasticity.

3.6 Conclusion

In this chapter, we presented systematically all the results recorded in the case of dry grains without vibration. The influence of the packing fraction on the elastic response, shear stress and creep dynamic were hence evidenced. We analyzed quantitatively the creep deformation with a fluidity model developed by Derec et al.[13]. Thanks to this model, we evidenced the significant parameter 'initial fluidity f_0' which depends only on packing fraction. Interestingly, the creep deformation and response to a stress ramp was consistent with the deformation measured by Diffusing-Wave Spectroscopy system. Then, we provided a direct visualization of the localized deformation events associated with the mechanical response of a granular packing under shear.

CHAPITRE 4

INFUENCE DES VIBRATIONS SUR LA RÉPONSE ÉLASTIQUE ET LE FLUAGE DYNAMIQUE

Contents

4.1 Introduction

The behavior of a granular medium under vibration is quite complex and displays a rich phenomenology. It has been the subject of numerous experimental and theoretical studies. Under weak vibrations, the flow properties can be strongly changed. For example, several works were devoted to the influence of vibrations driven by a piezoelectric transducer [9, 1] which inject sound waves in the material and modify its rheological properties. Also, the existence of a shear zone was found to modify the rheological properties at large distances, even in a zone where the granular medium did not display obvious agitation [47, 49]. In this chapter, I study the effect of vibrations produced by a piezoelectric device inserted in the granular medium in the context of the three mechanical tests presented in the previous chapter. In all cases, the granular packing is prepared by using the protocol defined previously for dry packing without vibration (see chapter.3). However, by lack of time I did not vary systematically the packing fraction and present essentially results obtained at $\phi = 0.6$.

In this study, a central control parameter will be the r.m.s acceleration measured using an accelerometer inserted in the packing at a given position. I will study its influence on the Coulomb yield threshold, the elastic response and the creep dynamics. I also studied spectral distribution of vibrations and its influence on the mechanical tests by varying the shape on the input electric signal. I do not have a systematic exploration of all these parameters, however as a first tentative, I will compare the results obtained for two different driving condition, i.e. square input at $100Hz$ and sinusoidal input at $1000Hz$ which display a different spectral response. The idea is to verify if the RMS acceleration is at least in first approximation, a pertinent control parameter. The spectral distribution of accelerations in the bulk and the relation between between RMS acceleration and input voltage was given in chapter 2 (see fig.2.14, fig.2.16, fig.2.19 and fig.2.20).

Note that for sono-fluidization at larger amplitude (typically $\Gamma \approx 0.35g$), Caballero et al. [72] have shown that the packing may undergo a slow logarithmic compaction. The total packing fraction after ten days had decreased by 3%. With a much stronger vibration $\Gamma \approx 6.8g$, Nowak et al. [24] found that this variation was about 5%. Thus, with vibration of typical maximal amplitude $0.04g$, we can assume that the packing fraction is not changed for application time of about 2 hours maximum.

4.2 Mesure du module élastique

4.2.1 Influence des vibrations

Propagation of sound waves in a granular medium is a classical technique which enables to measure the elastic modulii of a granular packing [7, 31, 23, 51]. In soils mechanics, the 'sound velocity' and 'small cycle of shear stress-shear strain' methods (as described in Chapter.3) were shown to be highly correlated [23, 31, 32]. In most cases, a very weak vibration was used and elastic response was found to be independent of the sound amplitude. However, some measurements were made recently at larger amplitudes and indeed a weakening of the modulus was reported. Effects of sound induced memories were invoked to explain the spatial coupling between tectonic shear zones and earth quakes triggering [46]. One of the simple questions to be asked in this section is how the low frequency shear elastic response is modified by the mechanical vibrations produced by the piezoelectric transducers. Fig.4.1 shows the effect of vibration on the normalized shear elas-

tic modulus $G/G_0(\phi)$ measured by a oscillation applied deformation (at 1/12 Hz). The method is presented in Chapter.2. The vibration is applied at the same time than the low frequency deformations and the overall measurements lasts 1 minute maximum. G_0 and G are respectively the values of shear elastic modulus with vibration and without vibration. Here, I present results obtained with a square vibration at $100Hz$ for three different packing fractions and a sinusoidal vibration at $1000Hz$ at $\phi = 0.60$. The data show that the elastic modulus is almost unchanged under very weak vibration $\Gamma < \Gamma_* = 0.08ms^{-2}$. So indded there might be a well defined elastic limit at low level of vibration. Note that the measured vibration level in the room was $\Gamma \approx 0.02ms^{-2}$. The second striking feature is that, even for different vibration conditions, the RMS acceleration seems a good control parameter as it regroups all the data on the same curve. However these results as they are, do not constitute an absolute proof and a more systematic work varying independently the driving amplitudes and frequencies is still to be done. The elastic modulus decreases quasi linearly with Γ. I fitted a function : $y = 1-(x-\Gamma*)b$, with $b \approx 1.5/g$. Note that with the sinusoidal tension input when $V > 6V$, the vibration spectrum begins to change drastically from quasi-harmonic to strongly anharmonic (see chapter.2, fig.2.16), but G continues to decrease linearly with Γ.

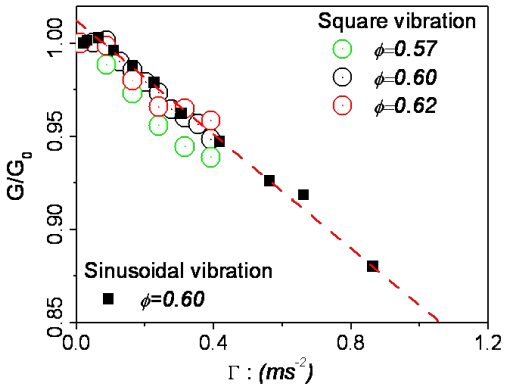

FIGURE 4.1: *Influence of vibration on the shear elastic modulus.* Normalized shear elastic modulus G/G_0 as a function of vibration level Γ for the sinusoidal and square vibration applied, fit line : $y = 1-(x-a)b$ with $a = 0.08$ and $b = 1.5/g$.

4.2.2 Réversibilité

This is an important issue in seismology to know, how a granular packing goes back (or not) to its initial structure when a vibration like a sound wave goes across a gouge zone (essentially composed of shared granular material). Experimental studies in the lab with shear apparatus by Paul et al.[68] and also field measurements of earthquakes synchronization have claimed that vibration could lead to a memory effects lasting a significant time. I established in the previous section that under vibration, the value of the shear elastic modulus is decreased significantly. A question is to know whether this material weakening is reversible and contains some temporal memory of the wave application. I established a protocol were after 1 minute of vibration and elastic response test, the vibration is suppressed. I continued to measure the shear modulus value. In fig.4.2 (left), I show the result for three different vibration levels. I found that the value of G was restored almost instantaneously (within few tenth of seconds) and was almost reversible. We can see that it can

go back 99% (fig.4.2) of its value. So no clear memory effect was detected and the action of weak vibration on the shear modulus under no applied shear stress, is quasi-reversible.

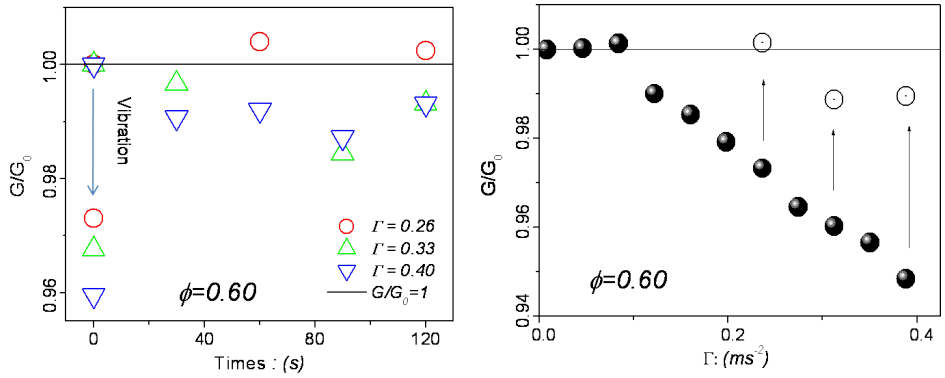

FIGURE 4.2: *Reversibility of a granular medium by measuring the shear elastic modulus G*. Evolution of G/G_0 as a function of the pause time, the black line is drawn as a guide to the eyes, $G/G_0 = 1$ (left), evolution of G/G_0 as a function of Γ after two minutes of pause (right).

4.3 Réponse à une rampe de contrainte

In the presence of vibrations, I performed stress ramp tests at fixed motor rotation speed $\dot{\beta} = 0.00104(rd/s)$. The maximum shear stress was measured. The vibration was introduced from the beginning of the ramp. In this section, we actually performed experiments for a systematic variation of compaction obtained with the same protocol as described in Chapter.3. The vibration level was also varied.

Remember that in the case with no vibration, we identified clearly a stress of first rupture σ_r. However in the same conditions with sufficient vibration, these events disappear as described on fig.4.3. In the case described in this figure, the vibrations were driven by a square tension at $f = 100Hz$ and $\Gamma = 0.4m/s^2$. The shear stress increases smoothly as a function of time until the maximum shear stress σ_M is reached. After that, the shear stress decreases smoothly and a quasi-steady regime is established. On the top of fig.4.3, we display the stress time derivative ($= 1s$) and besides noise, one does not observe the characteristic peaks as in fig. 3.8 with no noise. This curve is not perfectly horizontal, which allow us to consider that the shear-stress increases in a non-linear way with time. The displacement of the shear vane in then significantly larger that the grain size. Typically 50 grain sizes for the experiment displayed on fig.4.3. It would be interesting in a future work to study the disappearance of stick- slip motion with vibration in orderfor example to compare theses results to the effects of acoustic waves on stick-slip in granular media by Johnson et al. [68]. They show that the stress-drop magnitude decreases due to vibration. However, I had no time to carry this study in detail.

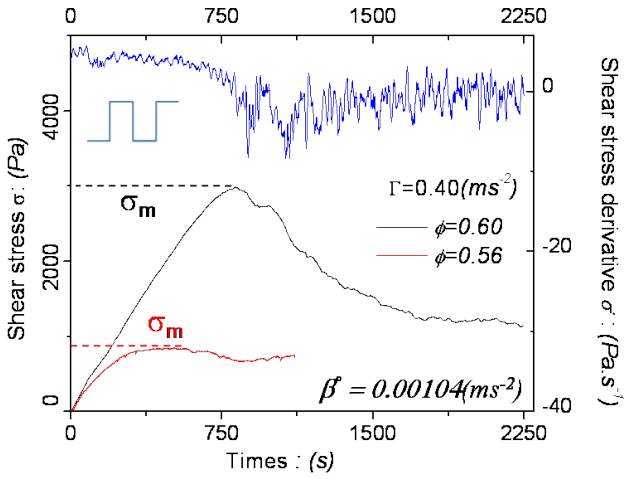

FIGURE 4.3: Response to a ramp stress showing the shear stress as a function of time with the influence of vibration, for two packing fractions with a vibration intensity $\Gamma = 0.40 ms^{-2}$ (bottom), shear stress derivative as a function of time with packing fraction $\phi = 0.60$ (top).

Fig.4.4 (left) shows the response of the granular medium to a stress ramp with a sinusoidal tension input for three frequencies ($600Hz$, $850Hz$ and $1000Hz$) such that the tension yields a similar r.m.s acceleration $\Gamma = 0.25 ms^{-2}$ (see fig.2.20), the motor rate being $\dot{\beta} = 0.00104\ rd/s$. The value of the maximum shear stress does not display significant differences.

Fig.4.4 (right) is a zoom at small stresses of the relationship between shear stress and deformation for the three previous frequencies (see corresponding zone in Fig.4.4 (left)). Again, results showed no large differences between the three frequencies. However, what is remarkable is the onset of large plastic deformation jumps for deformations of the order of $\Delta\gamma_c \approx 310^{-4}$. Below this value the elastic stiffness of the system is recovered.

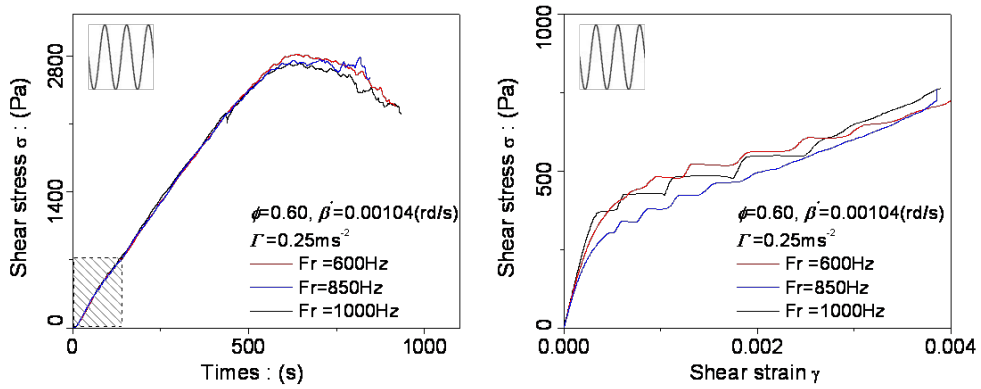

FIGURE 4.4: *Influence of vibration with sinusoidal voltage input on shear stress at a packing fraction* $\phi = 0.60$, response to a stress ramp (left), shear stress-shear strain relation (right).

I measured the maximum shear stress under vibration at different packing fractions. I used a

driving frequency with $f = 100Hz$ and tension input being a square corresponding to a vibration level of $0.40ms^{-2}$. I found that the maximum shear stress is reduced (see fig.4.5 left). Interestingly, these stress values of the maximum shear stress in the case of vibration and no vibration are strongly related since their ratio remains constant : ≈ 1.4 (see upper part of fig.4.5 left).

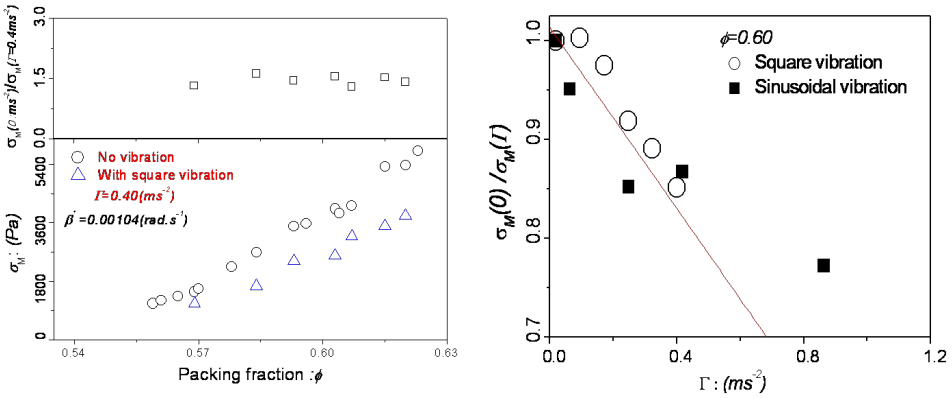

FIGURE 4.5: Maximum shear stress σ_M with vibration and no vibration as a function of the packing fraction (bottom) and its ratio as a function of the packing fraction (top) (left), and its ratio as a function of vibration level for a packing fraction $\phi = 0.60$ with two vibration types, (fit line : $y = 1-(x-a)b$ with $a = 0.03$ and $b = 4.5/g$) (right).

At a fixed packing fraction $\phi = 0.60$ and varying the vibration level, I measured the maximum shear stress σ_M. I found that the maximum shear stress decreases rapidly as a function of Γ. Experiments were carried for square and sinusoidal tension input as described on fig.4.5 (right). This is consistent with the influence of vibration on the shear elastic modulus (see fig.4.1). With $\sigma_M(0)$ and $\sigma_M(\Gamma)$ the maximum shear stress with vibration and no vibration respectively. We found that with $\Gamma < 0.5ms^{-2}$, the maximum shear stress decreased almost linearly with the vibration level measured with the RMS acceleration.

4.4 Réponse du fluage à une contrainte constante

In this section, we study the creep dynamic of the granular material under vibration. Such as for the study of the elastic response and the stress ramp, two vibration methods were used : vibration with square and sinusoidal tension. The vibration was triggered from the beginning of the test, i.e. as soon as the stress ramp started. The motor rotates at $\dot{\beta} = 0.00104rd/s$. The nominal applied stress is reached in about 3-4 minutes. The study is done at a fixed packing fraction $\phi = 0.60$ with various r.m.s accelerations Γ and applied shear stresses σ. With a square tension input, fig.4.6 (left) shows the creep deformation at different of vibration levels for the same applied shear stress $\sigma = 400Pa$. Note that in these conditions, the maximum stress is $\sigma_M = 2800Pa$. On fig.4.6 (right), creep deformations curves are displayed at different shear stresses for an applied vibration $\Gamma = 0.25m/s^2$. We found logically that the creep deformation increases with the vibration level and the shear stress.

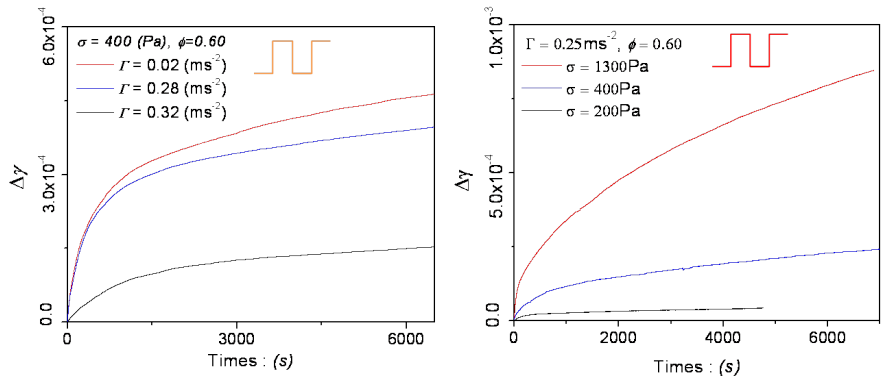

FIGURE 4.6: *Creep deformation with square tension input and packing fraction* $\phi = 0.60$, for different vibration levels at applied shear stress $\sigma = 400Pa$ (left) and for different applied shear stresses at r.m.s vibration $\Gamma = 0.25ms^{-2}$ (right).

We found that the creep deformation follows a long-time logarithmic law quite similar to what was found previously. This is confirmed on fig.4.7by the linear relation between $\dot{\gamma}^{-1} - \dot{\gamma}_0^{-1}$ and time. The slope C is obtained from a linear fit. Note that $\dot{\gamma}_0$ was obtained from each creep curve by a fit as explained in chapter 3. Similar couple of parameters $\dot{\gamma}_0$ and C were obtained for sinusoidal driving (see fig.4.8).

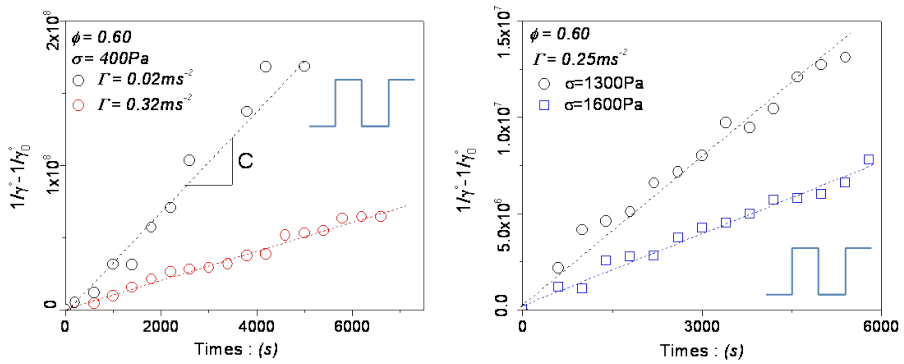

FIGURE 4.7: *Plot of* $\dot{\gamma}^{-1} - \dot{\gamma}_0^{-1}$ *as a function of time for square vibration,* different r.m.s vibrations (left) and different shear stresses (right).

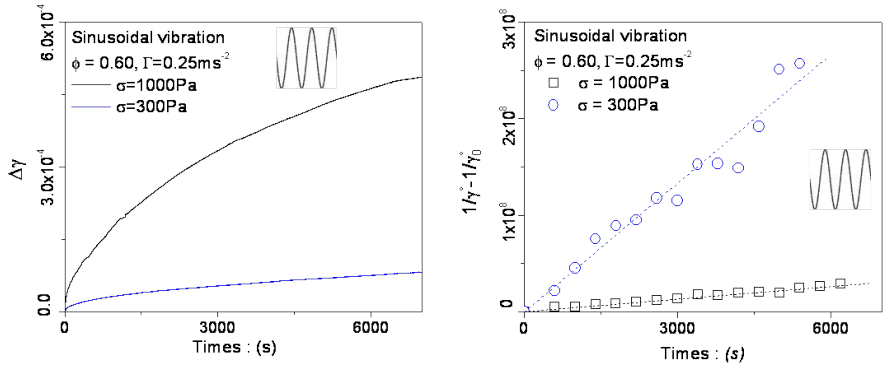

FIGURE 4.8: Creep deformation with different shear stresses, the packing fraction $\phi = 0.60$ and r.m.s vibration $\Gamma = 0.25 ms^{-2}$, sinusoidal tension input (left), plot of $\dot{\gamma}^{-1} - \dot{\gamma}_0^{-1}$ as a function of time (right).

On fig. 4.9 (left), I plot the relation between $\dot{\gamma}_0$ and σ and compare it with the relation without vibration. It appears that contrarily to the previous chapter, the relation is not linear anymore. It might still be linear at weak shear stress, with a slope larger than the case with no vibration. It eventually identifies at larger stresses, with the no-vibration curve. I pursue the analyzis of theses experimental results using the model of Derec et al.[13] as it has been done in the case of dry grains without vibration. In this framework, two parameters were extracted from the experimental data, the "initial fluidity", f_0 and the "equivalent aging", a_{eq} (see eqs 3.21 and 3.20). These parameters will be compared to those obtained in the absence of vibration when varying, shear stress and RMS acceleration.

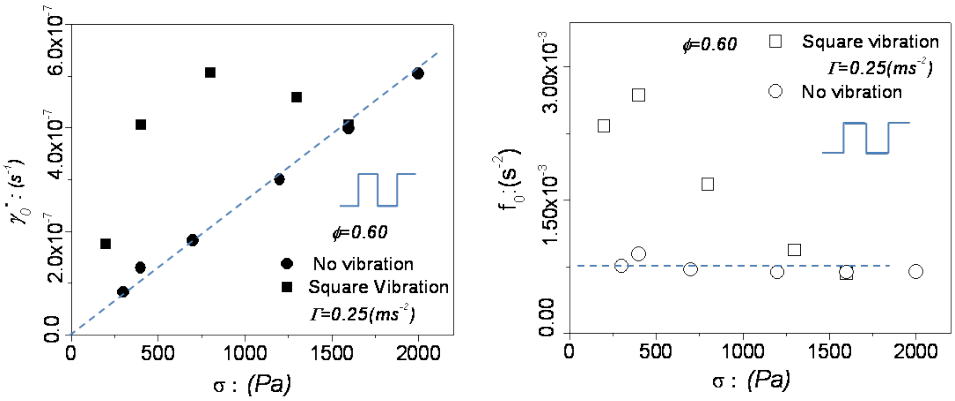

FIGURE 4.9: Initial shear strain rate as a function of the shear stress with square vibration and no vibration, the dotted lines are linear fits (left)and initial fluidity as a function of shear stress at r.m.s acceleration $\Gamma = 0.25 ms^{-2}$ and packing fraction $\phi = 0.60$ (right).

Along those lines, I represent on fig.4.9 (right) the initial fluidity f_0 as a function of shear stress.

In spite of the fact that more data point would be needed to reach a firm conclusion, it seems that this curve reaches a low stress value close to $\approx 2,8.10^{-3}$, which characterize an initial rate of stress relaxation higher with vibration than without vibration. Now I choose a low value of stress ($\sigma = 400pa$), to study the variation of f_0 with the vibration level. On fig.4.10 (left) it appears that under this constant applied stress, f_0 increases linearly with Γ at a given packing fraction. On this plot the value without vibration was plotted with the actual noise value measured with the accelerometer. The curve seems to be quite linear and interestingly, interpolates at a value which is different of zero for $\Gamma = 0ms^{-2}$. This las result may indicate the presence of a relaxation mechanism different from the mechanical vibrations. One can think of thermal processes activated at the level of contact plasticity.

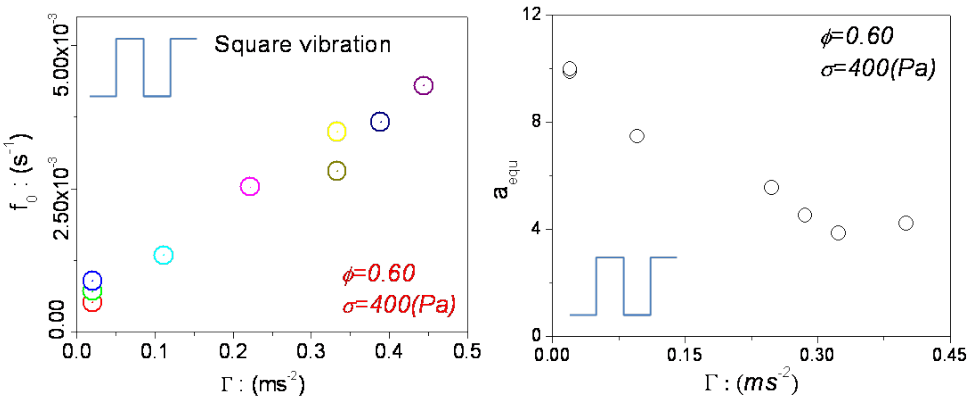

FIGURE 4.10: For shear stress $\sigma = 400Pa$, packing fraction $\phi = 0.60$ and square vibration; Initial fluidity f_0 (left) and ageing parameter a_{eq} as a function of the RMS acceleration Γ (right).

Now in the same conditions, I display the values of the 'aging parameter' a_{eq} (see fig.4.10 right) at different vibration levels. The fluidization effect is marked by an important drop of the the ageing parameter with Γ. From fig.4.11, I find that a_{eq} decreases monotony with the shear stress for an acceleration r.m.s of $\Gamma = 0.25ms^{-2}$ for the two types of vibration (square and sinusoidal tension input). Results showed that a local minimum indicating dynamical hardening with stress cannot be detected consistently with the response of a granular medium to a stress ramp (see section 4.3). where the 'first rupture stress' disappears in the presence of vibration. In both cases, vibration and without vibration, the 'aging parameter' a_{eq} seems to reach a same value when $\sigma = 0$. We find that a_{eq} approach to 0 when σ near to σ_D, the packing starts to exhibit a fluidity regime. Results shown on fig.4.11 allow us to estimate the value of $\sigma_D \approx 2800Pa$. This value is the dynamical shear stress corresponding to the steady shear rate in the case of without vibration. In presence of vibration $\Gamma = 0.25ms^{-2}$, the maximum shear stress is $\approx 2800Pa$ with $\phi = 0.60$.

The value of a_{eq} depends also on the applied shear stress. When we displayed a_{eq} as a function of the vibration level, we found logically that this value decreases with a vibration level (see fig.4.11 right). Then, we can assume that a_{eq} decreases monotony with σ and Γ in presence of vibration. From results showed in fig.4.5 (right), we can estimate that $\sigma = 400Pa$ is maximum shear stress of packing if $\Gamma \approx 1.8ms^{-2}$. This means that $a_{eq} = 0$ when $\sigma = 400Pa$ and $\Gamma \approx 1.8ms^{-2}$. This is consistent with what is shown on fig.4.11 if we consider that the value of a_{eq} decreasing linearly

with the vibration level.

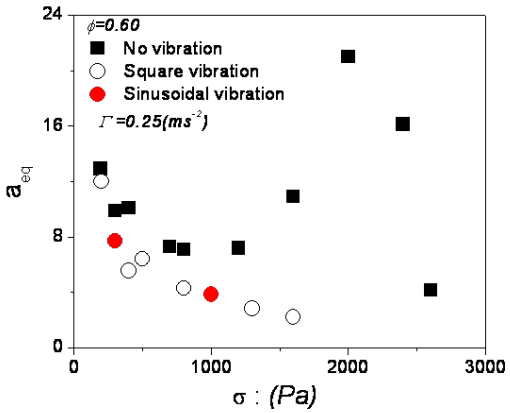

FIGURE 4.11: *Evolution of the aging parameter a_{eq} at a packing fraction ϕ* = 0.60, as a function of the shear stress with square (∘) and sinusoidal (•) vibration and no vibration

4.5 Conclusion

In presence of weak vibrations, we found that the mechanical properties and the creep dynamics is only dependent on the r.m.s acceleration. We presented the evolution of the elastic response and the maximum shear stress as a function of r.m.s acceleration Γ. Creep dynamics varies strongly with vibration for both types of vibration studied : square and sinusoidal tension input. Logarithmic creep was observed for the two types of vibration introduced. The results presented in this chapter is consistent with what is found in the case of no vibration, the 'ageing parameter' a_{eq} approach to 0 when the shear stress approach to the dynamic shear stress σ_D. A monotony diminution of a_{eq} would to indicate that no existence of reorganization in the granular medium under shear stress.

CHAPITRE 5

INFLUENCE DE LA QUANTITÉ D'EAU AJOUTÉE

Contents

5.1 Introduction

Most studies about granular medium are focused on dry granular medium, without any liquid between nearby beads. However, in various domains such as geology and many industrial applications (e.g. food processing, pharmaceuticals, ceramics, civil engineering, constructions), the granular medium is wet. Moreover in soil science, it is known that even sandy soil, which are the closest of a granular packing as we model it, contain a substantial amount of water. From the mechanical point of view, it is well known that the granular medium behavior is strongly different for wet granular media as observed for sand castle construction which has led to several physical studies [18, 75, 90] aiming to clarify the effects of capillary bridges between the grains on the material yield properties.

In this chapter, I study in the context of our experimental shear cell, how water content affects the mechanical properties of a granular packing. The experiments were designed to prepare a controlled wet sample and the details of preparation were presented in Chapter. 2. The aim is to perform mechanical test as done in Chapter.3 for dry samples. Also, the study is just preliminary since I had no time to carry systematic measurements. I will only here present the proof of principle that water content modifies drastically elastic, strength and creep properties of the packing. Initial packing at a given packing fraction (essentially at $\phi = 0.6$). Note in addition, that for every experiment, the shear vane is always introduced in the packing before the injection of humid air. The mechanical measurements are performed when the desire water content is obtained.

An important question is to know to which extend the addition of water may change the packing fraction. Actually, Feng et al. [15] have measured experimentally that the water content W influences the packing fraction only at high water content ($W \approx 1\%$). In our experiments, we add very small amount of water (typically $W \approx 0.2\%$). As a consequence, we may assume that the packing fraction stays unchanged, at least globally. Also, the room temperature could range between the extreme values $15^{\circ}C$ and $25^{\circ}C$, however we kept a relative humidity $30 \pm 5\%$. In these conditions, the measured water quantity for a dry granular media was always around $W = 0.05 \pm 0.02\%$.

5.2 Module élastique G

The experiments consist in measuring the shear modulus G for the granular medium at a given water content. The method is described in chapter 3. On fig.5.1 (left), I represent the influence of the water content W on the relative shear modulus $\frac{G}{G_0}$, where G_0 is the shear modulus for a dry granular medium ($W \approx 0.05\%$). Fig.5.1 (left) shows a slight increase of $\frac{G}{G_0}$ as a function of W for water content values below $W = 0.14\%$. Above this water content value, the shear modulus value does not change anymore as a function of W. The increase in material stiffness is a natural consequence of the presence of capillary bridges which provides cohesion to the packing. Typically there ate two contributions (i) stiffness increase due to the Hertz non-linear behavior, (ii) contribution of the elastic response due to the capillary bridge deformations. The resulting contribution at the macroscopic scale is a difficult issue as it depends on the geometrical distribution of capillary bridges in the packing. Note that the non-linear Hertz contribution is potentially a strong effect in our situation. If on estimates naively the relative increase in modulus as : $\delta G/G = 1/3\Delta P/P$ for a capillary overpressure $= \gamma/d \approx 350Pa$ (with water) and a confining pressure of $P = 10^3 Pa$ one gets

$\delta G/G = O(1)$.

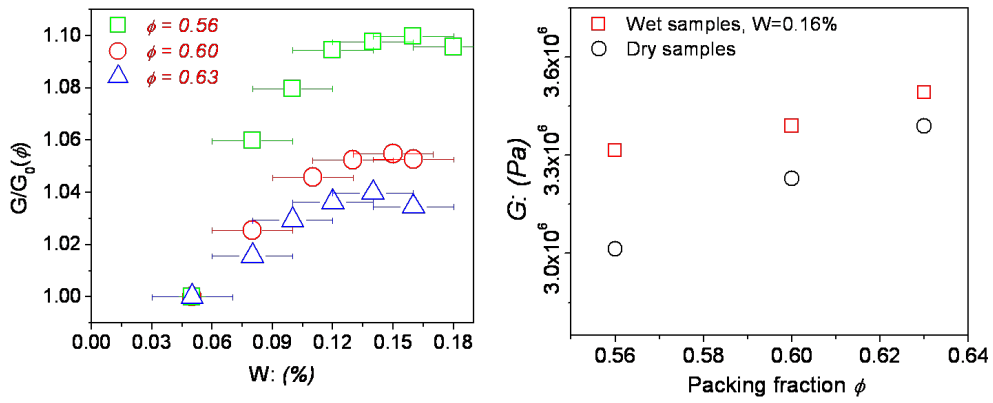

FIGURE 5.1: *Elastic shear modulus G*. Normalized shear modulus G/G_0 as a function of the water content W for different packing fraction values (left) and shear modulus as a function of the packing fraction for the dry sample and the wet sample with a water content value of $W = 0.16\%$ (right).

The discussion on chapter 2 based on the article by Hornbacker et al. [18], indicates that, for the water content we use, we are in the rising part of the relation between water content and the mean number of contacts per grains. This could explain qualitatively the increase in stiffness with W. However, we observe a saturation for value around $W = 0.14$. We do not have a clear explanation for this besides the fact that we may reach a plateau in mean number of contact per grains (around 6) as shown by Hornbacker et al. [18]. The effect is at the maximum of the order of $\delta G/G = 10\%$, a little bit smaller than what was estimated naively before. Note also, that if we follow strictly their curve this cross-over comes a little bit early in water content. Finally, that the effect stays qualitatively the same for different packing fractions. On Fig.5.1 (right), we see that the shear elastic modulus increases also with the packing fraction for a water content value $W = 0.16\%$.

5.3 Influence de la quantité d'eau sur le seuil de Coulomb

I measured the maximum shear stress σ_M for a wet sample using the same protocol as for dry granular matter(see Chapter 3). On fig.5.2 (left), an example of the response to a stress ramp is shown. The shear stress increases almost linearly as a function of time until it reaches the threshold value σ_M, for which a huge drop of stress is observed. We do not observe a succession of local ruptures as it was the case for dry granular matter. On the upper part of fig.5.2 (left), the shear stress derivative is represented as a function of time. The curve is almost horizontal up to the maximum shear stress.

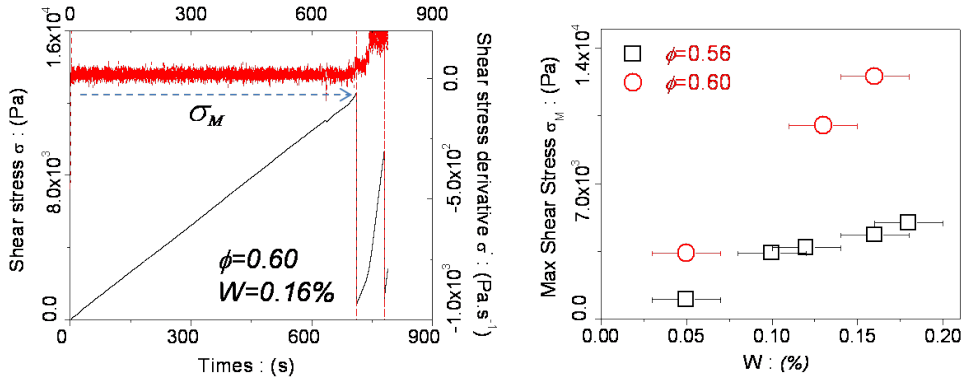

FIGURE 5.2: Shear stress as a function of time for a test ramp stress with parameter values $W = 0.16\%$, $\phi = 0.60$ (left) and the Coulomb threshold σ_M as a function of the water content $W(\%)$ for two different values of the packing fraction (right).

On fig.5.2 (right), σ_M is displayed as a function of W for two different values of the packing fraction. Note that on this graph, $W = 0.05\%$ corresponds to the water content measured for a dry granular medium in standard experimental conditions. The main point is that σ_M increases strongly as a function of W, with a trend almost linear. Somehow, the strong dependence with W, is expected, as we recall that the capillary cohesive pressure $P_c \approx \gamma/d \approx 10^3 Pa$ is comparable to the hydrostatic confining pressure $P = \rho g h \phi \approx 10^3 Pa$. We also observe on fig.5.2 (right) that the higher is the packing fraction value, the stronger is the increase of $\sigma_M(W)$. The sensitivity of this dependence with a small change in packing fraction is indeed a remarkable effect. In our study, if we consider that the confining pressure does not change with a very small water content W, in the framework of a simple Mohr-Coulomb criterion, it simply means that the cohesion increases linearly with W. This would correspond to the low water content identified by Scheel et al. [61] when they measure directly the tensile strength of a wet packing. At higher water content ($1\% < W < 3\%$) one would expect a nonlinear relation and a subsequent saturation ($W_m > 3\%$) as measured experimentally by Richefeu et al.[91].

5.4 Fluage

The study of dynamic creep in the presence of water is an important issue in soil science, for example the phenomenon of settlement due to a high water content or issues around root penetration in sandy soils. In our study, we focus on the dynamical creep properties for very weak water content values. After preparation of a dry sample , the shear vane $h = 5cm$ is introduced and water injected as described in chapter.2. The creep tests is performed under a constant applied shear stress after a stress ramp of $3-4$ min. The sample surface is covered by a light lid to prevent evaporation. During the creep tests, I measured a relative humidity beside the admission chamber (fig.2.2) always superior to 90%. For the same packing fraction $\phi = 0.60$ and at a shear stress value $\sigma = 2000$ Pa, on fig.5.3 (left), are displayed the creep curves describing the influence of the water content. The creep deformation decreases quite strongly with W.

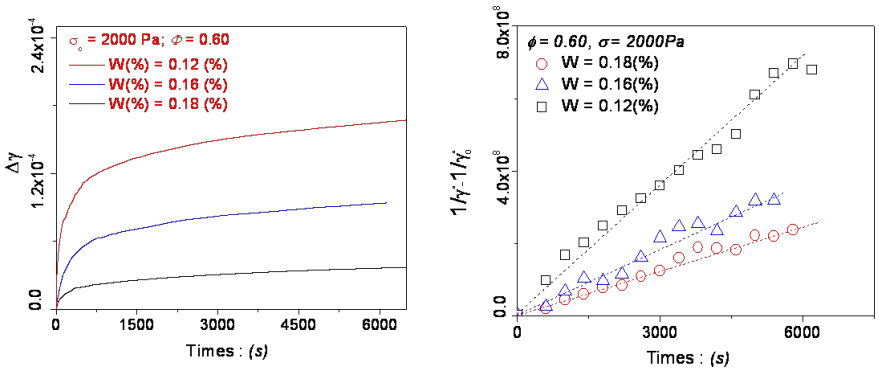

FIGURE 5.3: *Creep experiments at a constant packing fraction* $\phi = 0.60$ *for various water content values.* Creep deformation $\Delta\gamma$ as a function of the water content W (left) and $\dot{\gamma}^{-1} - \dot{\gamma}_0^{-1}$ as a function of time (right).

I also performed creep tests for two different values of packing fraction and shear stress as presented on fig.5.4. We can see that the logarithmic law for the creep is still observed. We found as expected, that the creep deformation increases and decreases respectively as a function of shear stress and packing fraction for a given value of W.

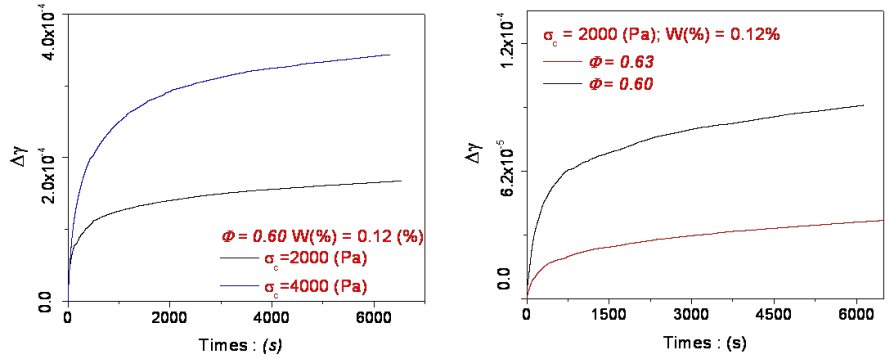

FIGURE 5.4: *Creep deformation* $\Delta\gamma$ *with water content* $W = 0.12\%$ under different values of shear stress at packing fraction $\phi = 0.60$ (left) and under different packing fraction values at shear stress $\sigma = 2000$ Pa (right).

Fig.5.3 (right) shows that the creep deformation for a wet sample follows a logarithmic law as a function of time, because we observe a linear relation $\dot{\gamma}^{-1} - \dot{\gamma}_0^{-1} = Ct$.

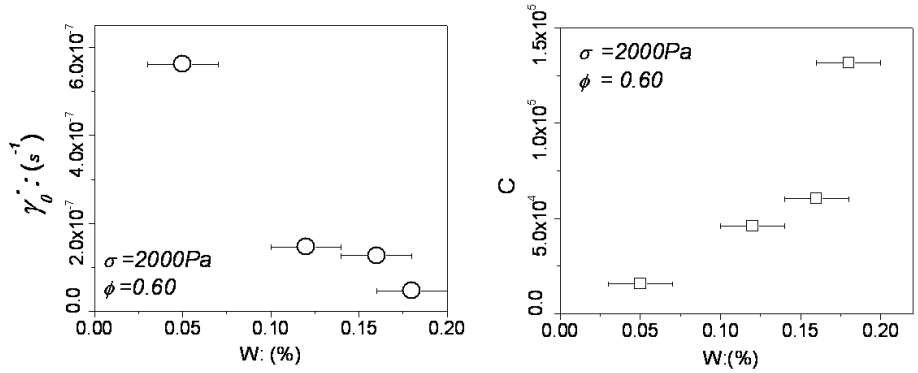

FIGURE 5.5: Evolution of the initial strain rate $\dot{\gamma}_0$' (left) and the "'creep slope" C (right) as a function of water content W, at a packing fraction $\phi = 0.60$ and a shear stress $\sigma = 2000$ Pa.

From the creep curves, I extracted the initial strain rate $\dot{\gamma}_0$ and the "creep slope" C which are displayed are displayed on fig.5.5 as a function of the water content W . These values are obtained at a packing fraction $\phi = 0.60$ and a shear stress $\sigma = 2000Pa$.

A remarkable result is that $\dot{\gamma}_0$ decreases very strongly with W and C increases. By simple linear interpolation one estimate the crossing of $\dot{\gamma}_0 = 0$ when W approaches 0.2%. On the other hand, at this value, C seems to strongly increase and possibly diverge. This would mean that the packing "solidifies"above this value of W around $0.25 \pm 0.05\%$.

5.5 Conclusion

We have demonstrated that adding a very small amount of water can modify strongly the mechanical properties of granular packing. Furthermore, the elastic response and the Coulomb threshold increases with W. We completed previous studies about the dependence of material resistance at low water content values. Finally, the logarithmic law for the creep of wet sample is still observed.

CONCLUSION ET PERSPECTIVES

In my thesis I tackled a question which had been so far, rarely considered in the physicist community : the problem of slow relaxation processes and creep, below the rupture threshold in granular packing. I considered three model situations : dry granular packing without and with vibration and also wet packing.
To this purpose I defined a methodology consisting of three mechanical tests of a granular packing in a shear cell. An important point was to define a protocol suited to prepare the packing at a fixed packing fraction ϕ .
The set-up was built to be able to measure experimentally the shear elastic response, the rupture threshold and the creep dynamics at fixed applied shear stress.

The major part of my work was dedicated to dry granular packing. The elastic response of such packing was found to increase linearly with packing fraction, consistently with mean-field Hertz elasticity. The ramp experiments allowed to define a maximum shear stress before yield which was found to increases with packing fraction. However, in this shear geometry and for slow driving, we identified at all packing fractions a clear "'first rupture threshold"' above which other ruptures could occur but overall, the resisting stress was found to increase up to the maximum shear stress value. For all stresses and packing fraction tested, the creep experiments displayed a slow deformation response that would yield a long time logarithmic response. We characterized this behavior by extracting two parameters : the initial value of the shear rate and a dimensionless coefficient expressing the importance of the creep. These data were analyzed in the context of a rheological model which introduces the concept of "fluidity", which characterizes the rate of stress relaxation due on internal processes in the packing. This is an extension of a classical visco-elatic rheology but with an age dependent fluidity f which is coupled to a dynamical equation for f. We proposed a simple form for this equation based on an original proposition of Derec et al. [13] which contains two antagonistic term : (i) an intrinsic aging parameter (ii) a shear-rate induced rejuvenation process. This model is consistent with the experimental finding and provides an interpretation for the empirical parameters. The linear relation between the initial shear rate and the applied stress allowed to define a rate of relaxation (the initial fluidity f_0) characteristic of the packing preparation. It naturally identifies an effective "viscosity" which diverges at the random close packing limit. The model also allows to define an effective aging coefficient characterizing the creep process. I have shown that with a proper rescaling in $f_0(\phi)$ and in stress by $\sigma_r(\phi)$ the aging curves at different stress and packing fractions could be rescaled onto a master curve. An important feature is that at larger stress the onset on the "first rupture threshold" is directly associated to a dynamical hardening of the packing corresponding to a slow down of the creep before the final yield.

In the context of dry granular packing, using a light scattering technique (DWS), we also provided in collaboration with a team of the Rennes University, a direct visualization of localized

deformation events associated with the mechanical response of a granular packing under shear. The optical DWS technique, manages to capture in a plane perpendicular to the vorticity axis, the emergence of the so-called "hot-spots" characterized by a spatial extension of about ten grains. This is to my knowledge, the first time such localized events were identified experimentally and it connects to the numerical and theoretical studies done in the context of disordered glassy solids [30, 84, 19]. Under a stress ramp, we showed that these events increase in density with the stress amplitude and cluster spatially as precursors of the shear banding macroscopic yield events. The occurrence of the first rupture event is directly associated to the first clustering of the "'hot-spots"'. Under constant applied shear stress, the rate of apparition of these "hot-spots" at the top surface is directly related to the rate of plastic deformation. Varying the applied shear and the surface boundary conditions, we point that at first approximation - possibly corresponding to a mean-field approximate of the problem - the hot-spot dynamics is in direct relation with the "fluidity" parameter and represents the mean rate of stress relaxation.

In the presence of weak vibration, I monitored the mechanical properties as a function the r.m.s acceleration Γ measured in situ using a buried accelerometer. I measured a decrease of the elastic shear modulus with Γ as well a decrease of the maximal shear stress the packing could sustain in the ramp experiment. Interestingly in this case, the first rupture stress disappears but instead, many plastic events could be evidenced along the ramp curve. The creep experiments showed also a slow logarithmic deformation response. However, the addition of vibration is strongly increasing the rate of deformation. I had to time to complete the experiments to test the validity of the fluidity model and study this creep acceleration directly with the DWS technique. This is certainly something to be considered for a future work.

The study of a wet sample was really preliminary. I essentially defined an experimental procedure showing that one could prepare a packing at fixed packing fraction with a controlled water content. In the few mechanical test I performed, I have demonstrated that adding a very small amount of water W, increased the elastic rigidity of the material. The maximal stress increases strongly with W but no partial rupture events were observed. In the range of value for W studied, the creep dynamics remained logarithmic but adding a small amount of water had a strong impact on the creep deformation rate. We almost reached a complete blockade of the system for $W \approx 0.2\%$. Of course an extented study of this effect would be necessary in the future.

ANNEXE

Van Bau Nguyen, Thierry Darnige, Ary Bruand and Eric & Clément. Creep and fluidity of a real granular packing near jamming, *Physical Review Letters*, 107, 138303 (2011).

Axelle Amon, Van Bau Nguyen, Ary Bruand, Jerome Crassous1, and Eric Clement. Hot spots in an athermal system.

Creep and Fluidity of a Real Granular Packing near Jamming

Van Bau Nguyen,[1,2] Thierry Darnige,[1] Ary Bruand,[2] and Eric Clement[1]
[1]PMMH, ESPCI, CNRS (UMR 7636) and Univ. Paris 6 & Paris 7, 75005 Paris, France
[2]CNRS/INSU, ISTO (UMR 6113), Univ. Orleans, 45071 Orleans, France
(Received 10 January 2011; published 21 September 2011)

We study the internal dynamical processes taking place in a granular packing below yield stress. At all packing fractions and down to vanishingly low applied shear, a logarithmic creep is observed. The experiments are analyzed using a viscoelastic model which introduces an internal, time-dependent, fluidity variable. For all experiments, the creep dynamics can be rescaled onto a unique curve which displays jamming at the random-close-packing limit. At each packing fraction, we measure a stress corresponding to the onset of internal granular reorganization and a slowing down of the creep dynamics before the final yield.

DOI: 10.1103/PhysRevLett.107.138303 PACS numbers: 47.57.Gc, 65.60.+a, 83.80.Fg

For granular matter, it is currently accepted that a quasistatic limit exists as for grains of macroscopic size, thermally activated processes can be ignored. At low shear rate, mechanical properties of granular packing are usually described by rate independent constitutive relations [1]. However, there are compelling experimental evidences that this limit is just a short-time approximation and time-dependent processes are significant on the long run [2]. Many numerical simulations based on soft interparticular interactions [3] have brought to the front the idea of an "universal" jamming transition scenario based on a mechanical rigidity threshold separating solid and fluid behavior (see a recent review and references in [4]). However, for real grains, interparticle solid friction was shown to affect the rigidity onset and stabilize packing at compacity below the random-close-packing limit [5]. In this case, experiments have pointed out the central importance of nanometric scales where humidity [6], contact plasticity, tiny thermal variations [7] or weak mechanical external noise [8], do impact significantly the macroscopic dynamics and the rheology. Since the original theoretical propositions of "soft glassy rheology" or "shear transformation zones" [9] various models have tried to capture the complex energy reorganization dynamics taking place in amorphous solids or yield-stress fluids, in relation with their constitutive rheological laws. Microscopically, the emergence of plasticity is often explained via a simple picture where localized elastic instabilities release irreversibly long range elastic constraints [10] which may be organized spatially as shear driven avalanches [11]. Macroscopically, to account for the complex phenomenology, an internal time-dependent variable called fluidity is often introduced [12] to describe the rate of stress relaxation.

In this Letter, we study the creeping dynamics of granular packing under constant shear stress, below the Coulomb limit. In order to reveal the internal relaxation processes and make connection with the behavior of a large class of yield-stress fluids [13], we propose a quantitative analysis using a phenomenological model based on the fluidity concept.

All the mechanical tests are performed at well defined packing fractions ϕ (see Fig. 1). To achieve this goal, the setup is designed as an air fluidized bed. The container is a plastic cylinder of inner diameter $D = 10$ cm closed at its bottom by a metal grid supported by a honeycomb grid. Pressurized air is introduced in an admission chamber below the grid at a controlled overpressure ΔP. We use glass beads of density $\rho = 2500$ kg/m^3 and mean diameter $d = 200$ μm (rms polydispersity $\Delta d = 30$ μm). A mass M of grains is poured into the container such that the typical packing height is $L = 10$ cm. Using a flow rate just above the fluidization value, we obtain after stoppage, an initially loose granular packing at a compacity $\phi \approx 0.56$. Then, by successive tapping on the container side, the packing fraction can be increased up to the desired packing fraction (maximal value $\phi = 0.625$). Note that in the present report, the relative humidity is kept at 35 ± 5%

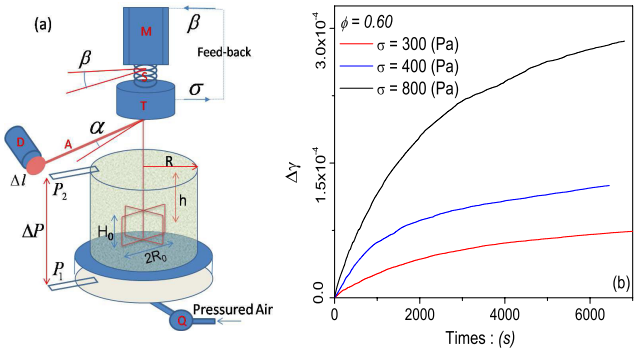

FIG. 1 (color online). (a) Schematics of the shear cell. (M): motor, (S): torsion spring, (T): torque probe, (D): induction distance probe, (A): transversal arm, (Q): flowmeter, P_1: differential pressure probes. (b) Creep deformation: $\Delta\gamma(t)$ under constant shear stress at packing fraction $\phi = 0.60$.

and we work in a "quiet" environment characterized by a background noise quantified by placing in the packing an accelerometer (rms acceleration 0.02 ms^{-2}).

Before each mechanical measurement, the packing fraction value is evaluated from a linear fit between pressure drop ΔP and flow rate Q: $\Delta P = \lambda Q$, stemming from Darcy's law [14]. The relation between permeability K and packing fraction was calibrated by a preliminary series of experiments and a Carman-Kozeny relation was obtained: $K(\phi) = A\frac{(1-\phi)^3}{\phi^2}d^2$, with $A = 1/165$. Consequently, for a mass M of grains poured in the cylinder the packing fraction is obtained through the relation $K(\phi)\phi = \eta\frac{4M}{\lambda\pi D^2\rho}$, where $\eta = 1.85 \times 10^{-6}$ Pa · s is the air viscosity. To shear the granular packing, we use a four-blade vane in stainless steel of height $H_0 = 2.54$ cm and diameter $2R_0 = 2.54$ cm [see Fig. 1(a)], introduced at a depth $h = 5$ cm below the surface prior to the initial fluidization process. This procedure creates reproducible initial conditions. Shear stress is applied through the vane (see Fig. 1) connected axially to a torque probe (T) itself coupled to a brushless motor (M) via a torsion spring (S). The vane rotation angle α is monitored via a transversal arm (A) whose rotation is followed by a displacement induction probe (D). The motor rotation angle β is imposed with a $2\pi/10\,000$ precision. Torque and displacement signals as well as the motor command are connected to a Labview controller board. The last one is programmed to impose a motor rotation rate or a fixed stress using a feedback loop on the torque signal. In the following, we ignore the stress and strain spatial distribution due to the Couette cell geometry and define only average values obtained from measurements of angular rotation α and torque T. The mean packing deformation γ is defined as $\gamma = \frac{\alpha R_0}{R-R_0}$ and the mean shear stress is $\sigma = \frac{T}{2\pi R_0^2 H_0}$. On Fig. 1(b), we display three examples of creep curves $\Delta\gamma(t) = \gamma(t) - \gamma(0)$ obtained at fixed compacity and shear stress values σ.

Elastic response.—To obtain the elastic response of the packing initially prepared at a given packing fraction, stress cycles were performed corresponding to sinusoidal deformations of small amplitudes around 10^{-5}. The cycles were carried out under constant mean confining pressure (hydrostatic loading). In the short-time limit, the response is essentially reversible [see inset of Fig. 2(a)]. Accounting for the apparatus stiffness, we extract the effective elastic shear modulus which increases with packing fraction almost linearly: $G = G_0\phi$ [see line on Fig. 2(a)], with a value of $G_0 = 5.38 \times 10^6$ Pa. Interestingly this simple result is consistent with a mean-field Hertz elasticity theory (see [15] and references within) where under a confining pressure $P_0 = \rho\phi g h$, the shear modulus scales as $G_{\text{eff}} \propto E_0(\phi Z)^{2/3}(\frac{P_0}{E_0})^{1/3}$, where Z is a constant mean contact number and E_0 the material Young's modulus, meaning that, in the range of density explored, the contact density at the origin of the ϕZ term varies linearly with ϕ.

Response to a stress ramp.—To identify the maximal stress supported by the packing before yield, shear stress ramps were applied at a constant motor rotation rate ($\dot{\beta}$), using the softest spring constant available ($k = 2.45 \times 10^{-3}$ Nm/rd). On Fig. 2(a), the stress response at $\phi = 0.60$ is displayed as a function of time. At first, a linear increase of the stress is observed with a slope corresponding to the spring constant. Then, at a given stress level σ_r, we observe the emergence of well-marked and sudden granular material reorganizations [see top view on Fig. 2(b)] in the form of rather equidistant events corresponding to stress drops and large plastic deformations ($\delta\gamma = 10^{-3} - 10^{-2}$). We define this stress value as the "first rupture stress": σ_r. However, stress can still be increased but undergoes series of partial rupture, up to a maximal value σ_M followed by a large stress jump. Then, a subsequent stick-slip dynamics is observed. Interestingly, such a structured fluctuation regime was also observed by Albert *et al.* [16] for the drag force on an intruder near jamming. In our case, the maximal stress value

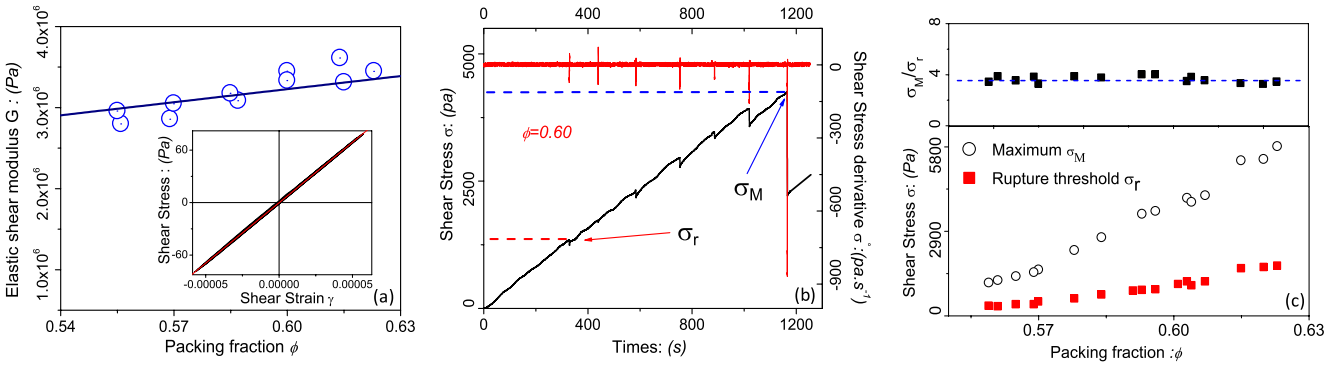

FIG. 2 (color online). (a) Shear modulus $G(\phi)$ under gravity confinement. Straight line $y = G_0 x$, with $G_0 = 5.38 \times 10^6$ Pa. (b) Response to a stress ramp: shear stress σ as a function time for $\dot{\beta} = 0.001\,04$ rd/s and a packing fraction $\phi = 0.6$. First rupture stress σ_r and maximal stress σ_M are displayed as horizontal dotted lines. (c) For the same rotation rate, σ_r, σ_M and the ratio $\frac{\sigma_M}{\sigma_r}$ as a function of packing fraction.

corresponds to a Coulomb yield criterion as we verified that its value increases linearly with the confining pressure. Such experiments were performed varying packing fraction and ramp velocities and we only display here stresses obtained at the slowest driving velocity where the values are quite insensitive to the rotation rate. On Fig. 2(b), the rupture, maximal and dynamical stresses are displayed as a function of packing fraction for a rotation rate ($\dot{\beta} = 0.001\,04$ rd/s). The values increase strongly with packing fraction. Interestingly these stress values are strongly related since their ratio stay constant with packing fraction: $X = \sigma_M/\sigma_r = 3.5 \pm 0.2$ [see upper part of Fig. 2(b)].

Creep flow.—This part is concerned with the creep response of the granular packing under constant shear stress. The packing fraction is varied between 0.56 and 0.625. The procedure consists of two steps. First, a monotonic loading up to the desired stress value. This initial step is fast with respect to the creep dynamics, typically less than 200 s. We verified that this loading time is much smaller than the inverse of the initial shear rate. Second, a phase of constant applied shear stress is obtained by a feedback procedure where stress is maintained at a constant value within a range less than 1%. The onset of feedback defines the initial time $t = 0$. If stress leaves the assigned range, a command is sent to the motor to rotate the torsion spring and to adjust the torque accordingly. From time to time, as a consequence of this fast motor rotation, an acceleration of the strain rate is observed, followed by a decay down to the value before the jump. These dynamical phases lasting less than 20 s were replaced by a linear interpolation of the shear rate so that they do not artificially perturb the subsequent analysis. For all the experiments, we observe a slow increase of the deformation $\Delta\gamma(t)$ [see Fig. 1(b)]. The creep dynamics increases with the applied shear stress and decreases for larger values of the packing fraction. To quantify the creep dynamics, strain rates were computed for a time step $\delta t = 1$ s and averaged over a time window of $\Delta T = 400$ s. On Fig. 3(a), we display $\dot{\gamma}^{-1} - \dot{\gamma}_0^{-1}$ as a function of time for a fixed packing fraction at different applied shear stresses; $\dot{\gamma}_0$ being the initial shear rate. This representation is a natural choice to probe a long-time logarithmic dynamics (consistent with $\dot{\gamma} \propto 1/t$). Indeed, we observe a relation of the type: $\dot{\gamma}^{-1} - \dot{\gamma}_0^{-1} = Ct$, corresponding to a long-time logarithmic creep : $\gamma = \gamma_0 + \frac{\dot{\gamma}_0}{C}\ln(1 + Ct)$. On Fig. 3(b), we represent the values of C extracted from a linear fit as a function of $G(\phi)/\sigma$, for different packing fraction values. We observe a monotonic increase, more prononced at larger packing fraction.

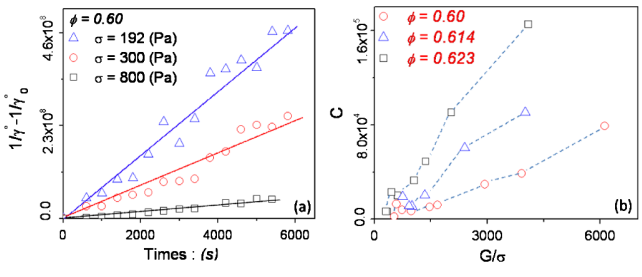

FIG. 3 (color online). Creep experience. (a) plot of $\dot{\gamma}^{-1} - \dot{\gamma}_0^{-1}$ as a function of time for creep experiments performed a constant packing fraction $\phi = 0.6$ for various shear stresses, the straight lines are linear fits : $y = Ct$. (b) Values of the fitted slopes C as a function of $G(\phi)/\sigma$ for three values of packing fractions.

Rheological model.—To analyze quantitatively the data, we use a theoretical model introduced by Derec *et al.* [12] in the context of complex fluids rheology. We propose here to adapt it to the creep flows of granular packing. The model extends naturally the standard Maxwell viscoelastic rheology. It introduces an internal phenomenological variable f called fluidity whose dimension is an inverse time. Physically, fluidity is a rate of stress relaxation. To describe a complex dynamics displaying ageing and rejuvenation, Derec *et al.* propose that fluidity should be time-dependent and its dynamics described by a simple "*à la* Landau" phenomenological equation:

$$\partial_t\sigma = -f\sigma + G\dot{\gamma}, \tag{1}$$

$$\partial_t f = -af^2 + r\dot{\gamma}^2. \tag{2}$$

The second equation introduces two dimensionless and positive parameters a and r. The first term corresponds a fluidity decrease, i.e., an ageing process which renders the fluid more "viscous" with time. We call a the "ageing parameter." The second term, corresponds a fluidity increase (less viscous) due to shear. We call r the "rejuvenation" parameter. The forms assumed by the ageing and rejuvenation terms are the most simple one can get in an expansion consistent with a nontrivial longtime dynamics (see discussion in [12]). At constant shear stress σ, one obtains the relation $f\sigma = G\dot{\gamma}$, yielding : $\partial_t f = -a(1 - (\frac{\sigma}{\sigma_D})^2)f^2$, where $\sigma_D = G\sqrt{a/r}$ is the dynamical shear corresponding to steady shear rate and steady fluidity. Introducing an equivalent ageing parameter:

$$a_{\mathrm{eq}} = a\left(1 - \left(\frac{\sigma}{\sigma_D}\right)^2\right) \tag{3}$$

the solution of this equation is then: $f(t) = \frac{f_0}{1+a_{\mathrm{eq}}ft}$. The shear rate variation is thus: $\dot{\gamma}^{-1} - \dot{\gamma}_0^{-1} = \frac{G}{\sigma}a_{\mathrm{eq}}.t$ which leads to a long-time logarithmic creep as observed experimentally. The experimental slopes C of Fig. 3(b) can then be identified using the relation:

$$a_{\mathrm{eq}} = C\frac{\sigma}{G}. \tag{4}$$

For all experiments performed at different stresses and packing fractions, the initial fluidity value $f_0 = G(\phi)\dot{\gamma}_0/\sigma$ can be plotted as a function of ϕ. For all stresses, data collapse onto a quasilinear curve (see inset

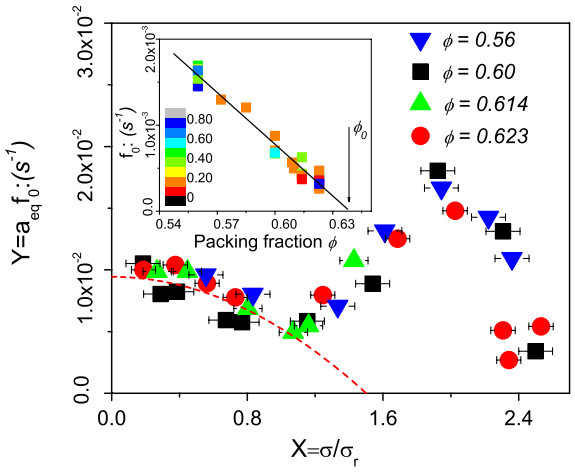

FIG. 4 (color online). Rescaled ageing parameter $a_{\mathrm{eq}} f_0$ as function of rescaled of shear stress $\frac{\sigma}{\sigma_r}$, dotted line: $y = \frac{1}{t_*}(1 - (\frac{x}{1.5})^2)$ with $t_* \cong 106$ s. Inset : initial fluidity f_0 as a function of packing fraction for different shear stresses, the color index reflects the ratio σ/σ_M, fit line: $y = F(\phi_0 - \phi)$ with $F = 0.0203$ and $\phi_0 = 0.635 \pm 0.002$.

of Fig. 4); the denser is the packing, the less is the initial fluidity. The linear extrapolation of this curve to $f_0 = 0$ yields a value $\phi_0 = 0.635 \pm 0.002$, close to random close packing of monodisperse spheres. This can be interpreted as an arrest of the creep dynamics at a packing fraction corresponding to the jamming limit for a random assembly of frictionless spheres [17]. Furthermore, the ageing dynamics can be characterized by computing the equivalent ageing parameter a_{eq} according to relation (4). If a and r are independent of shear, a_{eq} should decrease quadratically and reach a zero value at a finite stress corresponding to the dynamical stress σ_D according to relation (3).

Interestingly, the initial fluidity f_0 sets a time scale which can also be interpreted as an effective viscosity $\eta_0 = G(\phi)/f_0(\phi)$ diverging when approaching the jamming threshold from below : $\eta_0 \propto (\phi_0 - \phi)^{-1}$. Since, in principle, we are well below any thermalized regime where the viscosity concept could apply, this result is quite remarkable. Moreover, we can use this original time scale to rescale the effective ageing parameter and obtain a collapse of all the data. On Fig. 4, we plot $Y = f_0 a_{\mathrm{eq}}$ as a function of the nondimensionalized stress: $X = \sigma/\sigma_r$. The striking feature is that all data collapse onto a single curve for the entire range of stresses and packing fractions studied. The second important feature is that a_{eq} displays a non monotonic behavior with a minimum value at $\sigma \approx \sigma_r$ $(X = 1)$ corresponding to the onset of the strain rate bursts identified in the stress-ramp experiments. This behavior is clearly the signature of internal granular reorganizations leading to a slowing down of the creep dynamics instead of an increase as one might expect when shear is increased. For values above $X \approx 2$, the creep dynamics increases again before reaching the dynamical stress threshold $(a_{\mathrm{eq}} = 0)$ at $\sigma_D \approx 2.4\sigma_r$. For the smaller values of shear stress, i.e., below σ_r, the predictions of Derec's model with constant coefficients can still be validated with a dynamical stress $\sigma_D = 1.5\sigma_r$ (see dashed line on Fig. 4).

This experimental study shows that down to vanishing low applied shear and up to the yield-stress value, internal relaxation processes are present in a granular packing. The logarithmic creep hence observed, was analyzed using a simple viscoelastic model which introduces a time-dependent rate of relaxation (the fluidity). The dynamics is viewed as a competition between intrinsic ageing and shear stress rejuvenation. The model allows a dynamical characterization of the initial packing fluidity which decreases linearly with packing fraction and vanishes at the random-close-packing limit. Under finite stress, we identified the onset of internal reorganizations, slowing down the creep process and setting the yield stress to higher values. This process could be related to the onset of shear induced anisotropy [18] or shear band formation. This internal dynamics is the sign of a peculiar fragility of this type of solid, possibly mediated by thermal activation or by background mechanical noise. It may also be related to the intrinsic nature of the plastic response in amorphous solids [11], which are sometimes described as structurally fragile under finite shear [19,20].

We acknowledge the financial of the support CNRS-PEPS program and the ANR *Jamvibe-2010*.

[1] D. M. Wood, *Soil Behaviour and Critical State Soil Mechanics* (Cambridge University Press, Cambridge, England, 1990).
[2] J. H. Schmertmann, J. Geotech. Eng. **117**, 1288 (1991).
[3] C. O'Hern *et al.*, Phys. Rev. E **68**, 011306 (2003).
[4] M van Hecke, J. Phys. Condens. Matter **22**, 033101 (2010).
[5] E. Somfai *et al.*, Phys. Rev. E **75**, 020301(R) (2007); I. Agnolin and J-N. Roux, Phys. Rev. E **76**, 061303 (2007).
[6] L. Bocquet *et al.*, Nature (London) **396**, 735 (1998); G. Ovarlez and E. Clement, Phys. Rev. E **68**, 031302 (2003).
[7] K. Chen *et al.*, Nature (London) **442**, 257 (2006); T. Divoux, H. Gayvallet, and J.-Ch. Geminard, Phys. Rev. Lett. **101**, 148308 (2008).
[8] G. A. Caballero-Robledo and E. Clement, Eur. Phys. J. E **30**, 395 (2009).
[9] P. Sollich *et al.*, Phys. Rev. Lett. **78**, 2020 (1997); M. L. Falk and J. S. Langer, Phys. Rev. E **57**, 7192 (1998).
[10] G. Picard *et al.*, Eur. Phys. J. E **15**, 371 (2004); A. Tanguy *et al.*, Eur. Phys. J. E **20**, 355 (2006); C. Maloney and A. Lemaitre, Phys. Rev. E **74**, 016118 (2006).
[11] A. Lemaitre and C. Caroli, Phys. Rev. Lett. **103**, 065501 (2009); S. Karmakar, E. Lerner, and I. Procaccia, Phys. Rev. E **82**, 055103(R) (2010).
[12] C. Derec, A. Adjari, and F. Lequeux, Eur. Phys. J. E **4**, 355 (2001); L. Bocquet, A. Colin, and A. Ajdari, Phys. Rev. Lett. **103**, 036001 (2009).

Hot spots in an athermal system

Axelle Amon[1], Van Bau Nguyen[2,3], Ary Bruand[3], Jérôme Crassous[1], and Eric Clément[2]

[1] *Université de Rennes 1, Institut de Physique de Rennes (UMR UR1-CNRS 6251), Bât. 11A,Campus de Beaulieu, F-35042 Rennes, France*

[2] *PMMH, ESPCI, UMR CNRS 7636 and Université Paris 6 & Paris 7, 75005 Paris, France and*

[3] *Universit d'Orlans, CNRS/INSU, ISTO UMR 6113, F-45071 Orlans cedex 2, France*

(Dated: September 5, 2011)

Clarification of the mechanisms of plasticity and rupture in amorphous materials is a timely challenge. The state of the art postulates the existence of localized plastic events interacting through long range elastic coupling and triggering irreversible macroscopic deformations [1]. Models assuming such local features at the mesoscopic level are able to reproduce the generic rheology of a large class of materials [2–8]. The activation, dynamics and coupling of such zones have been intensively studied numerically and theoretically [8–14]. However, their concrete existence and their exact role in the various phases of the yield process remain elusive experimentally. Here we visualize directly localized deformation events ('hot spots') in a sheared granular packing using Diffusive Wave Spectroscopy. Their spatial clustering is shown to be linked to the emergence of shear bands. In creep experiments, we relate their rate of apparition to the global plastic deformation rate. We establish a bridge between our observations and the concept of 'fluidity', recently used to describe nonlocal rheology of several soft materials [15–18].

Our model of amorphous material is an assembly of glass spheres (diameter $200 \pm 30 \mu m$, packing fraction 0.60 ± 0.01) placed into an axisymmetric cylindrical shear cell (fig 1.a). Shear is obtained by rotation of a four blades vane. The applied stresses and deformations are controlled by a step motor fixed to a torsional spring. Constant motor rotation rate or constant shear stress can be imposed. Two surface loading conditions have been investigated: free and loaded. In addition to the mechanical measurements, we obtain spatially resolved map of the surface deformations using a Diffusive Wave Spectroscopy (DWS) technique [19]. A laser illuminates the top of the shear cell. A camera imaging that surface at a frame rate of 1 Hz, collects backscattered light. The correlation of scattered intensities between two successive images, g_I, are computed by zone, composing correlation maps of 370 μm resolution (fig 1.c). Maximal correlation (light yellow) corresponds to a deformation $\epsilon \lesssim 10^{-7}$ and vanishing correlation (black) corresponds to $\epsilon \gtrsim 10^{-5}$ (see Methods).

We first monitor the mechanical behavior of the system when submitted to an increasing shear stress. Fig 1.b shows the stress as a function of time at a constant motor rotation velocity. The stress increases linearly with the rotation as expected for an elastic material connected to a torsion spring. As the rotation is increased, small stress drops are first observed (precursor events) up to the maximal yield stress value σ_Y. Then, the system

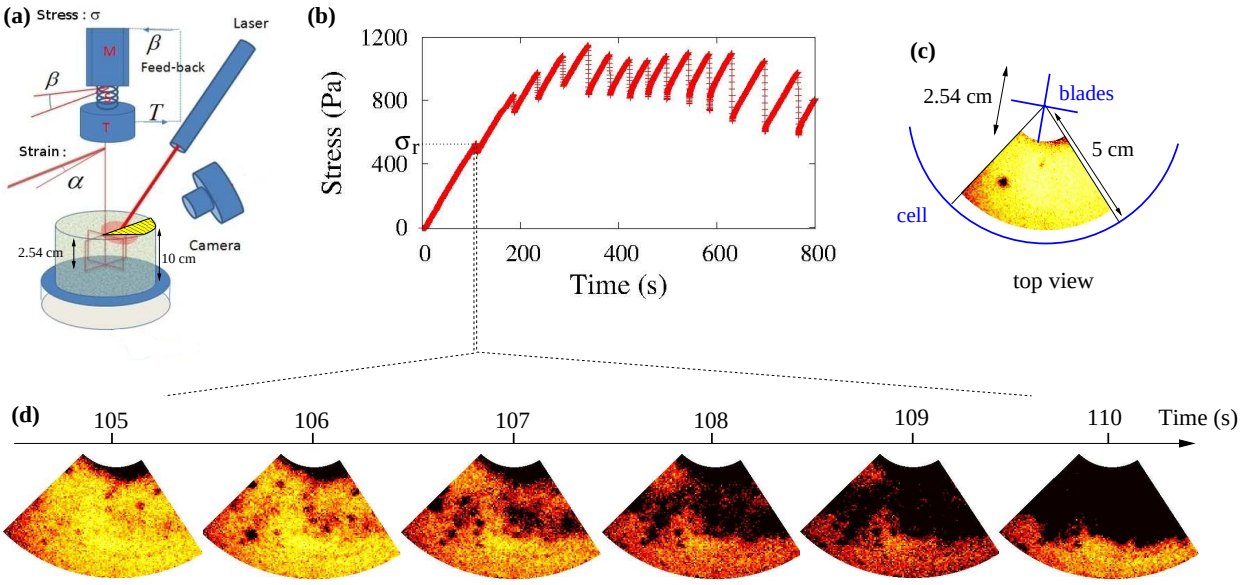

FIG. 1. (a) Schematic of the experimental set-up. (M): motor, (S): Torsion spring, (T): Torque probe. The feed-back loop allows to impose applied torque in creep experiments. A 633 nm HeNe Laser beam is expanded and illuminates about a quarter of the top surface. That surface is imaged with a lens on the camera. An iris diaphragm controls the size of the coherence areas on the camera. A polarizer is introduced in the light path to enhance contrast of the speckle pattern. (b) Stress response for an imposed deformation experiment in free surface boundary condition. (c) Part of the surface of the cell that is used for the analysis ($S = 13$ cm^2) showing a typical hot spot: in average $g_I \simeq 0.99$ (yellow) and $g_I \lesssim 0.95$ for the black spot. (d) Correlation maps between consecutive speckle images corresponding to the first stress drop at σ_r. The position of the first failure zone varies from experiments to experiments, and is not systematically situated at the outer edge of the blades as would be observed in Couette cell geometry.

reaches after few rupture events a regular stick-slip motion. This is to be expected for a soft torsion spring, driven at constant rotation rate and coupled with a material displaying both static and dynamic friction thresholds. Here we are only interested in the first part of the dynamics, up to σ_Y. The onset of precursor events was described by Nguyen *et al.* [20] and a similar phenomenology was also reported in many other amorphous glassy materials [10]. The DWS imaging of the top surface is shown on fig. 1.c. In the quasi-elastic part of the loading curves, the intensity correlation stays at $g_I \simeq 0.99$ except over small areas, the hot spots, where a significant localized correlation drop down to $g_I \lesssim 0.95$ is observed (see fig 1.c

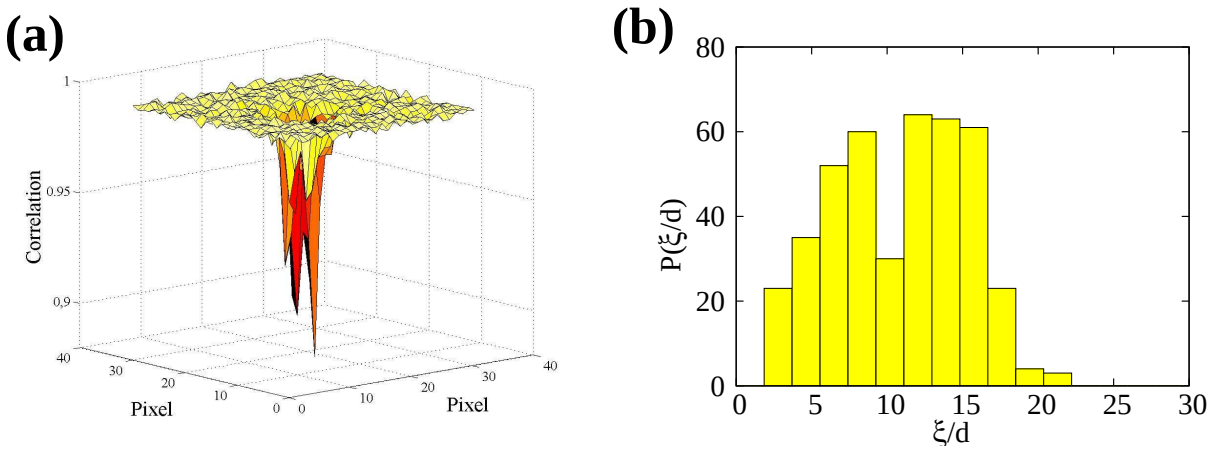

FIG. 2. Characterization of hot spots (a) 3D representation of a typical spot. (b) Distribution of hot spots sizes ξ in units of beads diameter d during a creep experiment.

and fig 2.a). The extent of these spots is typically $\xi \approx 3$ mm with a duration $\tau \sim 1$ s. The corresponding local deformation amplitude may be estimated from the decorrelation of the backscattered light [21, 22]: $\epsilon \simeq 5 \times 10^{-6}$ (see Methods). Figure 1.d shows successive maps corresponding to the first stress drop (see also the Supplementary Film). As the deformation is increased, more and more hot spots appear ($t = 105$ to 107 s). These events aggregate in clusters ($t = 107$ to 109 s). Finally, a large and totally uncorrelated zone supersedes the clusters ($t = 110$ s). This large decorrelation zone is associated with the first macroscopic stress drop. Therefore, the process is two-scales: the localized events occur as precursors of the macroscopic failure inside the glassy material when such failure is itself a precursor event of the final yield.

To link those localized plastic events to the global plastic deformation of the material, we do now creep experiments fixing the applied shear stress and monitoring both the global plastic deformation and the spatially resolved deformation map. On fig. 3 (blue symbols), we display an example of a global plastic deformation $\Delta\gamma(t)$ obtained at low applied shear stress $\sigma = 1200$ Pa, *i.e.* at a value smaller than the first precursor event $\sigma_r = 1700$ Pa. During this slow plastic deformation, the DWS imaging shows that the hot spots are still present and appear to be quite isolated at this level of applied stress. To quantify the relation between their apparition and the creep motion, the cumulated number of their occurrence $N(t)$ is computed and displayed on the same graph as $\Delta\gamma(t)$ (fig. 3). The temporal evolution of the two quantities are very similar. Therefore, the plastic deformation rate and the rate of

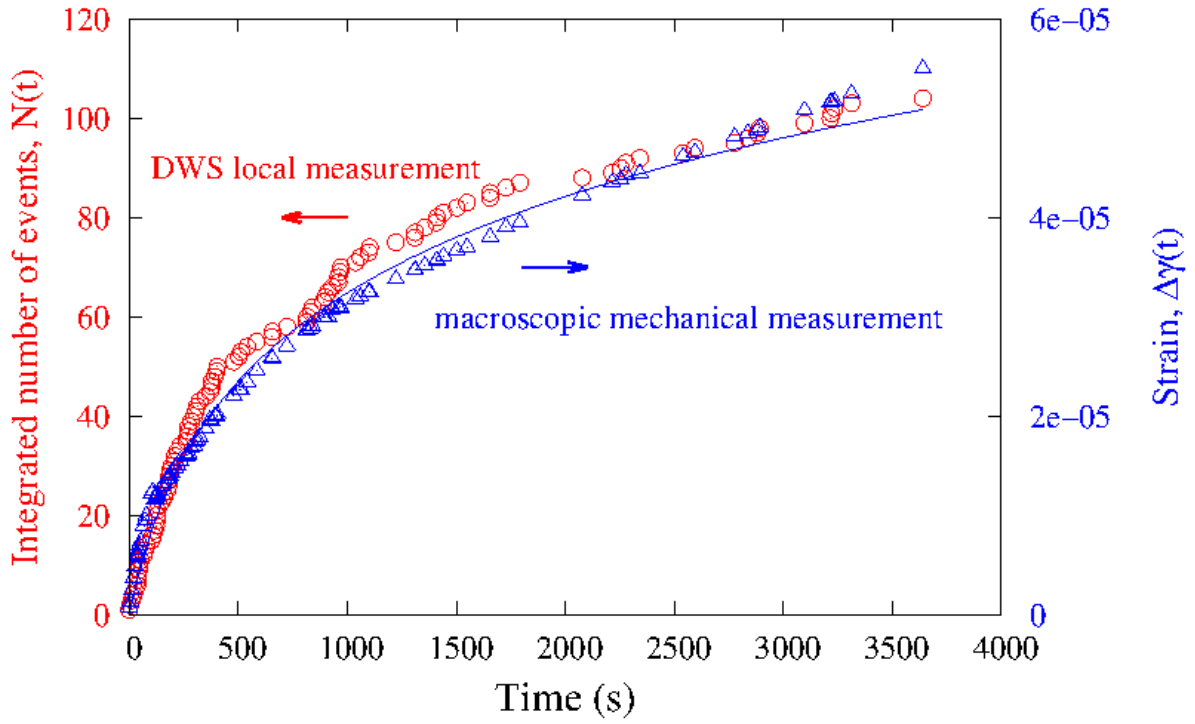

FIG. 3. Blue symbols (right axis): Strain as function of time in a creep experiment at applied shear $\sigma = 1200$ Pa for the loaded surface boundary condition. The origin of times is defined as the moment of application of the constant stress, after a linear stress ramp lasting about 100 s. Solid blue line: fit by a logarithmic creep law [20] $\Delta\gamma(t) = \dot{\gamma}_0 \ln(1 + Ct)/C$ with $C = 0.007$ s^{-1}. Red (left axis): integrated number of events.

apparition of localized event are proportional.

Such creep experiments can be interpreted using an age dependent relaxation rate [20] reminiscent of many models derived from the 'Soft Glassy Rheology'. In this context a simple visco-elastic scalar equation has been proposed [4] featuring an inverse characteristic relaxation time, the so-called 'fluidity' $f(t)$:

$$\dot{\sigma} = G\dot{\gamma} - f(t)\sigma \tag{1}$$

with σ the applied shear stress and G a shear elastic modulus. To close the model, a constitutive relation for $f(t)$ must be provided. Many forms were suggested [4] but for the present case, the observed creep dynamics is consistent with the relation: $\dot{f} \propto -f^2$, *i.e.* a relaxation time proportional to the actual age of the system (see fit of the strain on fig. 3). Building on the proportional relation between the rate of occurrence of hot spots and the

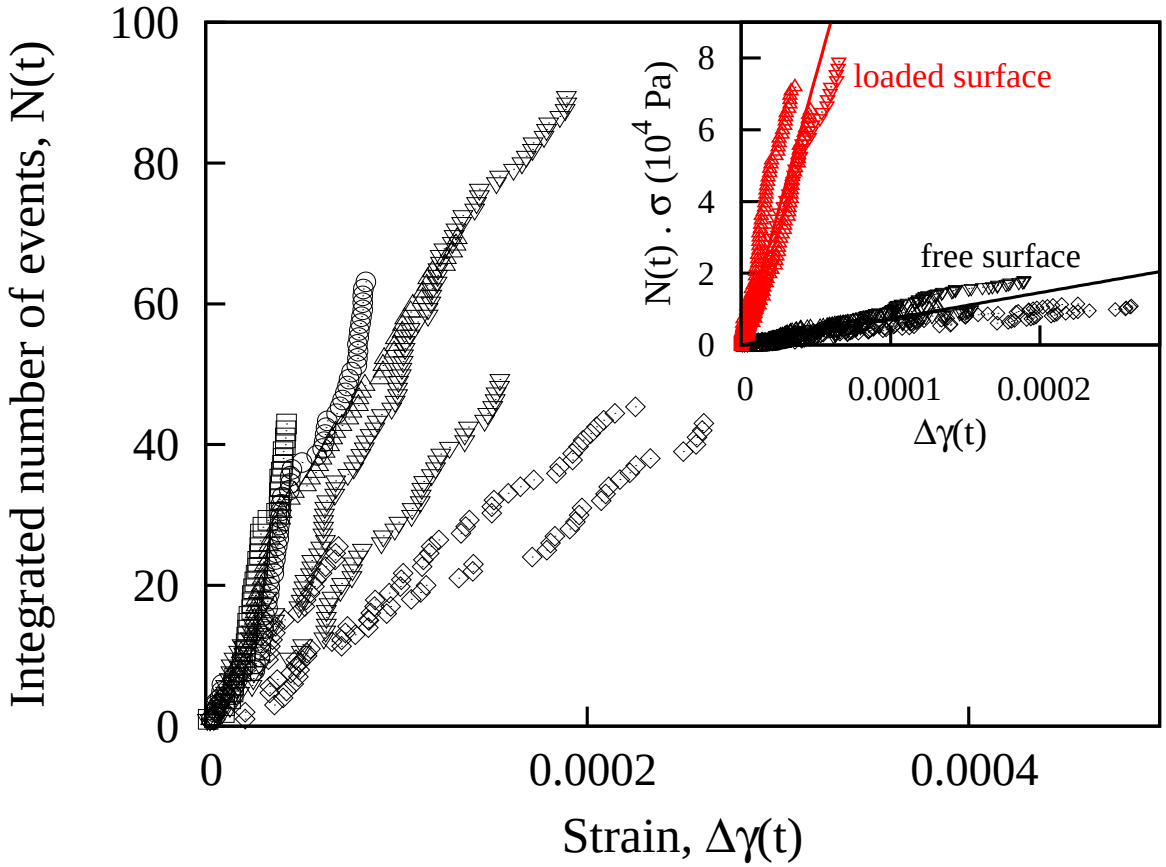

FIG. 4. Integrated number of events in a free surface experiment for different applied stress : 50 Pa (□), 100 Pa (○), 150 Pa (△), 200 Pa (▽) and 250 Pa (◊). Inset : integrated number of events multiply by the apply stress in two configurations. In black, free surface : data from the main graph. In red, loaded surface (top pressure equivalent to $P = 830$ Pa), applied stresses : 400, 800, 1200 and 1600 Pa.

shear rate, we propose now to go one step further and to identify $\dot{N}(t)$ with the fluidity parameter (within a proportionality constant). To test this proposition, we perform series of creep experiments at constant applied shear stresses σ for stress values below σ_r. Fig. 4 displays the relation between the cumulated number of events $N(t)$ and the total plastic strain $\Delta\gamma(t)$, for free surface loading condition. The relation is roughly linear, with slopes decreasing with the amplitude of the applied stress. Using our hypothesis of proportionality between the fluidity parameter and the hot spots rate of occurrence, integration of eq.(1) at

constant stress gives:

$$G\Delta\gamma(t) = \sigma \int_0^t f(t')dt' \propto \sigma N(t) \tag{2}$$

Following this relation it is then possible to collapse all the curves on a master straight line when multiplying $N(t)$ by the applied stress σ (inset of fig.4). To evaluate the robustness of this relation, we varied the top surface boundary condition: due to Hertz elasticity, the effective shear modulus G should increase with the confining pressure. Indeed, when the surface is loaded, the linear relation between $N(t)\sigma$ and $\Delta\gamma(t)$ hold (see inset of fig.4) showing the expected qualitative stiffening (a factor 20 approximatively). However from a simple account of the Hertz law, we should only expect here a factor 2. This significant difference is possibly due to the presence near the free surface of a strong stiffness gradient and a diverging elastic susceptibility.

So far, we have established a direct relation between the rate of plastic deformation and the apparition of the hot spots. Their clustering in the vicinity of major yield events *prior* to their macroscopic apparition, reinforces the idea that they play a leading role in the plasticity process. However, it is not *a priori* obvious that these are the only and sufficient modes of rupture which account for the full plastic flow dynamics. Therefore, we compare an estimation of the energy released by the hot spots to the total elastic energy dissipated in the bulk. The energy dissipation of one plastic event per unit of depth is $\sigma\epsilon\xi^2$, where σ is the local stress and $\epsilon \approx \sigma/G$ the typical plastic deformation during one event. We suppose that the 'hot spots' density is uniform in the bulk. During a creep experiment, the density of energy release through the elastic bulk relaxation processes is $\sigma\Delta\gamma(t)$. Then, the energy balance per unit depth, between the sum of the localized plastic dissipation $\sigma\epsilon\xi^2 N(t)$ and the bulk elastic relaxation $S\sigma\Delta\gamma(t)$ leads to the linear relation: $\sigma N(t) = K\Delta\gamma(t)$ with $K = GS/\xi^2$. Quantitatively, the relation can be tested on the surface loaded experiment for which the elastic response $G = 1.6 \times 10^6$ Pa has been measured (our torque probe was not sensitive enough to access to the elastic regime of the free surface packing). We obtain : $K \approx 10^9$ Pa close to the value obtain on the inset of fig.4. Therefore, within the consistency of the model, it seems that the energy released by the hot spots comes to the right magnitude to account for the macroscopic plasticity.

In this letter, we provide a direct visualization of localized deformation events associated with the mechanical response of a granular packing under shear. The optical DWS technique

captures the emergence of the so-called 'hot-spots', characterized by a spatial extension of about ten grains. Under a stress ramp, we show that these events increase in density with the stress amplitude and cluster spatially as precursors of the shear banding macroscopic yield events. Under constant applied shear stress, the rate of apparition of these hot spots at the top surface is proportional to the rate of plastic deformation. Varying the applied shear and the loading boundary conditions, we point that at first approximation - possibly corresponding to a mean-field approximate of the problem - the 'hot spot' dynamics is in direct relation with a parameter called fluidity defined in the context of 'Soft Glassy Rheology', and representing the mean rate of stress relaxation. Our study points out the interest of clarifying this relation, by characterizing the spatio-temporal coupling of the hot spot dynamics, in particular in the vicinity of the material yield or under sustained mechanical noise. These results provide some substantial experimental evidences backing many theoretical propositions made recently about zero temperature plasticity of amorphous solids. It focuses the debate on the importance of localized precursor events participating in the yield dynamics, a concept which can be crucial in a wide context encompassing solid disordered system, complex fluids or even earth-quake dynamics.

[1] Argon, A.S. Plastic deformation in metallic glasses. *Acta Metallurgica* **27,** 47-58 (1979).

[2] Sollich, P., Lequeux, F., Hébraud, P. & Cates M.E. Rheology of soft glassy materials. *Phys. Rev. Lett.* **78,** 2020–2023 (1997).

[3] Sollich, P. Rheological constitutive equation for a model of soft glassy materials. *Phys. Rev. E* **58,** 738–759 (1998).

[4] Derec, C., Ajdari, A. & Lequeux, F. Rheology and aging: A simple approach. *Eur. Phys. J. E* **4,** 355-361 (2001).

[5] Kabla, A. & Debrégeas, G. Local stress relaxation and shear banding in a dry foam under shear. *Phys. Rev. Lett.* **90,** 258303 (2003).

[6] Goyon, J., Colin, A., & Bocquet, L. How does a soft glassy material flow: finite size effects, non local rheology, and flow cooperativity. *Soft Matter* **6,** 2668-2678 (2010).

[7] Dahmen, K.A., Ben-Zion, Y. & Uhl, J.T. A simple analytic theory for the statistics of avalanches in sheared granular materials. *Nature Physics* **7,** 554–557 (2011).

[8] Lemaître, A. & Caroli, C. Rate-Dependent Avalanche Size in Athermally Sheared Amorphous Solids. *Phys. Rev. Lett.* **103,** 065501 (2009).

[9] Falk, M.L. & Langer, J.S Dynamics of viscoplastic deformation in amorphous solids *Phys. Rev. E* **57,** 7192–7205 (1998).

[10] Tanguy, A., Leonforte, F. & Barrat, J.-L. Plastic response of a 2d Lennard-Jones amorphous solid: Detailed analysis of the local rearrangements at very slow strain rate. *Eur. Phys. J. E* **20,** 355-364 (2006).

[11] Maloney, C.E. & Lemaître, A. Amorphous systems in athermal, quasistatic shear. *Phys. Rev. E* **74,** 016118 (2006).

[12] Lerner, E. & Procaccia, I. Scaling theory for steady-state plastic flows in amorphous solids. *Phys. Rev. E* **80,** 026128 (2009).

[13] Karmakar, S., Lerner, E. & Procaccia, I. Predicting plastic flow events in athermal shear-strained amorphous solids. *Phys. Rev. E* **82,** 055103(R) (2010).

[14] Talamali, S.M., Petäjä, V., Vandembroucq D., & Roux, S. Strain localization and anisotropic correlations in a mesoscopic model of amorphous plasticity. *Preprint: arXiv:1005.2463* (2011).

[15] Picard, G., Ajdari, A., Bocquet, L. & Lequeux, F. Simple model for heterogeneous flows of yield stress fluids. *Phys. Rev. E* **66,** 051501 (2002).

[16] Bocquet, L., Colin, A. & Ajdari, A. Kinetic theory of plastic flow in soft glassy materials. *Phys. Rev. Lett.* **103,** 036001 (2009).

[17] Goyon, J., Colin, A., Ovarlez, G., Ajdari, A. & Bocquet, L. Spatial cooperativity in soft glassy flows. *Nature* **454,** 84–87 (2008).

[18] Katgert, G., Tighe, B.P., Mobius, M.E. & van Hecke, M. Couette Flow of Two-Dimensional Foams. *Europhys. Lett.* **90,** 54002 (2010).

[19] Erpelding, M., Amon, A. & Crassous, J. Diffusive wave spectroscopy applied to the spatially resolved deformation of a solid. *Phys. Rev. E* **78,** 046104 (2008).

[20] Nguyen, V.B., Darnige, T., Bruand, A. & Clément, E. Creep and fluidity of a real granular packing near jamming. *Phys. Rev. Lett.* in Press (2011).

[21] Crassous, J. Diffusive wave spectroscopy of a random close packing of spheres. *Eur. Phys. J. E* **23,** 145-152 (2007).

[22] Erpelding, M., Amon, A. & Crassous, J. Mechanical response of granular media: New insights from diffusing-wave spectroscopy. *Europhys. Lett.* **91,** 18002 (2010).

Acknowledgements

We acknowledge the financial supports CNRS-PEPS program, the ANR projects "Jamvibe-2010" and "STABINGRAM" No. 2010-BLAN-0927-01. E.C. thanks Bruno Andreotti for many scientific discussions; A.A. and J.C. thank Patrick Chasles for help with the image acquisition.

Author Contributions

V.B.N., A.B. and E.C. designed the creep experiment, V.B.N. made creep experiment, A.A. and J.C. designed and made DWS experiments, A.A. did the data analysis and E.C., A.A. and J.C. wrote the paper.

Author Information

Correspondence and requests for materials should be addressed to E.C. (eric.clement@upmc.fr) or J.C. (jerome.crassous@univ-rennes1.fr)

Methods

The filling height of the shear cell is $\simeq 10\ cm$. The penetration depth of the vane is fixed so that the upper edge reaches the surface from below within a few grain sizes. During the insertion procedure the material is gently fluidized by an air flux in order to obtain a controlled uniform compacity, deduced from in-situ permeability measurement (see [20] for details). The fluidization process is stopped during each mechanical measurements. The spring deformation and the rotation of the vane are measured, giving access to the applied stresses and strains. The device is suited to work at an imposed motor rotation rate or at an imposed shear stress due to a feed back loop between the torque probe and the motor. For the loaded surface condition a circular glass lid with a hole for the axis is placed on the glassy material and supplementary loads are added, producing a top pressure equivalent to $P = 830$ Pa. The backscattering DWS technique probes the deformation field in a plane perpendicular to the shear vorticity axis in a depth corresponding to the light transport mean free path l^*. The correlation between the successive speckle patterns are computed and averaged over zones of 16×16 pixels, corresponding to $370\ \mu m \times 370\ \mu m$ areas. Previous work on backscattering DWS technique in granular packing [21, 22] have

established a relation $\epsilon \approx -\ln(g_I)/c$ were $c \simeq 15000$ is a numerical constant related to the ratio between $l^* \approx 3.3d$ and the optical wavelength. With $g_I \approx 0.95$, we obtain here approximatively $\epsilon \simeq 5 \times 10^{-6}$.

BIBLIOGRAPHIE

[1] A. Garcimartin E. Kolb J. Lanuza A. Janda, D. Maza and E. Clément. Unjamming a granular hopper by vibration. *A letters journal exploring the frontiers of physics*, 87 :24002, 2009.

[2] Ivana Agnolin and Jean-Noël Roux. Internal states of model isotropic granular packings. iii. elastic properties. *Physical Review E*, 2007.

[3] Douglas A.G. Andersland, O.B. Interesting case studies from the practice of engineering geology. *Nedra, Moskow*, page 224, 1981.

[4] H.A. Barnes. Introduction to rheology. *Elsevier*, 1989.

[5] J. Bear. Dynamics of fluids in porous media. *Dover*, 1989.

[6] L. Berthier and G. Biroli. A statistical mechanics perspective on glasses and aging *Encyclopedia of Complexity and Systems Science. Springer, New York*, 2008.

[7] W. Haegeman C. Karg. Elasto-plastic long-term behavior of granular soils : Experimental investigation. *Soil dynamics and earthquake engineering*, 29 :155–172, 2009.

[8] G.A. Caballero and E. Clément. Soil behaviour and critical state soil mechanics. *Cambridge University Press*, 1990.

[9] G.A. Caballero and E. Clément. Rheology of a sonofluidized granular packing. *Eur.Phys. J*, E30 :395–401, 2009.

[10] R. Candelier and O. Dauchot. Simple model for heterogeneous flows of yield stress fluids. *Phys. Rev. Lett*, 103 :128001, 2009.

[11] Kérisel J. Caquot A. Traité de mécanique des sols. *Editions Gauthier-Villars*, 1966.

[12] F. Caton and C. Baravian. Plastic behavior of some yield stress fluids : from creep to long time yield. *Rheologica Acta.*, 601 :47, 2008.

[13] A.Adjari C.Derec and F.lequeux. Rheology and aging : A simple approach. *Eur.Phys.J.*, E4 :395, 2001.

[14] Simon A. Johnson Christopher D. Willett, Michael J. Adams and Jonathan P. K. Seville. Capillary bridges between two spherical bodies. *Langmuir*, 16 :9396–9405, 2010.

[15] A.D. Yu C.L. Feng. Effect of liquid addition on the packing of mono-sized coarse spheres. *Powder Technology*, 99 :22–28, 1998.

[16] C. A. Coulomb. Essai sur un application de règles de maximis et minimis à quelques problèmes de statique, relatifs à l'architecture. *Mem. de Math. et de Phys. Acd. Roy. des Sci. Paris*, 7 :343, 1773.

[17] J. Crassous. Diffusive wave spectroscopy of a random close packing of spheres. *Eur. Phys. J. E*, 23 :145–152, 2007.

[18] I. Albert A.-L. Barabasi D. J. Hornbaker, R. Albert and P. Schiffer. What keeps sandcastles standing ? *Nature*, 387 :765, 1997.

[19] Ben-Zion Y. Uhl J.T Dahmen, K.A. A simple analytic theory for the statistics of avalanches in sheared granular materials. *Nature Physics*, 7 :554557, 2011.

[20] Nicolas Gland David L. Johnson Hernan A. Makse and Lawrence Schwartz. Why effective medium theory fails in granular materials. *Phys. Rev. Lett*, 83(24) :5070 :5073, 1999.

[21] S. N. Domenico. Elastic properties of unconsolidated porous sand reservoirs. *Geophysics*, 42(7) :1339–1368, 1977.

[22] J. Duffy and R.D.Mindlin. Stress-strain relations and vibrations of a granular medium. *Journal of applied mechanics*, 24(4) :585–593, 1957.

[23] Di Benedetto H. Van Bang D. Pham Ezaoui A. Duttine, A. Anisotropic small strain elastic properties of sands and mixture of sand-clay measured by dynamic and static methods. *Soils and foundation*, 47 :457–472, 2007.

[24] E. Ben Naim H. M. Jaeger E.R. Nowak, J.B. Knight and S. Nagel. Density fluctuations in vibrated granular materials. *Phys. Rev. E*, 57 :1971, 1998.

[25] C.O'Hern et al. Jamming at zero temperature and zero applied stress : The epitome of disorder. *Phys.Rev. E*, 011306 :68, 2003.

[26] E.Somfai et al. Critical and noncritical jamming of frictional grains. *Phys. Rev. E*, 020301 :75, 2007.

[27] J.Geng et al. GreenŠs function measurements of force transmission in 2d granular materials. *Physica D*, 274 :182, 2003.

[28] K. Chen et al. Granular materials : Packing grains by thermal cycling. *Nature*, 257 :442, 2006.

[29] L.Bocquet et al. Moisture-induced ageing in granular media and the kinetics of capillary condensation. *Nature*, 735 :396, 1998.

[30] A. Lemaitre et C. Caroli. Rate-dependent avalanche size in athermally sheared amorphous solids. *Phys. Rev. Lett.*, 065501 :103, 2009.

[31] Alain Ezaoui. Comportement expérimental statique et dynamique des salbes et modélisation 'élasto-visco-plastique' anisotrope en petites et moyennes déformations. *ENTPE Lyon, Thèse de docteur*, 2008.

[32] Di Benedetto Ezaoui, A. Experimental measurements of the global anisotropic elastic behaviour of dry hostun sand during triaxial tests, and effect of sample preparation. *Geotechnique*, 59 :621–635, 2009.

[33] Tatsuoka. F and Shibuya. S. Deformation characteristics of soils and rocks from field and laboratory tests. *9th Asian Regional Conference*, II :101–170, 1991.

[34] J. Kurchan F. Sausset, G. Biroli. Do solids flow ? *J.Stat.Phys.*, 718 :140, 2010.

[35] M. L. Falk and J. S. Langer. Dynamics of viscoplastic deformation in amorphous solids. *Phys. Rev. E*, 57(6) :7192–7205, 1998.

[36] Hervé Gayvallet Frédéric Restagno, Cécile Ursini and Elisabeth Charlaix. Aging in humid granular media. *Physical review E*, 66 :021304, 2002.

[37] M. I. Khan G. I. Tardos and D. G. Schaeffer. Forces on a slowly rotating, rough cylinder in a couette device containing a dry, frictional powder. *Phys. of Fluids*, 10 :335–341, 1998.

[38] E.Clement G.Ovarlez. Slow dynamics and aging of a confined granular flow. *Pys.Rev. E*, 031302 :68, 2003.

[39] J.J. Khan G.R. McDowell. Creep of granular materials. *Granular Matter*, 5 :115–120, 2003.

[40] Chu-heng Liu H. M. Jaeger and Sidney R. Nagel. Relaxation at the angle of repose. *Physical Review Letters*, 62, 1, 1989.

[41] P. Hebraud and F. Lequeux. Mode coupling theory for the pasty rheology of soft glassy materials. *Phys. Rev. Lett*, 81 :2934–2937, 1998.

[42] S. Herminghaus. Dynamics of wet granular matter. *Advances in Physics*, 54 :221–261, 2005.

[43] David L. Johnson Hernan A. Makse and Lawrence M. Schwartz. Packing of compressible granular materials. *Physical review letters*, 84 :18, 2000.

[44] C. Radin H. L. Swinney J-F. Métayer, D. J. Suntrup III and M. Schröter. Shearing of frictional sphere packings. *A letters journal exploring the frontiers of physics*, 93 :64003, 2011.

[45] K. L Johnson. Contact mechanics. *Cambridge University Press*, 1985.

[46] Paul A. Johnson and Xiaoping Jia. Nonlinear dynamics, granular media and dynamic earthquake triggering. *Nature*, 437 :871–874, 2005.

[47] Y. Forterre K. A. Reddy and O. Pouliquen. Evidence of mechanically activated processes in slow granular flows. *Physical Review Letters*, 108301 :106, 2011.

[48] Y. Khidas and X. Jia. Anisotropic nonlinear elasticity in a spherical-bead pack : Influence of the fabric anisotropy. *Phys. Rev. E*, 021303 :81, 2010.

[49] Renaud Bastien Elie Wandersman Kiri Nichol, Alexey Zanin and Martin van Hecke. Flow-induced agitations create a granular fluid. *Physical Review Letters*, 078302 :104, 2010.

[50] D. Schalk T. C. Lubensky L. Bocquet, W. Losert and J. P. Gollub. Granular shear flow dynamics and forces : Experiment and continuous theory. *Phys. Rev. E*, 65 :011307, 2002.

[51] B. Andreotti L. Bonneau and E. Clément. Surface elastic waves in granular media under gravity and their relation to booming avalanches. *Physical Review E*, 2007.

[52] A.Ajdari L.Bocquet, A.Colin. Kinetic theory of plastic flow in soft glassy materials. *Phys. Rev. Lett.*, 036001 :103, 2009.

[53] Andrea J. Liu and Sidney R. Nagel. Jamming is not just cool any more. *Nature*, 396 :21–22, 1998.

[54] Christian D. Lorenz and Mark J. Stevens. Fracture behavior of lennard-jones glasses. *Phys. Rev. E*, 68 :021802, 2003.

[55] Frédéric Restango Lydéric Bocquet, Elisabeth Charlaix. Physics of humid granular media. *C. R. Physique*, 3 :207–215, 2002.

[56] S. H. Yu M. J. Jiang and D. Harris. Bond rolling resistance and its effect on yielding of bonded granulates by dem analyses. *Int. J. Numer. Anal. Meth. Geomech*, 30(8) :723–761, 2006.

[57] M. ASCE M. Jiang, S. Leroueil and J-M. Konard. Yield of micro structured geomaterial by distinct element method analysis. *Journal of engineering mechanics, ASCE*, 131(11) :1209–1213, 2005.

[58] N. H. Loh M. L. Foong, K. C. Tam. Yield stress behaviour of metal injection moulding suspensions at elevated temperatures. *Journal of materials science*, 30 :3625–3632, 1995.

[59] H. J. Herrmann D. W. Howell M. Lätzel, S. Luding and R. P. Behringer. Comparing simulation and experiment of a 2d granular couette shear device. *Eur. Phys. J. E*, 11(4) :325333,, 2003.

[60] S. Luding M. Lätzel and H. J. Hermann. Macroscopic material properties from quasi-static, microscopic simulations of a two-dimensional shear-cell. *Granular Matter*, 2 :123–135, 2000.

[61] M. Bringkmann M. Di Michiel A. Sheppard B. Breidenbach M. Scheel, R. Seemann and S. Herminghaus. Morphological clues to wet granular pile stability. *Nature materials*, 10.1038 :2117, 2008.

[62] A. Maloney, C.E. Lemaître. Amorphous systems in athermal, quasistatic shear. *Phys. Rev. E*, 74 :016118, 2006.

[63] Axelle Amon Marion Erpelding and Jérôme Crassous. Diffusive wave spectroscopy applied to the spatially resolved deformation of a solid. *Physical review E*, 78 :046104, 2008.

[64] Axelle Amon Marion Erpelding and Jérôme Crassous. Mechanical response of granular media : New insights from diffusing-wave spectroscopy. *EPL*, 91 :18002, 2010.

[65] D. Muir-Wood. Soil behaviour and critical state soil mechanics. *Cambridge University Press*, 1991.

[66] D.M. Newitt and J.M. Conway-Jones. A contribution to the theory and practice of granulation. *Trans. I. Chem. Eng.*, 422 :36, 1958.

[67] Proc. R. Soc. London Ser. A P. W. Rowe. 269 :500, 1962.

[68] Matt Knuth Joan Gomberg Paul A. Johnson, Heather Savage and Chris Marone. Effects of acoustic waves on stick-slip in granular media and implications for earthquakes. *Nature*, 451 : 57–61, 3 January 2008.

[69] Ajdari A. Bocquet L. Lequeux F Picard, G. Simple model for heterogeneous flows of yield stress fluids. *Phys. Rev. E*, 66 :051501, 2002.

[70] Y. Pomeau. Fundamental problems in brittle fracture : unstable cracks and delayed breaking. *C.R.A.S. Mec.*, 249 :330, 2002.

[71] A.-L. Barabasi R. Albert, M. A. Pfeifer and P. Schiffer. Slow drag in a granular medium. *Phys. Rev. Lett.*, 84(1) :205–208, 1999.

[72] Gabriel Arturo Caballero Robledo. Slow relaxation and jamming transition in non-brownian systems. *Thesis of Universidad Nacional Autonoma de México*, pages 29–36, 2006.

[73] W. Volk-S. Diebels H.J. Herrmann S. Luding, M. Lätzel. From discrete element simulations to a continuum model. *Comput. Methods Appl. Mech. Engrg*, 191 :21–28, 2001.

[74] Kazutoshi Michihiro Sakuro Murayama and Toshihiko Sakagami. Creep characteristics of sands. *Soils and foundations*, 24 :1–15, 1984.

[75] P. A Schiffer. Bridge to sandpile stability. *Nature Phys*, 1 :21–22, 2005.

[76] S. Schöllmann. Simulation of a two-dimensional shear cell. *Phys. Rev. E*, 59 :889–899, 1999.

[77] J.H. Schmertmann. *J.Geotech.Eng*, 288 :117, 1991.

[78] K. Hapgood S.M. Iveon, J.D Litster and B.J. Ennis. Nucleation, growth and break phenomena in agitated wet granulation processes : a review. *Powder Technol.*, 117 :3, 2001.

[79] Lequeux F. Hebraud P. Sollich, P. and M. E. Cates. Rheology of soft glassy materials. *Phys. Rev. Lett.*, 2020 :78, 1997.

[80] Peter Sollich. Rheological constitutive equation for a model of soft glassy materials. *Phys. Rev. E*, 58 :738–759, 1998.

[81] El Youssoufi M. S. Cherblanc F. Saix C. . Soulie, F. Capillary cohesion and mechanical strength of poly-disperse granular materials. *European Physical Journal E*, 21 :349–357, 2006.

[82] S.Torquato and F.H.Stillinger. Jammed hard-particle packings : From kepler to bernal and beyond. *Rev.Mod.Phys.*, 2633 :82, 2010.

[83] Petſajſa V. Vandembroucq D. Roux S Talamali, S.M. Strain localization and anisotropic correlations in a mesoscopic model of amorphous plasticity. *Preprint : arXiv :*, page 1005.2463, 2011.

[84] Leonforte F. Barrat J.-L Tanguy, A. Plastic response of a 2d lennard-jones amorphous solid : Detailed analysis of the local rearrangements at very slow strain rate. *Eur. Phys. J. E*, 20 :355–364, 2006.

[85] H. Gayvallet T.Divoux and J.-Ch. Geminard. Creep motion of a granular pile induced by thermal cycling. *Phys. Rev. Lett.*, 148308 :101, 2008.

[86] C. Thorton and C. W. Randanll. Applications of theoretical contact mechanics to solid particle system simulation. *Micromechanics of Granular Materials, M. Satake and J. T. Jenkins, eds., Elsevier Sci. Pub*, 1988.

[87] M. Tsamados. Plasticity and dynamical heterogeneity in driven glassy materials. *Eur.Phys.J.E*, 165 :32, 2010.

[88] M van Hecke J.Phys. Jamming of soft particles : geometry, mechanics, scaling and isostaticity. *Cond.Matt.*, 033101 :22, 2010.

[89] L. Vanel and E. Clément. Pressure screening and fluctuations at the bottom of a granular column. *Eur. Phys. J*, 11 :525–533, 1999.

[90] Emilien Azéma Farhang Radjaï Vincent Richefeu, Moulay Saïd El Youssoufi. Force transmission in dry and wet granular media. *Powder Technology*, 190 :258Ű263, 2009.

[91] Moulay Saïd El Youssoufi Vincent Richefeu and Farhang Radjaï. Shear strength properties of wet granular materials. *Physical Review E*, 051304 :73, 2006.

[92] T.C. Lubensky W. Losert, L. Bocquet and J. P. Gollub. Particle dynamics in sheared granular matter. *Phys. Rev. Lett*, 85(7) :1428, 2000.

[93] K. Walton. The effective elastic moduli of a random packing of spheres. *Journal of the Mechanics and Physics of Solids*, 35(2) :213–226, 1987.

[94] C. Caroli X. Jia and B. Velicky. Ultrasound propagation in externally stressed granular media. *Phys. Rev. Lett.*, 82(9) :1863–1866, 1999.

[95] S Herminghaus M M Kohonen F Mugele M Scheel M Schulz B Schulz Ch Schier R Seemann Z fournier, D Geromichalos and A Skudelny. Mechanical properties of wet granular materials. *Journal of Physics Condensed Matter*, 17 :S477–S502, 2005.

Van Bau NGUYEN

Fluage et fluidité d'un empilement granulaire sous contrainte

Résumé :

L'objectif principal de la thèse a été d'identifié expérimentalement les comportements mécaniques et rhéologiques de milieux granulaires dans un environnement à complexité croissante. En particulier, je me suis intéressé aux phénomènes de fluage sous contrainte en essayant de mieux comprendre l'impact des vibrations et la présence d'une faible quantité d'eau piégée entre les pores.
J'ai monté un système cissométrique permettant de réaliser des tests mécaniques de fluage. Une originalité de mon montage a été de mettre au point un système de lit fluidisé qui, en alliant flux d'air et vibration, m'a permis de fabriquer des empilements à compacité initiale contrôlée. J'ai étudié les propriétés fondamentales de fluage sous contrainte d'un empilement granulaire de billes de verre de taille $d = 200\mu m$ sous le seuil de Coulomb. Cette étude a mis en évidence que les seuils de Coulomb varient fortement avec la compacité, mais en plus , on a mis en évidence une contrainte σ_r appelée " contrainte de première rupture " qui traduit des réorganisation internes dans l'empilements et qui est d'environ 1/3 de la contrainte seuil maximale. En outre, grâce à la précision de la mesure de déformation, on a obtenu les réponses élastiques à de petits cycles en contrainte et on a établi que le module cisaillement élastique G augmente linéairement en fonction de la compacité, en accord avec le modèle d'élasticité non-linéaire de Hertz (modèle de champ moyen). Nous avons réalisé aussi une étude paramétrique complète du fluage en variant systématiquement la compacité et la contrainte de cisaillement. Notre étude sur les seuils de contrainte, l'élasticité effective et la dynamique de fluage, a été prolongée pour des empilements sous vibration générés par des transducteurs piézo-électriques enfouis sous la surface. Ce montage permet en outre par injection dans le granulaire d'un gaz saturé en vapeur d'eau, d'imposer sous un faible gradient thermique une condensation et d'obtenir une quantité contrôlée d'eau piégée dans l'empilement. Cette méthode permettra par la suite d'aborder le cas de granulaires cohésifs.
Mots clés : milieux granulaire, fluage, vibration, pont capillaire ...

Creep and fluidity of a granular packing under shear stress.

Résumé :

The main objective of the thesis was to identify experimentally the mechanical and rheological behavior of granular media in an environment varying in complexity. In particular, I was interested to creep phenomenon under stress in trying to understand better the impact of vibration and the presence of a small amount of water trapped between the grains.
I set-up a system to perform mechanical creep tests. Originality of my setup was the fluidized bed which uses air flow and vibration, and thus allows the control of the initial packing fraction. I studied the basic properties of creep strain of a granular resulting from a packing of glass beads of size d = 200 μm under the Coulomb threshold. This study showed that the Coulomb thresholds vary strongly with the packing fraction. In addition, it showed a stress σ_r called "the first rupture", that results from internal reorganizations in the granular medium and which is approximately $1/3$ of the maximum stress threshold. Moreover, thanks to the precision of measuring deformation, we obtained the elastic response with small stress cycles, and we found that the shear elastic modulus G increases linearly with the packing fraction, in agreement with the model of nonlinear elasticity of Hertz (mean field). We performed a parametric study of creep in varying the packing fraction and shear stress. In all cases, we found the dynamics of logarithmic strain for long times. Our study on stress threshold, the elastic modulus and dynamics of creep, has been extended to granular medium under vibration generated by piezoelectric transducers buried under the surface. A small amount of water can be added and thus modifies the mechanical properties by the presence of capillary bridges. Preliminary experiments show the dependence of the Coulomb threshold of the elastic response and dynamic creep with an amount of water content.
Keywords : granular medium, creep, vibration, capillary bridge ...

Institut des Sciences de la Terre d'Orléans
Laboratoire Physique et Mécanique des Milieux Hétérogènes